amU
Aix Marseille Université

NNT : 2025AIXM0000

THÈSE DE DOCTORAT

Soutenue à Aix-Marseille Université
le 21 Janvier 2025 par

Simone Scollo

Mixing inside a tilted rotating cylindrical container

Discipline
Sciences pour l'Ingénieur

Spécialité
Mécanique et physique des fluides

École doctorale
ED 353: Sciences pour l'Ingénieur : Mécanique, Physique, Micro et Nanoélectronique

Laboratoire
Institut de Recherche sur les Phénomènes Hors Equilibre (IRPHE)

Composition du jury

Jörg SCHUMACHER Professeur, Technische Universitat, Imenau (Allemagne)	Rapporteur
Florence RAYNAL DR CNRS, Ecole Centrale Lyon	Rapporteur
Giorgio KRSTULOVIC CR CNRS, Laboratoire Lagrange, Nice	Examinateur
Jerome NOIR Professeur, ETH Zurich	Président du jury
Patrice Meunier DR CNRS, IRPHE	Directeur de thèse
Emmanuel VILLERMAUX Professeur, Aix Marseille Université	Codirecteur de thèse

CoPerMix
European ITN project

irphé
Institut de Recherche sur les Phénomènes Hors Equilibre

Affidavit

I, undersigned, Simone Scollo, hereby declare that the work presented in this manuscript is my own work, carried out under the scientific supervision of Patrice Meunier and Emmanuel Villermaux, in accordance with the principles of honesty, integrity and responsibility inherent to the research mission. The research work and the writing of this manuscript have been carried out in compliance with both the french national charter for Research Integrity and the Aix-Marseille University charter on the fight against plagiarism.

This work has not been submitted previously either in this country or in another country in the same or in a similar version to any other examination body.

Marseille 12 Novembre 2024,



This work is licensed under Creative Commons Attribution-NonCommercial-NoDerivatives 4.0 International Public License

Liste de publications et participation aux conférences

Liste des publications réalisées dans le cadre du projet de thèse

1. Scollo S., Nobili C., Villermaux E., Meunier P. 2023 Resonances and instabilities in a tilted rotating annulus, *J. Fluid Mech.* **973**, A34.

Participation aux conférences et écoles d'été au cours de la période de thèse

1. Solvay Conference Mixing: at the crossroads of foundations and practices (4-6 December 2024) International Solvay Institutes for Physics and Chemistry, Bruxelles
2. EFDC1 2024 (16-20 September 2024) Exploring Mixing with Diffuselet Method European Mechanics Society Aachen, Germany
3. Summer School Frontiers of Mixing (15-25 August 2023) Cargese, Corse
4. GreZuMar (4 May 2023) Precession-Like instability in a tilted rotating annulus Marseille.
5. APS DFD 2023 (19-21 November 2022) Diffuselet method in a rotating tilted cylinder American Physics Society Washington DC
6. Summer School Wave Turbulence and Beyond (18-21 July 2022) Turin, Italy
7. CoPerMix Mid-term meeting (16-17 June 2022) ULB, Bruxelles
8. APS DFD 2022 (20-22 November 2022) Annular Geoinspired Soft Mixer American Physics Society Indianapolis
9. Mixing in Action (17-21 of October 2022) ICTP Trieste, Italy
10. Fundamentals of mixing (04-8 April 2022) CoPerMix - Marseille

Abstract

This thesis explores the mixing properties of the "soft mixer", a specialized rotating bioreactor designed for low-shear fluid mixing, particularly suitable for cultivating fragile cells like dinoflagellates and stem cells. The device comprises a fluid-filled rotating cylinder, where the height of the fluid is critical for achieving resonant motion that enhances mixing without high shear. An observed challenge was suboptimal light exposure within the reactor, affecting dinoflagellate growth. To address this, the bioreactor's geometry was altered to an annular configuration, introducing the inner cylinder radius as a new variable. Experimental and theoretical studies, using Particle Image Velocimetry (PIV) for flow analysis, verified the impact of this modification on flow stability and mixing behavior. Further mixing studies employed Laser Induced Fluorescence (LIF) to trace dye dispersion and to measure the mixing efficiency as a function of the tilt angle and Ekman number.

In addition, a novel numerical method called the Diffuselet method (P. Meunier & E. Villermaux, J. Fluid Mech. 951, 2022) was used for calculating the evolution of a passive scalar field within a prescribed flow field. The advantage of this method is the possibility of doing it for parameters that are virtually inaccessible to the DNS. In fact, using the Ranz transformation (Ranz, AiChE J., 1979) to couple advection with molecular diffusion is possible to account explicitly (and nearly exactly) for the stretching history of each individual fluid element. The mixing characteristics (mixing time, concentration distribution and variance decay) are statistically captured with Lagrangian tracers to have statistic of the mixture in terms of the contributions of the different sub-regions of the flow. We have applied this method to the soft mixer, whose non-trivial flow field is nevertheless described analytically. The model is tested against experimental observations using LIF. This approach enables the acquisition of experimental statistics for comparison with the numerical results. The variance and the probability distribution functions (PDF) are correctly predicted by the Diffuselet method.

Finally, the case of a stratified fluid in a soft mixer has been studied experimentally. Several bands of instabilities have been observed at specific values of the Froude number, that can be predicted theoretically.

Keywords : Mixing, Rotating Flows, Parametric Instability.

Résumé

Cette thèse explore les propriétés de mélange du "soft mixer", un bioréacteur rotatif conçu pour le mélange de fluides à faible cisaillement, particulièrement adapté à la culture de cellules fragiles telles que les dinoflagellés et les cellules souches. L'appareil est constitué d'un cylindre rotatif rempli de fluide, où la hauteur du fluide est cruciale pour atteindre un mouvement résonnant qui améliore le mélange sans imposer un cisaillement élevé.

Un problème observé était l'exposition lumineuse sous-optimale à l'intérieur du réacteur, ce qui affectait la croissance des dinoflagellés. Pour remédier à cela, la géométrie du bioréacteur a été modifiée en une configuration annulaire, introduisant le rayon du cylindre intérieur comme nouveau paramètre. Des études expérimentales et théoriques, utilisant la vélocimétrie par imagerie de particules (PIV) pour l'analyse de l'écoulement, ont vérifié l'impact de cette modification sur la stabilité de l'écoulement et le comportement du mélange. La fluorescence induite par laser (LIF) a été utilisée pour suivre la dispersion du colorant et mesurer l'efficacité du mélange en fonction de l'angle d'inclinaison et du nombre d'Ekman.

De plus, une nouvelle méthode numérique, appelée méthode Diffuselet, a été utilisée pour calculer l'évolution d'un champ scalaire passif au sein d'un champ d'écoulement prescrit. L'avantage de cette méthode réside dans la possibilité de l'appliquer à des paramètres pratiquement inaccessibles aux simulations DNS. En effet, en utilisant la transformation de Ranz pour coupler l'advection avec la diffusion moléculaire, il est possible de rendre compte explicitement (et presque exactement) de l'historique d'étirement de chaque élément fluide individuel. Les caractéristiques de mélange (temps de mélange, distribution des concentrations et décroissance de la variance) sont capturées statistiquement avec des traceurs lagrangiens pour obtenir une statistique globale du mélange en fonction des contributions des différentes sous-régions du flux. Nous avons appliqué cette méthode au soft mixer, dont le champ d'écoulement non trivial est néanmoins décrit analytiquement. Le modèle est testé par rapport aux observations expérimentales à l'aide de la méthode LIF. Cette approche permet d'obtenir des statistiques expérimentales pour les comparer avec les résultats numériques. La méthode Diffuselet prédit correctement la variance et les fonctions de distribution de probabilité (PDF).

Enfin, le cas d'un fluide stratifié dans un soft mixer a été étudié expérimentalement. Plusieurs bandes d'instabilités ont été observées pour des valeurs spécifiques du nombre de Froude, qui peuvent être prédites théoriquement.

Mots clés : Mélange, Flux rotatifs, Instabilité paramétrique.

Acknowledgements

I want to thank my supervisors Patrice Meunier and Emmanuel Villermaux for the opportunity they gave me and for what I learnt. All the people from CoPerMix, our project, with whom I shared this journey. Special thanks to the people who hosted me at their universities Colm-Cille Patrick Caulfield and Jörg Schumacher. All the people working and studying in the IRPHE Laboratory who were able to understand a difficult person, and whom I will never regret enough for not sharing enough time together. Impossible not to thank my friend and colleague Lucas Rotily, there are no words to describe our sharing (il sait). Last but not least, I want to thank another friend Nicolaos Petropoulos an essential travelling companion.

This project has received funding from the European Union's Horizon 2020 research and innovation program under the Marie Skolodowska-Curie grant agreement N°956457.

Table of contents

Affidavit ii

Liste de publications et participation aux conférences iii

Abstract iv

Résumé v

1 Introduction 1
- 1.1 Motivation . . . 1
  - 1.1.1 Bioreactor . . . 1
  - 1.1.2 Geophysics . . . 3
- 1.2 Dynamics of rotating flows . . . 7
  - 1.2.1 Rotating flows: Navier-Stokes equation . . . 7
  - 1.2.2 Solid Body rotation . . . 11
  - 1.2.3 Geostrophic flow . . . 11
  - 1.2.4 Inertial waves . . . 13
  - 1.2.5 Global Inertial modes: Kelvin modes . . . 15
  - 1.2.6 Forcing by the free surface . . . 17
  - 1.2.7 Ekman layer . . . 18
  - 1.2.8 Application to a tilted rotating cylinder . . . 21
  - 1.2.9 Stability of the flow . . . 23
    - 1.2.9.1 Centrifugal Instability . . . 23
    - 1.2.9.2 Triadic Instability . . . 25
- 1.3 Mixing . . . 28
  - 1.3.1 General Introduction to Mixing . . . 28
  - 1.3.2 Diffuselet Method . . . 34
- 1.4 Content of the Manuscript . . . 37

2 Resonances and Instabilities in a tilted rotating Annulus 38
- 2.1 Introduction . . . 38
- 2.2 Materials and methods . . . 40
  - 2.2.1 Experimental set-up . . . 40
  - 2.2.2 Non-dimensional parameters . . . 40

2.2.3 Measurement techniques . . . 41
2.3 Forced mode . . . 42
2.4 Instabilities of the flow . . . 49
2.4.1 Onset time of the instability . . . 49
2.4.2 Triadic instability . . . 49
2.4.3 Centrifugal instability . . . 55
2.4.4 Turbulent flow regime . . . 56
2.5 Mixing . . . 58
2.5.1 Variance of concentration . . . 58
2.5.2 Decaying time as a function of h . . . 59
2.5.3 Decaying time as a function of E . . . 59
2.6 Conclusion . . . 60
2.7 Appendix . . . 62
2.7.1 Amplitude viscous correction . . . 62
2.7.2 Amplitude equations for triadic instability . . . 64
2.7.3 Small gap limit . . . 67

3 Diffuselet Method : Numerical Implementation 71
3.1 Numerical Cost . . . 71
3.2 From the theory to the algorithm . . . 72
3.3 Validation of the code . . . 75
3.4 Convergence Study of the code for the Soft Mixer . . . 79
3.5 Results in Turbulent DNS . . . 82

4 Diffuselet Method in the rotating tilted Cylinder 85
4.1 Description of the flow . . . 85
4.1.1 Non-dimensional parameters . . . 85
4.1.2 Fitting model . . . 86
4.1.3 Geostrophic flow . . . 87
4.1.4 PIV measurement of the amplitudes . . . 87
4.2 The Diffuselet method . . . 91
4.3 Comparison with experiment . . . 94

5 Stratified Fluid in Rotating Cylinder 99
5.1 Method and material . . . 99
5.1.1 Experimental set-up . . . 99
5.1.2 Procedure . . . 100
5.1.3 Measurement of the Stratification . . . 102
5.2 Experimental results . . . 102
5.3 Theoretical Background . . . 104

6 Conclusion 109
6.1 Summary . . . 109
6.2 Future work . . . 110

References **112**

Chapter 1

Introduction

This manuscript describes the mixing properties of a rotating and tilted cylinder. We first describe why such a set-up has been studied on a fundamental point of view and used in the industry. We then describe the mathematical background necessary for the description of the flow and the mixing.

1.1 Motivation

1.1.1 Bioreactor

A bioreactor is a device or system designed to support a biologically active environment, facilitating the growth and maintenance of various microorganisms, cells, or tissues. It plays a key role in biotechnology and bioengineering, as well as in the production of biological products such as pharmaceuticals, biofuels, and enzymes (Prokop 1981). By providing optimal conditions—such as temperature, pH, oxygen (O_2) and/or carbon dioxide (CO_2) levels, and nutrient supply—bioreactors allow for the controlled growth of these biological entities.

For cell-based therapies and drug production/testing, the goal is to maximize biomass production, which is done by achieving a high concentration of cells while maintaining a rapid duplication. However, when the number of cells increases, the large bioreactors require a high-oxygen (O_2) flux. To meet this need, the bioreactors commonly used in industry employ stirring mechanisms that induce mixing via propellers or blades (Doran 1999, Stephenson & Grayson 2018) (see Figure 1.1). Another popular bioreactor type uses bubble column injection to enhance mixing (Kantarci *et al.* 2005). These methods homogenize the fluid within the bioreactor, ensuring a high O_2 flux and rapid CO_2 expulsion. However, this efficiency comes at the cost of creating high-shear regions with an average shear rate of approximately

$$\gamma \sim 10^3 \text{ s}^{-1}, \tag{1.1}$$

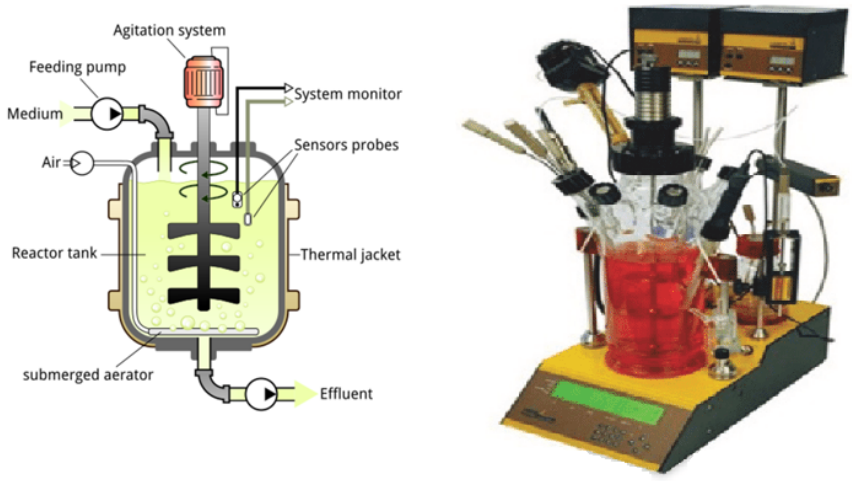


Fig. 1.1 Schematics of bioreactors commonly used in industry on the left (taken from https://bioprocessing.weebly.com/types-of-fermenters.html) and an actual device on the right (Valdés *et al.* 2017).

for the classical Rushton turbine setup (Bustamante *et al.* 2013), and

$$\gamma \sim 10 \text{ s}^{-1}, \tag{1.2}$$

for a bubble column configuration (De Jesus *et al.* 2017).

A special category of cell cultures includes fragile cells, such as stem cells, for which the maximum shear rate is typically limited to around $\gamma_{\max}^{SC} \sim 1$ to $10\,\text{s}^{-1}$ (Halim *et al.* 2020). Above this value, the duplication rate drops and the cells may even differentiate or lose their biological functions. Such cultures require continuous mixing and efficient mass transfer to ensure that metabolic requirements are homogeneously maintained throughout the volume, all while keeping shear forces low to protect these sensitive cells. Finally, to support stem cell growth, the culture environment must remain sterile, with temperature carefully regulated by an incubator (see Figure 1.2). To address this need, a new device was developed (Meunier 2020, Meunier 2020b).

This device, known as a "soft mixer" (see Figure 1.2), consists of a rotating cylinder tilted relative to gravity, allowing a harmonic forcing from the free surface to create mixing. This setup is scalable, providing uniform local shear by using a bladeless mixing mechanism, where the forcing scales with the volume, and the shear rate depends solely on the rotation speed. Additionally, the device ensures efficient mass transfer by delivering dissolved gas through the free surface, thus avoiding bubbles. This configuration prevents exceeding the mechanical stress threshold tolerated by the cells under study. The soft mixer achieves a maximum shear rate of $\gamma_{\max} \lesssim 0.4\,\text{s}^{-1}$ (Lefranc 2023) at the rotation speed used ($\Omega \sim 10$ rpm)for this application.

The soft mixer has also been tested as a photobioreactor to cultivate dinoflagellates, which are also fragile cells with a maximum shear rate of $\gamma_{\max}^{D} \sim 0.12\,\text{s}^{-1}$ (Lefranc 2023; Camacho *et al.* 2007). The low shear rate of the soft mixer increases the cells

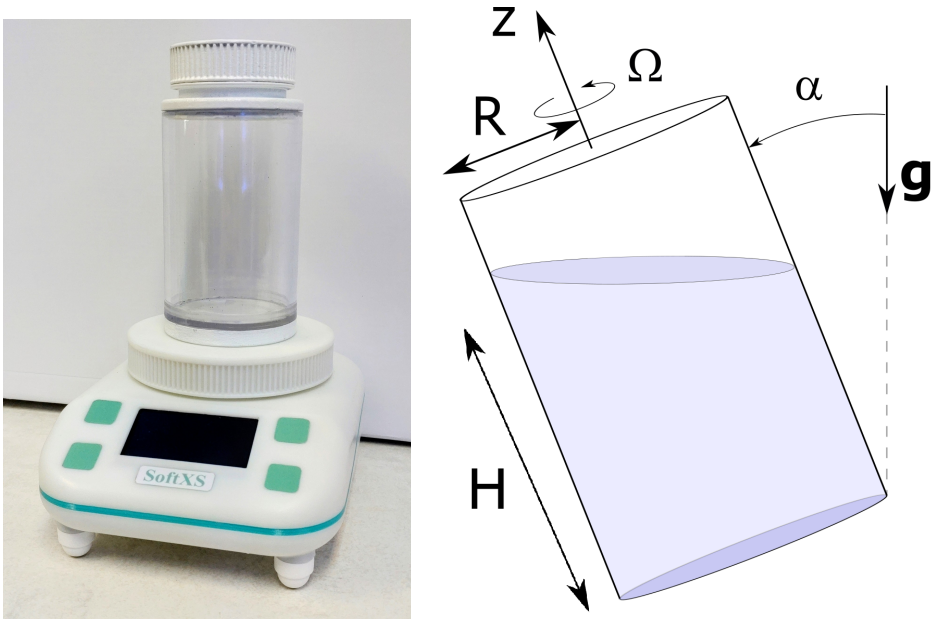


Fig. 1.2 Prototype for the growth of stem cells (courtesy of Softcell) on left. Scheme of the set up on the right, composed of a rotating tilted cylinder inserted inside an incubator (fixed at a temperature of 37° with an equilibrium concentration of $CO_2 \sim 5\%$). The height of the water is well controlled to keep the flow resonant.

duplication rate compared to traditional methods, achieving a production rate that is three times higher. Practical experience with this device suggests that production efficiency can be further optimized. In the high-cell-concentration phase, external light struggles to penetrate the dense central region, limiting cell proliferation. To address this, a transition from a cylindrical to an annular geometry has been proposed (Detournay & Meunier 2024), allowing light to reach the biomass from within. This alternate geometry will be studied in detail in the second chapter.

The soft mixer was designed by mimicking the flow dynamics of precessing fluids. The free surface creates a precessing boundary condition within the rotating frame, replicating the global flow observed in a precessing cylinder. Precessional flows have been widely studied in the geophysics community, particularly regarding Earth's precession and its potential role in generating a dynamo effect, a topic we will explore in the next section.

1.1.2 Geophysics

The Earth has an ellipsoidal shape, slightly flattened at the poles, with an equatorial diameter that is 43 km longer than its polar diameter, resulting in a reference geode diameter of 12.742 km. Beneath the surface, Earth is composed of several concentric layers (see Figure 1.4). The crust extends to a depth of about 35 km, followed by the mantle, which reaches down to 3.480 km. At the center lies the core, divided into the outer core, a liquid layer from 1.220 km to 3.480 km, and the inner core, a solid region

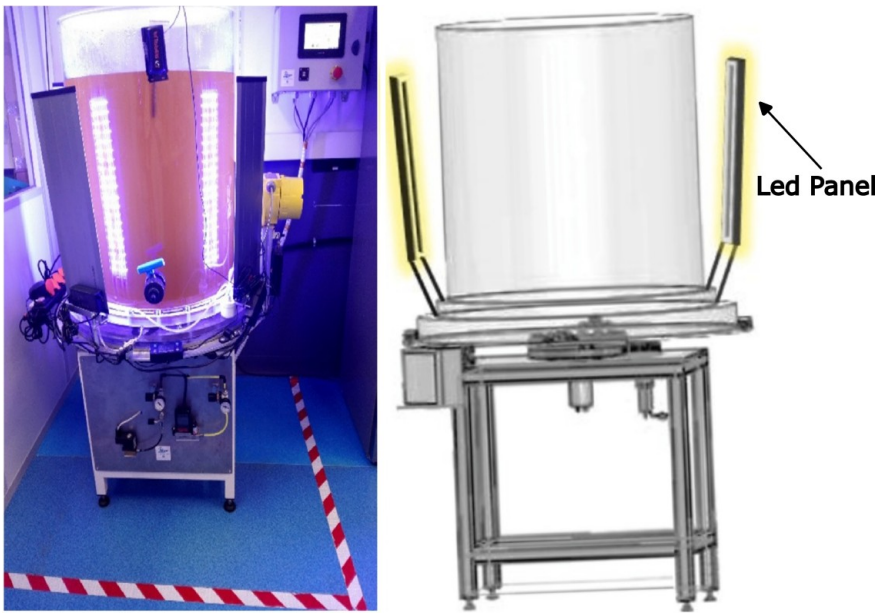


Fig. 1.3 On the left is an image of the soft mixer used for cultivating dinoflagellates (courtesy of Planktovie), and on the right, a diagram of the setup. The setup consists of a tilted cylinder placed on a rotating table, with transparent walls that allow light from an LED panel to pass through to support photosynthesis in the dinoflagellates. A flux of $C0_2$ is introduced from the bottom by a semipermeable membrane.

extending from 0 to 1.220 km. The outer core is composed primarily of liquid iron, with a viscosity similar to that of water, while the inner core consists of solid iron. In the outer core, pressures range from 130 to 330 GPa, and temperatures vary between 4.000 and 5.000 K. The interaction between the liquid outer core and the solid inner core drives convective currents within the outer core.

In a pioneering work, Larmor (1919) hypothesized that convective fluid motions within Earth's electrically conductive core could generate a magnetic dynamo sustaining the planet's magnetic field. For decades, physicists have studied thermal activity in the cores of planets, beginning with the seminal works of Roberts 1968 and Busse 1970, to validate this hypothesis. Indeed, it was later demonstrated that convective motions in planetary cores can create a dynamo effect (Glatzmaiers & Roberts (1995)).

In convection-driven geodynamo models, the energy available to generate turbulent flow through convection arises mainly from the solidification of the inner core, which heats the outer core through latent heat release. This effect is further enhanced by buoyancy forces, as light elements are expelled from the liquid iron as it cools. Using data on the planet's internal physics (Pozzo *et al.* 2012) and calculations of the core's thermal conductivity, it has been shown that convection at the core-mantle boundary alone is insufficient to sustain the geodynamo. Therefore, the presence of the inner core appears essential for maintaining the geodynamo.

Magnetized rock observations suggest that Earth's magnetic field is at least 3.4 billion years old (Landeau *et al.* 2022), spanning a period marked by significant changes

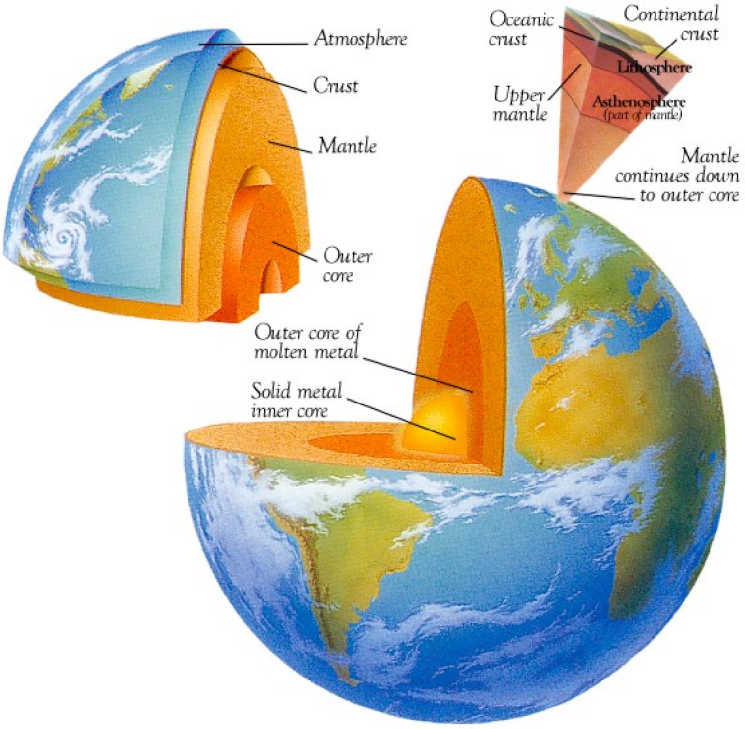


Fig. 1.4 Visualization of the Earth structure Shore (2013).

in the thermal dynamics of Earth's core. The inner core likely began to form less than 1 billion years ago, meaning that for over 2.4 billion years of the magnetic field's history, Earth's core was entirely liquid. Consequently, only part of the magnetic field's history can be attributed to buoyancy-driven forces.

This is why, despite skepticism regarding the possibility of a geodynamo due to precession (Rochester *et al.* 1975, Loper 1975), a debate has emerged about the interaction between convection, tidal forces, and precession in relation to the energy balance of magnetic field diffusion. This discussion opens new research horizons in understanding the support mechanisms of planetary magnetic fields, particularly through the application of precessing fluids (Le Bars *et al.* 2015, Landeau *et al.* 2022).

The flow is modeled by global modes excited by the harmonic forcing resulting from their erratic precession and the tidal forces caused by the gravitational coupling with other bodies in their planetary systems, as illustrated in Figure 1.5. In the following sections, we will describe the case of Earth's precession.

The Earth's rotation, which takes about 23 hours and 56 minutes, generates a centrifugal force that creates a bulge at the equator. The Earth's axis is tilted at an angle of 23 degrees relative to the plane of the ecliptic, which causes the seasonal cycle. Additionally, the Earth experiences a precessional motion, with its axis rotating around a direction perpendicular to the ecliptic plane in a cycle lasting approximately 25.800 years.

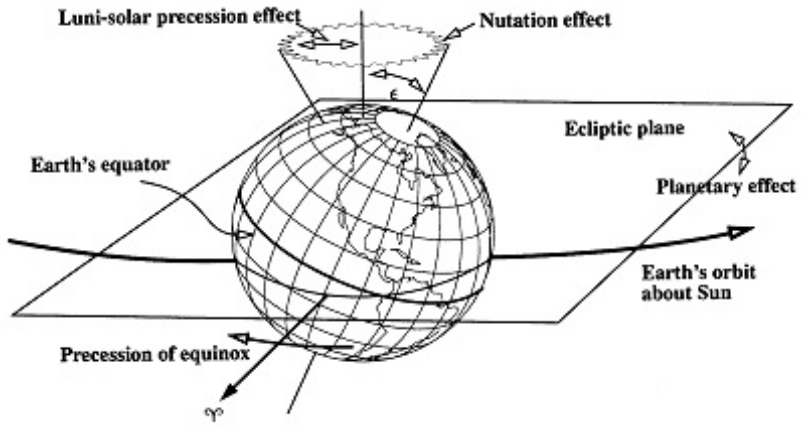


Fig. 1.5 Precession of the Earth (Taken from Meriggiola 2012).

Numerous studies have sought to determine whether the flow within Earth's outer core is laminar or turbulent under the influence of precession. These investigations are motivated by the observation that a turbulent regime in the outer core could generate sufficient energy to create currents strong enough to sustain the magnetic field (Kerswell 1996).

Following the theoretical study initiated by Kerswell (1993) on triadic instability, a parametric instability involving the nonlinear interaction of inertial modes (see Section 1.2.9.2 for more details), research has performed experiments (Noir *et al.* 2001, Nobili *et al.* 2021) and simulations (Lorenzani & Tilgner 2001,2003, Tilgner 2005, Ernst-Hullermann *et al.* 2013) to understand the instabilities generated by precessional motions in spheroids and spheroidal shells to underline the energy budget in the core of the Earth given by precession.

One of the first experiments aimed at demonstrating the possibility of creating a dynamo through precessional flow involved using molten sodium in a precessing cylinder (Gans 1971), but it did not yield positive results. However, a new experimental setup is currently being built and tested in Dresden following encouraging numerical results (Giesecke *et al.* (2018)).

One notable feature highlighted by experiments in a precessing cylinder is the inherent mixing capability of the various setups used. This property is actually commonly used in the industry. For example, industrial mixers use precession for high-viscosity fluids such as paint (known as biaxial mixers; see Figure 1.6). However, the presence of two axes of rotation increases the complexity of these setups.

Thanks to the experiment conducted by McEwan (1970) (see Figure 1.7), it is possible to switch to a simpler setup that mimics the precession forcing by tilted top end of the cylinder. The orientation of this tilted disc is rotated at Ω_p inside the rotating cylinder. This modification creates a harmonic forcing rotating in the cylinder's reference frame. Linear theory demonstrates that this type of forcing is equivalent to precession forcing with an azimuthal wavenumber $m = 1$.

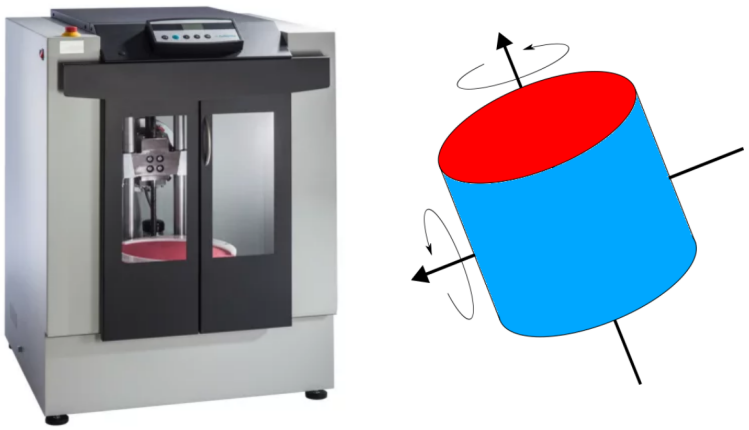


Fig. 1.6 Example of a biaxial mixer used in industry for mixing paint (Gyroscopic mixer BIAX 45 Copyright ©2024 Collomix). It can mix a pot of paint up to 50 kg in about 30s with a fast precession movement of the pot (around few rounds per minute (rpm)) as shown in the schematic drawing (Right).

A further simplification of this setup, as demonstrated by Meunier (2020), involves using a free surface of the liquid and tilting the axis of rotation with respect to gravity to apply harmonic forcing. It corresponds to the case where Ω_p is exactly opposite to Ω, such that the orientation of the tilted disc is motionless in the laboratory frame of reference. This system, presented earlier (see Figure 1.2), is referred to as a soft mixer. The physics of this setup will be described in the next section.

1.2 Dynamics of rotating flows

In this section, we will describe the mathematical treatment used in the manuscript by defining the notation and introducing all the equations used regarding the flow (as traditionally done Thompson 1970, Lagrange *et al.* 2009). For an exhaustive treatment of the subject, we refer the reader to the classic book Greenspan (1968) where all topics are exhaustively treated, or to Davidson (2024) where a modern and more user-friendly treatment can be found.

1.2.1 Rotating flows: Navier-Stokes equation

To describe a rotating fluid, it is essential to explain its kinematics in a non-Galilean reference frame. We define the laboratory frame, which is a Galilean frame, as $(T, \mathbf{X}')$ and the rotating frame, a non-Galilean frame, as $(T, \mathbf{X})$ (see Figure 1.8).

Let us consider an incompressible fluid of uniform density ρ and viscosity ν with vector position $\mathbf{X}(\mathbf{T})$ in the laboratory frame. If the fluid is in rotation with an angular

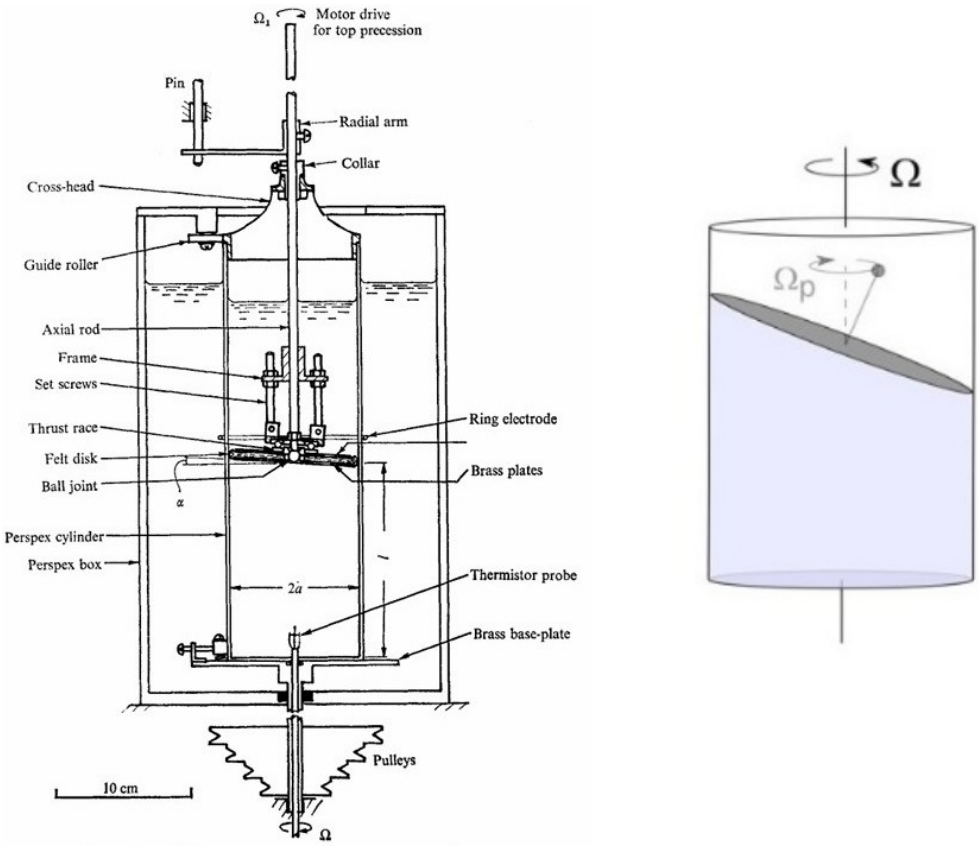


Fig. 1.7 Original experimental set-up used by McEwan (1970). The experiment used a top tilted plane that counter rotates with respect to the cylinder to create a harmonic forcing that equivalent to the forcing of precession.

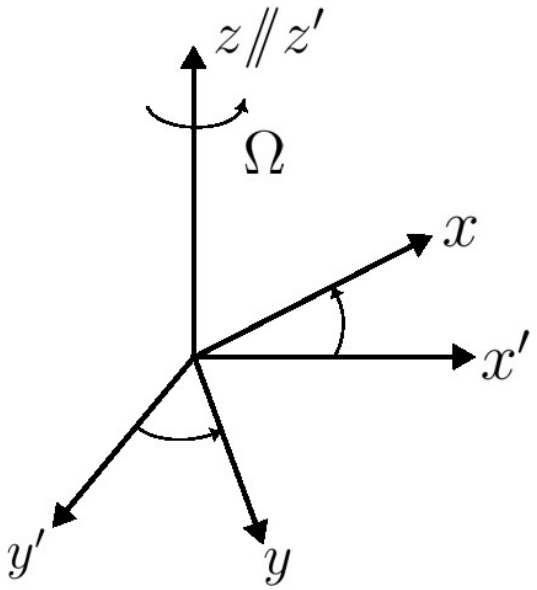


Fig. 1.8 Diagram illustrating the change of reference from a laboratory frame $(T, \mathbf{X}')$ to a rotating frame $(T, \mathbf{X})$.

velocity Ω, we have a general kinematics for the position:

$$\frac{d\mathbf{X}'}{dT} = \frac{d\mathbf{X}}{dT} + \mathbf{\Omega} \wedge \mathbf{X}, \tag{1.3}$$

which translates into the velocity addition:

$$\mathbf{U}' = \mathbf{U} + \mathbf{\Omega} \wedge \mathbf{X}, \tag{1.4}$$

where we have defined the velocities in the two different frames as $\mathbf{U}'(\mathbf{X}', T)$ and $\mathbf{U}(\mathbf{X}, T)$ in the respective frame.

We can then find the law of conversion of accelerations under the change of reference, by deriving the previous identity with respect to time and including the addition of velocity, we obtain the following identity

$$\begin{aligned} \frac{d\mathbf{U}'}{dT} =& \frac{d}{dT}(\mathbf{U} + \mathbf{\Omega} \wedge \mathbf{X}) + \mathbf{\Omega} \wedge (\mathbf{U} + \mathbf{\Omega} \wedge \mathbf{X}) \\ =& \frac{d\mathbf{U}}{dT} + 2\mathbf{\Omega} \wedge \mathbf{U} + \mathbf{\Omega} \wedge \mathbf{\Omega} \wedge \mathbf{X} + \left(\frac{d\mathbf{\Omega}}{dt}\right)' \wedge \mathbf{X} \end{aligned} \tag{1.5}$$

where we can recognize the Coriolis acceleration $A_{\text{Cor}} = -2\mathbf{\Omega} \wedge \mathbf{U}$, the centrifugal acceleration $A_{\text{cen}} = -\mathbf{\Omega} \wedge \mathbf{\Omega} \wedge \mathbf{X} = -\nabla|\mathbf{\Omega} \wedge \mathbf{X}|^2/2$ and the Poincaré acceleration $A_{\text{P}} = -(\frac{d\mathbf{\Omega}}{dt})' \wedge \mathbf{X}$. The Poincaré acceleration is defined in the inertial reference system, since the source of rotation are of two kind, intrinsic (with the $'$) and extrinsic (rotating of the frame).

In the case of a precessing system, where the axis of rotation of the container $\mathbf{\Omega}_{\text{spin}}$ is itself rotating at a constant angular velocity $\mathbf{\Omega}_{\text{p}}$ around a fixed axis of precession, the Poincaré acceleration can be expressed as follows

$$\left(\frac{d\mathbf{\Omega}}{dt}\right)' \wedge \mathbf{X} = \mathbf{\Omega}_{\text{p}} \wedge \mathbf{\Omega}_{\text{spin}} \wedge \mathbf{X}. \tag{1.6}$$

In the case of a rotating cylinder, we consider the stationary scenario where the rotation velocity $\mathbf{\Omega} = \Omega_{\text{spin}}$ is constant, i.e. $\Omega_{\text{p}} = 0$, resulting in the Poincaré acceleration term vanishing. This assumption holds throughout the entire manuscript.

To describe the dynamics of an incompressible fluid, we start in the laboratory reference frame, where the usual Navier-Stokes equation is expressed as follows:

$$\frac{d\mathbf{U}'}{dT} = \partial_T \mathbf{U}' + (\mathbf{U}' \cdot \nabla)\mathbf{U}' = -\frac{1}{\rho}\nabla P + \nu\nabla^2\mathbf{U}' - \nabla\phi, \tag{1.7}$$

where $\phi = gz$ is the gravitational potential per unit mass, with g representing the gravitational acceleration, and P is the pressure.

Therefore, taking into account the transformations described above, the Navier-Stokes equation in the rotating reference frame can be written as

$$\partial_T \mathbf{U} + (\mathbf{U} \cdot \nabla)\mathbf{U} = -\nabla\left(\frac{P}{\rho} + \phi + \frac{1}{2}|\mathbf{\Omega} \wedge \mathbf{X}|^2\right) - 2\mathbf{\Omega} \wedge \mathbf{U} + \nu\nabla^2\mathbf{U}, \tag{1.8}$$

which can be simplified by defining the reduced pressure $\tilde{P}/\rho = P/\rho + \phi + \frac{1}{2}|\mathbf{\Omega} \wedge \mathbf{X}|^2$. Incorporating the incompressibility condition, we obtain the following system of equations

$$\begin{cases} \partial_T \mathbf{U} + (\mathbf{U} \cdot \nabla)\mathbf{U} + 2\mathbf{\Omega} \wedge \mathbf{U} = -\frac{1}{\rho}\nabla\tilde{P} + \nu\nabla^2\mathbf{U} \\ \nabla \cdot \mathbf{U} = 0 \end{cases}. \tag{1.9}$$

As usual in fluid mechanics, we aim to identify appropriate scales to nondimensionalize the equations. Given that we are considering a fluid contained within a rotating cylinder, we can use $1/\Omega$ as the characteristic time scale, the radius of the cylinder R as the length scale, and ρR^3 as the mass scale. Defining the dimensionless variables $t = \Omega T$ and $\mathbf{x} = \mathbf{X}/R$, we obtain the dimensionless velocity $u = \mathbf{U}/(\Omega R)$ and pressure $p = \tilde{P}/(\rho\Omega^2 R^2)$. Using these definitions, we can rewrite the system as

$$\begin{cases} \partial_t \mathbf{u} + (\mathbf{u} \cdot \nabla)\mathbf{u} + 2\hat{\mathbf{\Omega}} \wedge \mathbf{u} = -\nabla p + E\nabla^2\mathbf{u} \\ \nabla \cdot \mathbf{u} = 0 \end{cases}, \tag{1.10}$$

where the derivatives are now dimensionless, $\hat{\mathbf{\Omega}}$ is the dimensionless unit vector of rotational velocity, and

$$E = \nu/(\Omega R^2) \tag{1.11}$$

is the Ekman number, representing the ratio between viscous forces and the Coriolis force. The Ekman number is usually very small and indeed this is the case in our work. This number is significant in rotating fluids, as it quantifies the thickness of the Ekman boundary layers ($\propto E^{1/2}$). These boundary layers strongly attenuate the flow and consequently influence the amplitude of modes within the cylinder, as will be discussed in the following sections.

Another important dimensionless number in the analysis of rotating fluids is the Rossby number

$$Ro = U/(\Omega R), \tag{1.12}$$

where U is the characteristic velocity of the flow in the rotating frame. The Rossby number represents the ratio of advective term to Coriolis term. This parameter is commonly used in studies of geophysical phenomena in the oceans and atmosphere, as it characterizes the relative importance of Coriolis accelerations resulting from planetary rotation, where the Rossby number is small and the nonlinear term can be neglected.

In the following sections, we will explore solutions to this equation, gradually increasing the complexity to develop a model that closely approximates experimental observations.

1.2.2 Solid Body rotation

The simplest solution occurring in Equation (1.10) is the stationary trivial solution $\mathbf{u} = 0$ and $p = constant$. In this case, the fluid follows the rotation of the rotating frame (the cylinder in our case).

We want to emphasize that this simple assumption actually conceals a transitional phase observed in experiments. When a cylinder filled with fluid is impulsively accelerated from rest to a fixed rotational speed, the fluid undergoes a transient regime known as spin-up (Weidman 1976, Weidman 1976). During this phase, the fluid gradually adjusts from rest as the shear forces exerted by the cylinder generate boundary layers along the sidewall and bottom wall, allowing angular momentum to adjust progressively from the edges to the axis of rotation. Once the spin-up time $t_{\text{spin-up}} = E^{-1/2}\Omega^{-1}$ (with this scaling derived from Ekman pumping, as discussed in Section 1.2.7) has elapsed, the system reaches the stationary solution described above. Throughout the cases we describe, we assume an initial condition of solid-body rotation, meaning that we focus on times after the spin-up period.

1.2.3 Geostrophic flow

In geophysics, geostrophic motion refers to the flow where the horizontal component of the Coriolis force, perpendicular to the gravitational vector $\mathbf{g}$, balances the pressure gradient force (Phillips 1963). The resulting geostrophic flow, denoted as $\mathbf{u}_0$, is a solution to Equation (1.10) under the assumption that both the Rossby number and the Ekman number are much smaller than 1. In this regime, we can neglect the nonlinear

terms and viscous forces, simplifying the equation to:

$$\partial_t \mathbf{u} = 2\hat{\mathbf{\Omega}} \wedge \mathbf{u} - \nabla p. \tag{1.13}$$

Further, considering the motion to be steady or quasi-steady allows us to neglect the term $\partial_t \mathbf{u}$, which simplifies the governing equations to

$$2\hat{\mathbf{\Omega}} \wedge \mathbf{u}_0 = -\nabla p_0, \tag{1.14}$$

so in this flow, the velocity is perpendicular to the pressure gradient, meaning that the streamlines coincide with the isobars.

This flow is fully described by the properties of the Taylor–Proudman theorem (Proudman 1916). To demonstrate this property, we can take the curl of the equation (1.14)

$$2\nabla \wedge \hat{\mathbf{\Omega}} \wedge \mathbf{u}_0 = -\nabla \wedge \nabla p_0 = 0, \tag{1.15}$$

where the left hand size is zero by definition, i.e. the gradient of a scalar field is conservative, that after some algebra lead to

$$\left(\hat{\mathbf{\Omega}} \cdot \nabla\right) \mathbf{u}_0 = 0. \tag{1.16}$$

This implies that the velocity of geostrophic flow remains uniform along the direction parallel to the axis of rotation, thus forming an essentially 2D flow. This concept also provides an explanation for the experimental phenomenology shown later by Taylor (1917), commonly referred to as 'Taylor columns'.

In Taylor's experiment (illustrated in Figure 1.9), a colored column is created in a fluid undergoing solid-body rotation, with an obstacle beneath it. This obstacle is slowly translated (toward the right in Figure 1.9) compared to the fluid in solid body rotation.

Due to the axial invariance of the flow (see equation (1.16)), the obstacle causes cylindrical streamlines to form around it. This effect is often described as if the fluid above the obstacle was inside an imaginary cylinder located above the obstacle and moving with the obstacle.

A nice way to visualize this phenomenon is to release a blob of dye at point A, above the obstacle. This dye moves, to the right and remains consistently aligned above the obstacle's center. In contrast, dye introduced at point B, positioned ahead of the column, is divided into two streaks as the obstacle passes beneath it.

This experiment provided the first evidence of how topographic constraints affect rotating fluids, showing that flow around obstacles is channeled in columnar structures aligned with the rotation axis, a fundamental concept in geophysical fluid dynamics.

Finally, we want to note the fact that this flow comes into play in the nonlinear description in the case of a cylinder in precession (Meunier *et al.* 2008, Lagrange *et al.* 2011, Gao *et al.* 2021).

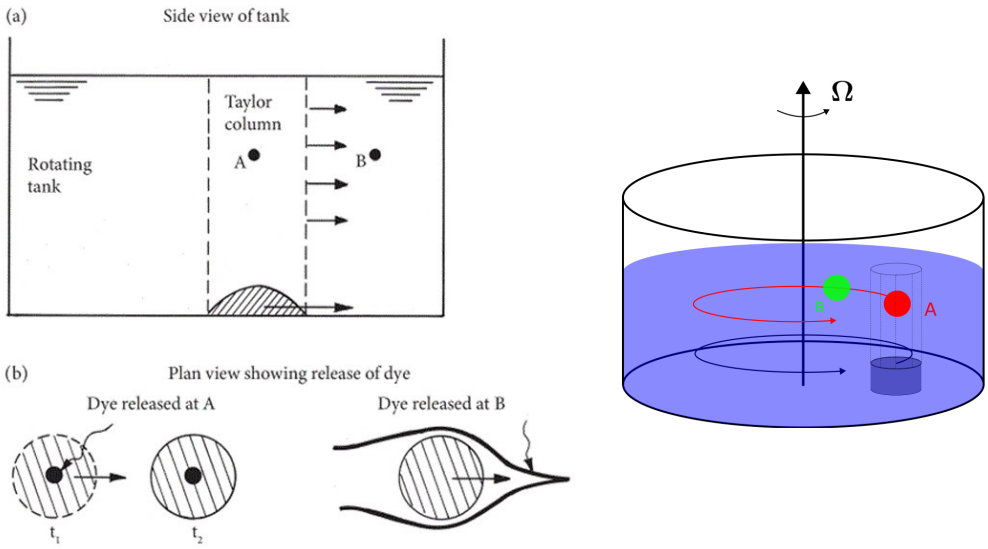


Fig. 1.9 Experimental set-up usually used to show the Taylor column, in side view (a), plan view (b) (picture taken from Davidson (2015)) and 3D version on the right. In a rotating tank in solid body rotation with a small obstacle two different dyes are put in the tank, one inside the Taylor column created by the obstacle A and the other outside B. Because of the Taylor column, it is observed that the dye A will follow the Taylor column while B will remain around the initial injection position where it is crossed by the imaginary cylinder created by the Taylor column.

Indeed, the z-invariant axysimmetric zonal flow is always weakly forced by nonlinear interactions. Since it is only weakly damped by viscous effects, it can saturate at a large amplitude and generate strong detuning effects.

1.2.4 Inertial waves

Previously we have described the stationary solutions of the linearized inviscid equation (1.13). Keeping the temporal derivatives, we can eliminate the pressure by taking the curl of (1.13), resulting in the expression

$$\partial_t \nabla \wedge \mathbf{u} - 2(\hat{\mathbf{\Omega}} \cdot \nabla)\mathbf{u} = 0. \tag{1.17}$$

By taking the curl of the previous expression once more and applying the incompressibility condition:

$$\partial_t(-\nabla^2 \mathbf{u}) - 2(\hat{\mathbf{\Omega}} \cdot \nabla)\nabla \wedge \mathbf{u} = 0, \tag{1.18}$$

which can be further simplified by differentiating with respect to time, thanks to the Equation (1.17) for the second term, we arrive at the Poincaré equation (Poincaré 1885)

$$\partial_t^2 \nabla^2 \mathbf{u} + 4(\hat{\mathbf{\Omega}} \cdot \nabla)^2 \mathbf{u} = 0. \tag{1.19}$$

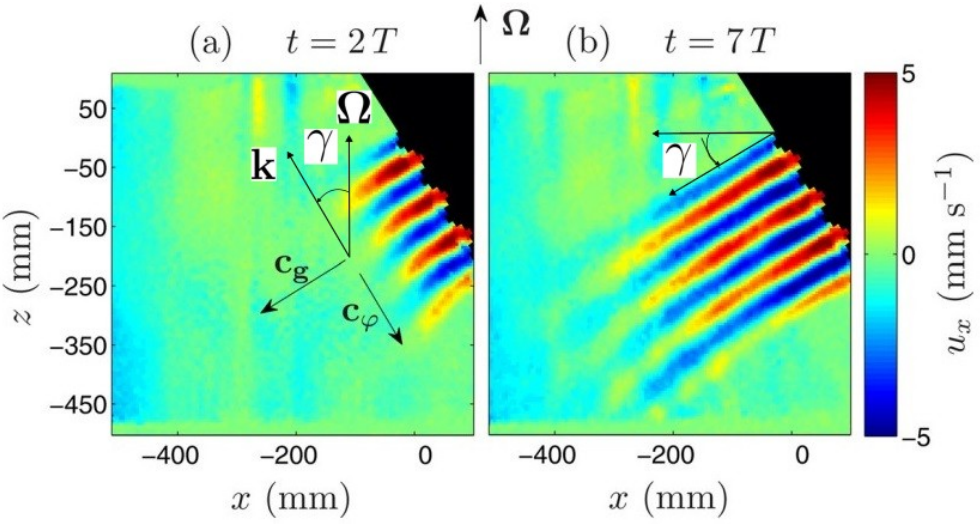


Fig. 1.10 Visualization of inertial waves in a rotating tank generated by a wavemaker (Bordes *et al.* 2012).

Assuming the rotation axis is parallel to z and taking $\mathbf{u} \propto e^{i\varpi t}$, we substitute into the equation, yielding

$$-\varpi^2 \nabla^2 \mathbf{u} + 4\partial_z^2 \mathbf{u} = 0, \tag{1.20}$$

which admits wave solutions of the form $\mathbf{u} \propto e^{i(\mathbf{k}\cdot\mathbf{x}+\varpi t)}$, allowing us to derive the dispersion relation as follows:

$$\varpi^2 = \frac{4(\mathbf{k}\cdot\hat{\mathbf{z}})^2}{k^2} \equiv 4\cos(\gamma)^2, \tag{1.21}$$

where γ is the angle between the wave vector $\mathbf{k}$ and the rotation axis see Figure 1.10.

From this dispersion relation, we observe that the frequency of the waves depends on the direction of the wave vector, but not on its magnitude. The frequency is bounded by $|\varpi| \leq 2$ with the maximum value occurring when the wave vector $\mathbf{k}$ is aligned with the axis of rotation ($\gamma = 0$).

From the incompressibility $\mathbf{k}\cdot\mathbf{u} = 0$, we conclude that the wave vector is orthogonal to the velocity of the fluid particles. The velocity along k at which the phase $t + kr$ of the inertial wave remains constant is called the phase velocity and is given by

$$\mathbf{c}_\varphi = \pm 2\frac{\mathbf{k}\cdot\hat{\mathbf{z}}}{k}\hat{\mathbf{k}} = \pm 2\cos(\gamma)\hat{\mathbf{k}}. \tag{1.22}$$

Since the phase velocity depends on the frequency, two inertial waves with different frequencies have phases that propagate at different speeds. This is referred to as a dispersive propagation of inertial waves.

The energy propagation speed associated with an inertial wave is called the group velocity and is given by

$$\mathbf{c}_g \coloneqq \partial_k \omega = \pm 2 \frac{\hat{\mathbf{k}} \wedge (\hat{\mathbf{z}} \wedge \hat{\mathbf{k}})}{k} = \pm 2 \frac{(\hat{\mathbf{z}} - \cos(\gamma)\hat{\mathbf{k}})}{k}, \tag{1.23}$$

and is orthogonal to the phase velocity.

An example of these waves is given in Figure 1.10. This experiment is conducted by a wavemaker in a rotating tank Bordes *et al.* (2012), demonstrating the properties discussed above.

For $\cos(\gamma) = 0$ we have $\omega = c_\varphi = 0$ and we recover the case of the geostrophic flow: it corresponds to Taylor columns since the flow is invariant in z because $\mathbf{k}$ is perpendicular to $\hat{\mathbf{z}}$.

1.2.5 Global Inertial modes: Kelvin modes

Inertial modes are defined as the solutions of equation (1.10) confined in a certain geometry, mathematically taking the right boundary conditions. Inertial modes in cylindrical geometry were initially studied by Kelvin (1880), referred to as Kelvin modes.

In a cylinder, the solution can be obtained by closing the problem in terms of pressure, with the ansatz $\mathbf{u} \sim \mathbf{u}_k(r) e^{i(m\theta + kz + \varpi t)}$ and $p \sim p_k(r) e^{i(m\theta + kz + \varpi t)}$, where m is the azimuthal wavenumber and k the axial wavenumber. Indeed, we can use equation (1.13) to express the identities

$$\begin{cases} \mathbf{u}_\perp = \frac{1}{4-\varpi^2}(i\varpi\mathcal{I} + i2\boldsymbol{\sigma}_y)\nabla_\perp p \\ w_k = -\frac{k}{\varpi} p_k \end{cases}, \tag{1.24}$$

where we have used $\mathcal{I}$ as the 2×2 identity matrix, $\boldsymbol{\sigma}_y = \begin{pmatrix} 0 & -i \\ i & 0 \end{pmatrix}$ is the second Pauli matrix and the subscript $\perp$ indicates the component in the plane orthogonal to the axis of rotation.

The solution is then forced by substituting w by $-ik/\varpi p$ in the axial component of the Poincaré equation (1.20), which leads to

$$\nabla^2 p_k - \frac{4k^2}{\varpi^2} p_k = 0. \tag{1.25}$$

This equation can then be written

$$\frac{d^2}{dr^2} p_k(r) + \frac{1}{r}\frac{d}{dr} p_k(r) + \left(\lambda^2 - \frac{m^2}{r^2}\right) p_k(r) = 0, \text{with} \quad \lambda = k\sqrt{4/\varpi^2 - 1}. \tag{1.26}$$

This is a Bessel equation with the solution $p_k(r) = J_m(\lambda r)$, where λ is the radial wavenumber, J is the Bessel function of the first kind. It is important to note that

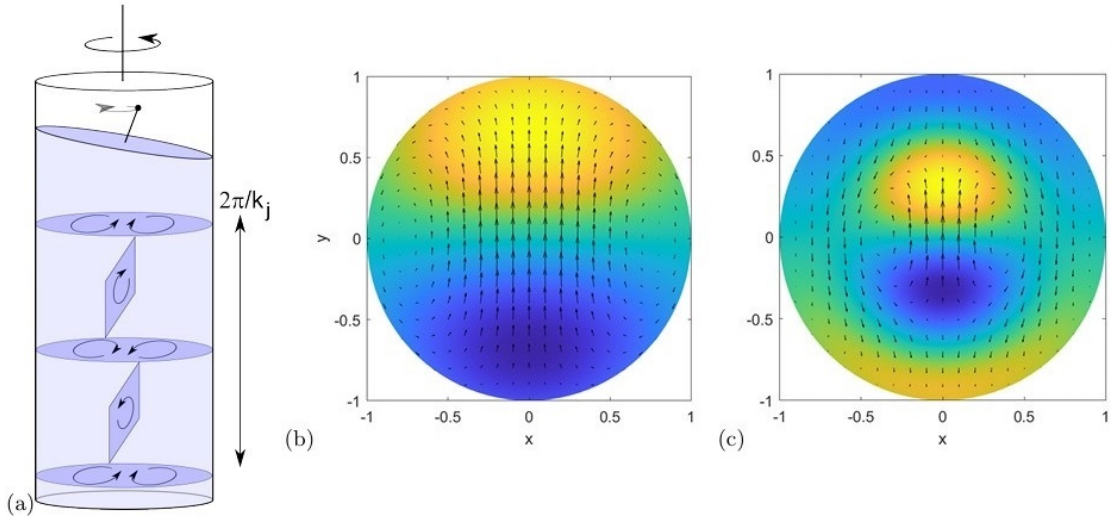


Fig. 1.11 Structure of Kelvin mode in the soft mixer with azimuthal wavenumber $m = 1$. A schematic drawing of the first mode $j = 1$ is given in (a). Velocity field and vorticity of the mode $j = 1$ (b) and $j = 2$ (c). The visualization is a horizontal cross section at $z = 0.2$, where the arrows show the velocity field (u, v) and the color map is the vorticity ω_z.

the radial and axial wavenumbers are proportional, with a ratio depending on the frequency ϖ. With this solution we can use the relations (1.24) to find the general flow

$$\begin{cases} u = -\frac{i}{4-\varpi^2}\left[\varpi\lambda J_{m-1}(\lambda r) + \frac{m(\varpi-2)}{r}J_m(\lambda r)\right]\cos(kz)e^{im\theta+\varpi t} \\ v = \frac{1}{4-\varpi^2}\left[2\lambda J_{m-1}(\lambda r) + \frac{m(\varpi-2)}{r}J_m(\lambda r)\right]\cos(kz)e^{im\theta+\varpi t} \\ w = -i\frac{k}{\varpi}J_m(\lambda r)\sin(kz)e^{im\theta+\varpi t} \end{cases} . \tag{1.27}$$

Here, we can observe that the choice of axial modulation ($p \propto \cos(kz)$) follows from the condition at the bottom of the cylinder, $w(z = 0) = 0$. Including the boundary condition on the side walls, $u(r = 1) = 0$, allows us to write the dispersion relation

$$(2 - \varpi)mJ_m(\lambda) + \lambda\varpi J_{m-1}(\lambda) = 0. \tag{1.28}$$

This dispersion relation provides the bound for frequencies, which must satisfy $|\varpi| < 2$. For a given frequency, the radial wavenumber has an infinite discrete number of roots λ_j. Each root λ_j corresponds to a radial profile with j lobes of the radial velocity (see Figure 1.11).

Finally, we want to conclude with an observation that connects the inertial modes with the inertial waves. In a remarkable paper, Waleffe (1990) demonstrated how these inertial motions can be described as a superposition of the inertial waves described above by considering the angle of $\gamma = \arccos(\varpi/2)$, see equation (1.21).

In the following section, we will introduce the boundary condition for our case. In particular, we will describe how the inertial modes are exited by the harmonic forcing of the free surface.

1.2.6 Forcing by the free surface

So far, we have expressed the solution in the most general form. We now want to specify the solution in accordance with the motion of the free surface in a soft mixer.

In a tilted rotating cylinder with a free surface (Figure 1.2), it is observed that the centrifugal force can deform the surface into a parabolic shape due to the equilibrium of fluid forces acting across it. This effect is quantified by the Froude number $Fr = R\Omega/g$. It is assumed to be small in this context, allowing us to model the free surface as a flat boundary. Under these conditions, we can describe the free surface in the cylinder's horizontal frame of reference, positioned at

$$\zeta(t,\theta) = h - \alpha r\cos(\theta + t), \tag{1.29}$$

where $h = H/R$ is the dimensionless height of fluid.

Taking the derivative of this position with respect to time allows us to express the resulting forcing, specifically the boundary condition for the forced axial velocity:

$$w(z = \zeta(t,\theta)) = \alpha r\sin(\theta + t). \tag{1.30}$$

This forcing has an azimuthal wavenumber $m = 1$ and a frequency $\varpi = 1$, characteristics imprinted on the base flow. These value of the frequency determines the radial wave number, defined in equation (1.26), as a function of the axial wavenumber $\lambda = \sqrt{3}k$. Solving the dispersion relation (1.28) for $m = 1$, yields an infinite number of axial wavenumbers k_j which are equal to $k_1 = 1.579$, $k_2 = 3.286$, $k_3 = 5.062$ and so on.

These modes can be forced by the free surface. We can search the solution as a superposition of all possible forced modes with the axial wavenumbers we derived, expressed as:

$$\mathbf{u} = \sum_{j=1}^{\infty} \mathrm{Re}\left[A_j \begin{pmatrix} u_j(r)\cos(k_j z) \\ v_j(r)\cos(k_j z) \\ w_j(r)\sin(k_j z) \end{pmatrix} e^{i(\theta+t)}\right] \quad , \quad p = \sum_{j=1}^{\infty} \mathrm{Re}\Big[A_j p_j(r)\cos(k_j z)e^{i(\theta+t)}\Big], \tag{1.31}$$

where

$$\begin{cases} p_j(r) = J_1(\sqrt{3}k_j r) \\ u_j(r) = -\frac{i}{3r}\left(J_1(\sqrt{3}k_j r) + \sqrt{3}k_j r J_0(\sqrt{3}k_j r)\right) \\ v_j(r) = \frac{1}{3r}\left(J_1(\sqrt{3}k_j r) + 2\sqrt{3}k_j r J_0(\sqrt{3}k_j r)\right) \\ w_j(r) = -ik_j J_1(\sqrt{3}k_j r) \end{cases} . \tag{1.32}$$

From this expression, we can derive the amplitude of the various modes by equating w at $z = h$ with equation (1.30)), leading to:

$$\sum_j A_j k_j J_1(\sqrt{3}k_j r)\sin(k_j h) = \alpha r. \tag{1.33}$$

Thanks to the orthogonality of these eigenmodes

$$\int_0^1 r J_1(\lambda_j r) J_1(\lambda'_j r) dr = 0, \text{ if } \quad j \neq j', \tag{1.34}$$

we can multiply the previous identity by $rJ_1(\sqrt{3}k'_j r)$ and integrate with respect to r to derive the expression for the amplitudes

$$A_j = \frac{\alpha F_j}{T_j \sin(k_j h)}, \tag{1.35}$$

with

$$F_j = \int_0^1 r^2 J_1(\sqrt{3}k_j r) dr = \frac{J_1(\sqrt{3}k_j)}{k_j^2}, \tag{1.36}$$

and

$$T_j = k_j \int_0^1 r J_1^2(\sqrt{3}k_j r) dr = \frac{k_j}{2}\left(1 + \frac{1}{k_j^2}\right) J_1^2(\sqrt{3}k_j). \tag{1.37}$$

Here we have used the fact that $J_0(\lambda_j) = -J_1(\lambda_j)/\lambda_j$ as given by the dispersion relation (1.28).

From equation (1.35), we observe that the amplitude A_j diverges when $\sin(k_j h) = 0$. This indicates that there is a resonance of the j-th Kelvin mode when the height of fluid h is a multiple of the half-wavelength, specifically when $h = nh_j$, where n is an integer and

$$h_j = \frac{\pi}{k_j}. \tag{1.38}$$

In experiments, it is possible to select the mode we want to observe by adjusting the height of water in the cylinder (Meunier 2020). In particular, in the soft mixer, we have chosen the mode in which the first resonance ($n = 1$) occurs for $k_1 = 1.579$, i.e. $h_1 = 1.9898$. In the experiments, we fill the cylinder to a height $h \approx 2$, where we observe a strong amplitude A_1 that is saturated by viscous effect.

The next section will explain this effect and how to incorporate it in the model.

1.2.7 Ekman layer

In the previous section, we neglected the effect of viscosity. This simplification is possible because, in the bulk of the cylinder (away from the rigid boundaries) the effect of viscosity is negligible. However, in the vicinity of the rigid walls, the dissipative effects become more pronounced, necessitating a local boundary layer theory(see Schlichting & Gersten 2017 for a didactic introduction).

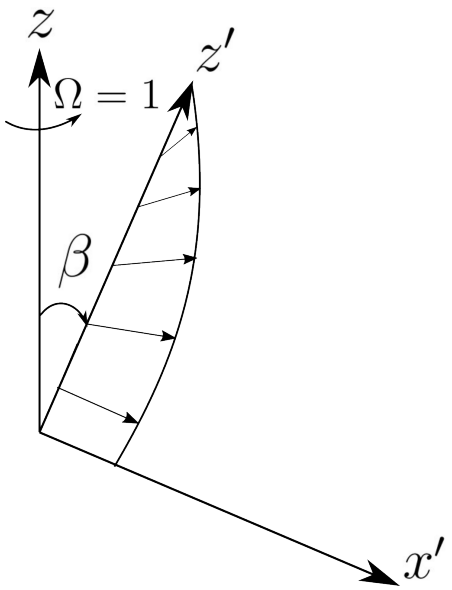


Fig. 1.12 Change of local co-ordinates to generalize the Ekman pumping calculation

In the context of rotating fluids, this problem was first addressed through the calculation of relative rotational motion between a fluid and a disc (Von Kármán 1921, Bödewadt 1940), and was subsequently generalized to fluids confined in a rotating vessel (Kudlick 1966, Greenspan 1968). In the following, we present an original and detailed derivation to arrive at a general identity used in this thesis.

In the Ekman layer, of depth $\delta \propto E^{1/2}$, there is an additional normal motion due to the Coriolis term which, unlike classical boundary layers, allows for an exchange of matter. This is why the resulting flow is referred to as Ekman pumping. This perturbation is of order $E^{1/2}$.

Following the boundary layer analysis, we separate the fluid velocity $\mathbf{u}$ into two terms: the inviscid solution $\mathbf{u}_b$ in the bulk, at frequency ϖ, which is valid far from the walls, and the boundary layer flow $\tilde{\mathbf{u}}$.

We define the flow as

$$\mathbf{u} = (\mathbf{u}_b + \tilde{\mathbf{u}})e^{i\varpi t}, \tag{1.39}$$

which evolves according to the equation

$$i\varpi\tilde{\mathbf{u}} + 2\hat{\mathbf{z}} \wedge \tilde{\mathbf{u}} + \nabla\tilde{p} - E\Delta\tilde{\mathbf{u}} = 0. \tag{1.40}$$

To perform this calculation, we consider a local (Cartesian) frame (x', y', z') aligned with the boundary layer, tilted by an angle β with respect to $\hat{\Omega}$, as shown in Figure 1.12. Defining the velocity in this frame leads to the following equations:

$$\begin{cases} i\varpi\tilde{u}' - f\tilde{v}' - E\Delta\tilde{u}' = -\partial_r\tilde{p} \\ i\varpi\tilde{v}' + f\tilde{u}' - E\Delta\tilde{v}' = -\frac{1}{r}\partial_\theta\tilde{p} \end{cases}, \tag{1.41}$$

where $f = 2\cos\beta$ represents the generalized orientation of the Coriolis force.

Inside the Ekman layer, the equation can be rewritten using the transformation $\tilde{z} = z'E^{-1/2}$ and $\hat{w}' = \tilde{w}'E^{-1/2}$ as follows:

$$\begin{cases} i\varpi\tilde{u}' - f\tilde{v}' - \partial_{\tilde{z}}^2\tilde{u}' = 0 \\ i\varpi\tilde{v}' + f\tilde{u}' - \partial_{\tilde{z}}^2\tilde{v}' = 0 \end{cases}, \tag{1.42}$$

since $\tilde{p}$ scales as E ($\partial_{\tilde{z}}\tilde{p} = -Ei\varpi\hat{w}$) and is therefore negligible.

The boundary condition is expressed as

$$\begin{pmatrix} u_b' + \tilde{u}' \\ v_b' + \tilde{v}' \\ \hat{w}' \end{pmatrix}\Bigg|_{z'=0} = 0, \tag{1.43}$$

ensuring that the total velocity vanishes at the boundary.

Assuming $(\tilde{u}, \tilde{v}) \sim e^{\tilde{z}/\delta}$ leads to four roots for δ, of which only two are physical, for the velocity to vanish at $\tilde{z} \to \infty$. The solution of this equation is given by

$$\begin{cases} \tilde{u}' = A_+e^{-\tilde{z}/\delta_+} + A_-e^{-\tilde{z}/\delta_-} \\ \tilde{v}' = iA_+e^{-\tilde{z}/\delta_+} - iA_-e^{-\tilde{z}/\delta_-} \end{cases}, \quad \begin{cases} A_+ = \frac{1}{2}[-iv_b(z=0) - u_b(z=0)] \\ A_- = \frac{1}{2}[iv_b(z=0) - u_b(z=0)] \end{cases}, \tag{1.44}$$

with the following roots:

$$\delta_+ = \begin{cases} \frac{1-i}{\sqrt{2(\varpi-f)}}, & \text{for } \varpi > f \\ \frac{1+i}{\sqrt{2|\varpi-f|}}, & \text{for } \varpi < f \end{cases}, \quad \delta_- = \begin{cases} \frac{1-i}{\sqrt{2(\varpi+f)}}, & \text{for } \varpi + f > 0 \\ \frac{1+i}{\sqrt{2|\varpi+f|}}, & \text{for } \varpi + f < 0 \end{cases}. \tag{1.45}$$

The incompressibility can be written as

$$\partial_{x'}\tilde{u}' + \partial_{y'}\tilde{v}' + \partial_{\tilde{z}}\hat{w}' = 0. \tag{1.46}$$

The normal flow, far from the boundary layer, is thus found to be

$$\hat{w}'(\tilde{z} = +\infty) = \int_{\bar{z}=0}^{\infty} (\partial_{x'}\tilde{u} + \partial_{y'}\tilde{v})\, d\bar{z}. \tag{1.47}$$

From the definition of the bulk flow vorticity $\omega_{z'} = \partial_{x'}v_b(z'=0) - \partial_{y'}u_b(z'=0)$, and using the incompressibility of the bulk flow, we find the solution

$$\hat{w}'(\tilde{z} = +\infty) = -\frac{1}{2}\partial_z w_b'(z=0)(\delta_+ + \delta_-) - \frac{i}{2}\omega_{z'}(\delta_- - \delta_+). \tag{1.48}$$

This expression corresponds to the Ekman pumping observed from outside the boundary layer. It can be simplified using the property of a Kelvin mode, $\boldsymbol{\omega}_b = (-i2/\varpi)\partial_z\mathbf{u}_b$, and written using vectors by defining a normal vector $\hat{n}$ directed inward as follows:

$$\tilde{\mathbf{u}}\cdot\hat{n} = \sqrt{E}\Big[-\frac{1}{2}(\delta_- + \delta_+)(\hat{\mathbf{n}}\cdot\nabla)(\mathbf{u}\cdot\hat{\mathbf{n}}) + \frac{1}{\varpi}(\delta_- - \delta_+)\hat{\mathbf{n}}\cdot\partial_z\mathbf{u}\Big]. \tag{1.49}$$

This equation is general for any wall as long as the axis of rotation is along $\hat{z}$. This identity is similar to equation (2.6.12) of Greenspan (1968). It is important to note that this treatment parallels the work of Wedemeyer (1966), where the solutions for the side and bottom boundaries are considered separately. The wedge between the two surfaces is assumed a negligible discontinuity in the pumping compared to the main pumping.

A different formula was obtained by Kudlick (1966) for geometries without wedge.

1.2.8 Application to a tilted rotating cylinder

In section 1.2.6, we calculated the inviscid solution by neglecting the dissipation term and imposing zero flow on the edges, which is valid away from the edges. Now that we have the flow expression in the boundary layers, we want to calculate the first-order correction of the forced mode, i.e. the Ekman pumping flow, to have the correct conditions at the edge.

This is done by considering the solvability condition (Meunier 2020), obtained by multiplying the linearized Navier-Stokes equation (1.10) with the complex conjugate of the jth mode $\bar{\mathbf{u}}_j = \Big(\bar{u}_j\cos(k_j z), \bar{v}_j\cos(k_j z), \bar{w}_j\sin(k_j z)\Big)e^{-i(\theta+t)}$ and integrating over the cylinder excluding Ekman boundary layers ($\tilde{V}$)

$$\iiint_{\tilde{V}} \bar{\mathbf{u}}_j\cdot\Big[i\mathbf{u} + 2\hat{\mathbf{z}}\wedge\mathbf{u} + \nabla p - E\nabla^2\mathbf{u}\Big]d^3r = 0. \tag{1.50}$$

Since the jth Kelvin mode is solution of equation (1.13), multiplying by $\mathbf{u}$ we find the expression

$$\begin{aligned} i\mathbf{u}\bar{\mathbf{u}}_j =& 2\mathbf{u}\cdot\hat{\mathbf{z}}\wedge\bar{\mathbf{u}}_j + \mathbf{u}\cdot\nabla\bar{p}_j \\ =& -2\bar{\mathbf{u}}_j\cdot\hat{\mathbf{z}}\wedge\mathbf{u} + \mathbf{u}\cdot\nabla\bar{p}_j \end{aligned}, \tag{1.51}$$

so the previous equation can be rewritten as

$$\iiint_{\tilde{V}} \Big(\mathbf{u}\cdot\nabla\bar{p}_j + \bar{\mathbf{u}}_j\cdot\nabla p - E\bar{\mathbf{u}}_j\cdot\nabla^2\mathbf{u}\Big)\,d^3r = 0. \tag{1.52}$$

The last simplification follows directly from the incompressibility with which the first two terms can be defined as a gradient

$$\nabla\cdot\left(\bar{p}_j\mathbf{u} + p\bar{\mathbf{u}}_j\right), \tag{1.53}$$

then using the Gauss theorem leads to

$$\oint_{\partial\tilde{V}} \left(\bar{p}_j \mathbf{u} + p\bar{\mathbf{u}}_j\right) \cdot \mathbf{n} d\Sigma - E \iiint_{\tilde{V}} \bar{\mathbf{u}}_j \cdot \nabla^2 \mathbf{u} d^3x = 0. \tag{1.54}$$

The first two terms we consider are the same as in the inviscid theory, as this approach extends what we have seen in the previous paragraph, from the first integral contribution at the free surface. The first term $\bar{p}_j \mathbf{u}$ integrated over the free surface gives a term that can be calculated as

$$\int_0^{2\pi} d\theta \int_0^1 r dr p_j(r) \cos(k_j h) w(z = \zeta(t, \theta)) = 2\pi\alpha i F_j \cos(k_j h), \tag{1.55}$$

where F_j is defined in equation (1.36). Here, the velocity w has been calculated by Equation (1.31).

The second term is given by the inviscid mode, defined in (1.31), that gives

$$\int_0^{2\pi} d\theta \int_0^1 r dr p_j(r) \cos(k_j h) A_j w_j(r) \sin(k_j h) = -2\pi i A_j T_j \cos(k_j h) \sin(k_j h), \tag{1.56}$$

where T_j is defined in equation (1.37). Here the pressure p is defined in Equation (1.32).

The first correction we consider is the contribution of Ekman pumping defined in equation (1.49) in the first integral on the side and bottom walls.

On the side wall the integral of $p\bar{\mathbf{u}}_j$ with $u = \tilde{u}$ gives a term

$$\int_0^{2\pi} d\theta \int_0^h dz p_j(r = 1) \cos(k_j z) \left(-\tilde{u} e^{-i(\theta+t)}\right) = A_j E^{1/2} C, \tag{1.57}$$

where

$$C_j = \pi h \frac{1+i}{2} (1 + k_j^2) J_1^2(\sqrt{3} k_j) \left(1 + \frac{\sin(2k_j h)}{2k_j h}\right). \tag{1.58}$$

On the bottom we have

$$\int_0^{2\pi} d\theta \int_0^1 r dr p_j(r) \tilde{w} e^{-i(\theta+t)} = A_j E^{1/2} B, \tag{1.59}$$

where

$$B_j = -6\pi k_j^2 \left(\frac{1-i}{2\sqrt{2}} + \frac{1+i}{6\sqrt{6}}\right) T_j. \tag{1.60}$$

The last correction is given by the integral of the Laplacian term that is found to be

$$E \iiint_{\tilde{V}} \bar{\mathbf{u}}_j \cdot \nabla^2 \mathbf{u} d^3x = 4k_j^2 A_j E \|\mathbf{u}_j\|^2. \tag{1.61}$$

where the norm of the eigenmodes can be calculated analytically (Gao *et al.* 2021):

$$\|\mathbf{u}_j\|^2 = \frac{2\pi h}{3}\left(2k^2 + J_1^2(\lambda)\right). \tag{1.62}$$

Introducing these terms in (1.54) leads to the correct amplitude at order E of the forced modes

$$A_j = \frac{\alpha f_j}{\sin(k_j h) - \frac{s_j}{\cos(k_j h)}E^{1/2} - \frac{v_j}{\cos(k_j h)}E}, \tag{1.63}$$

where we have defined the forcing coefficient

$$f_j = \frac{F_j}{T_j}, \tag{1.64}$$

that describes the saturation value of the forced mode. The surface coefficient

$$s_j = \frac{B_j + C_j}{2\pi i T_j}, \tag{1.65}$$

is a very important coefficient describing the saturation of amplitudes at small Ekman number. Indeed, at resonance (when $\sin(k_j h) = 0$), the amplitudes is equal to $A_j = -\alpha f_j / s_j E^{1/2}$ at leading order.

The volumetric coefficient

$$v_j = \frac{4k_j^2\|\mathbf{u}_j\|^2}{2\pi i T_j}, \tag{1.66}$$

induces a correction to the saturation value of amplitudes at order E.

To conclude this section, the base flow inside a tilted rotating cylinder is a sum of Kelvin modes defined in Equation (1.31), with amplitudes given by (1.63).

1.2.9 Stability of the flow

1.2.9.1 Centrifugal Instability

In a seminal paper, Rayleigh (1917) studied the motion of a non-viscous fluid in a cylinder and demonstrated a criterion of stability using Kelvin's circulation theorem and energy balance arguments. His argument begins with the observation that by expressing Euler's equation in cylindrical coordinates for an incompressible, axisymmetric fluid, one can derive the identity

$$\frac{Dru_\phi}{Dt} = 0, \tag{1.67}$$

where $\frac{D}{Dt} = \partial_t + u_r\partial_r + u_z\partial_z$ is the material derivative in cylindrical coordinates for an axisymmetric flow.

In other words, under these conditions, angular momentum $L = ru_\phi$ is conserved.

Since angular momentum is constant in the absence of viscosity, the kinetic energy per unit mass can be written as

$$K = \frac{1}{2}\frac{L^2}{r^2}. \tag{1.68}$$

Considering two fluid parcels located at distances r_1 and r_2, with $r_2 > r_1$, the total energy per unit mass is given by

$$K = \frac{1}{2}\left(\frac{L_1^2}{r_1^2} + \frac{L_2^2}{r_2^2}\right). \tag{1.69}$$

If we switch the two parcels, the energy becomes

$$K' = \frac{1}{2}\left(\frac{L_2^2}{r_1^2} + \frac{L_1^2}{r_2^2}\right). \tag{1.70}$$

The resulting difference in energy is

$$\Delta K = \frac{1}{2}\left(L_2^2 - L_1^2\right)\left(\frac{1}{r_1^2} - \frac{1}{r_2^2}\right). \tag{1.71}$$

For the flow to be stable under this transformation, the change in energy must be positive. This condition is satisfied if and only if

$$L_2^2 - L_1^2 > 0 \quad \Longleftrightarrow \quad \frac{dL^2}{dr} > 0. \tag{1.72}$$

Thus, we can present the stability criterion of Rayleigh as

$$\frac{\partial L^2}{\partial r} = \frac{\partial (r^2 u_\phi)^2}{\partial r} > 0. \tag{1.73}$$

In descriptive terms, stability is achieved when there is an angular stratification of momentum that remains constant or increases monotonically with r. Figure 1.13 provides a visualization of the associated instability.

This criterion is typically defined in the form:

$$\phi(r) = \frac{1}{r^3}\frac{\partial (r^2 u_\phi)^2}{\partial r} > 0, \tag{1.74}$$

which makes the criterion explicit as a function of the growth rate of the instability, given by $\sigma \sim \sqrt{-\phi(r)}$, as extensively described in the book of Chandrasekhar (1961).

This criterion was extended by Taylor (1923), demonstrating that the role of viscosity is primarily to delay the onset of centrifugal instability (a general discussion of this case can be found in Chandrasekhar 1961).

From an experimental standpoint, centrifugal instability can arise in any flow that is influenced by a wall, leading to a pressure gradient perpendicular to the streamlines.

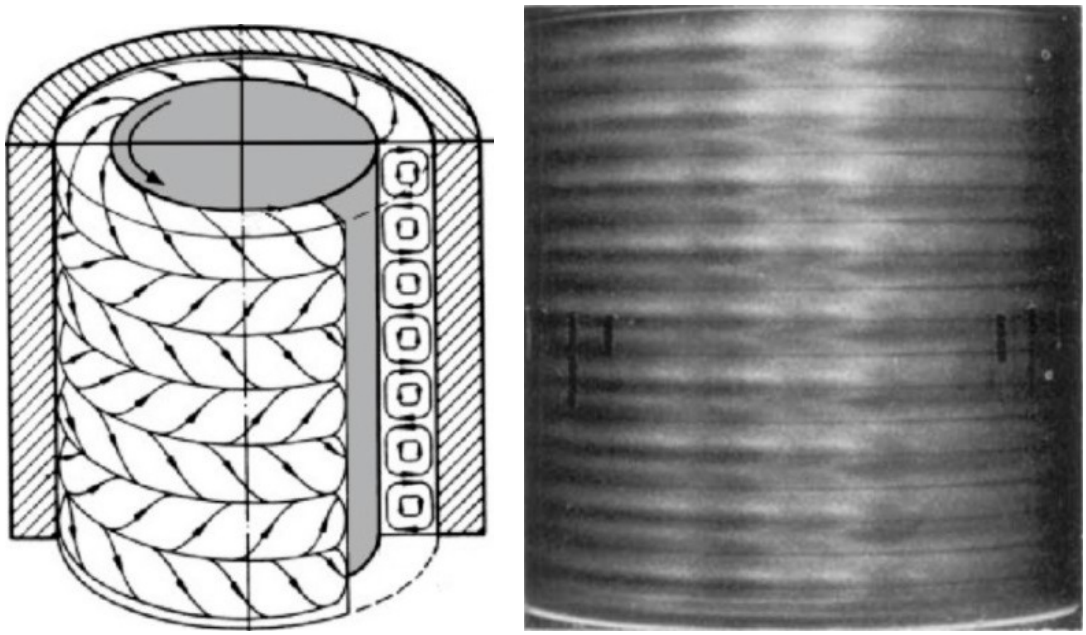


Fig. 1.13 Diagram of the set-up creating a Taylor–Couette flow, left (Meironke & Klembt 2019), used to visualise the centrifugal instability on the right (Fenstermacher *et al.* 1979).

A well-known example of this phenomenon is the Taylor–Couette flow, which occurs between two coaxial cylinders rotating at different angular velocities. Depending on the two Reynolds numbers calculated from these angular velocities and the ratio of the cylinder radii, a stationary, spatially structured flow can emerge. This structure is characterized by counter-rotating toroidal vortices and exhibits periodicity in the axial direction (see Figure 1.13). The formation of these vortices is a direct consequence of centrifugal instability.

We will revisit this type of instability in our study to assess its presence in the case of a soft mixer.

1.2.9.2 Triadic Instability

In rotating flows, triadic instability was first studied in the context of three-dimensional destabilization of two-dimensional rotating flows characterized by elliptical streamlines, a phenomenon referred to as elliptical instability (see the review by Kerswell 2002). This instability arises from a resonance between the normal waves of an undisturbed circular flow and the underlying deformation field, which has an azimuthal wavenumber $m = 2$. The linear growth rate is proportional to the deformation rate.

The instability complicates the flow, quickly leading to a breakdown into small-scale disorder, which has acquired significant interest within the turbulence research community. This phenomenon is crucial in various contexts, including planetary cores and accretion disks, where the perturbed system exchanges energy and angular momentum.

This instability was independently discovered in the 1970s in the West and in Russia. In the West, Crow (1970) identified a three-dimensional long-wavelength instability in vortex pairs, driven by the resonance of Kelvin waves within the vortex filament and external straining field imposed by the other vortex filament. Subsequent studies by Widnall *et al.* (1974), Moore & Saffman (1975) and Tsai & Widnall (1976) found that the same mechanism applies to short Kelvin waves, which create weak elliptical distortion in the global streamlines. Later, Robinson & Saffman (1984) demonstrated through numerical computation that this qualitative behavior also holds true under finite strain.

In Russia, Obukhov's group studied fluid-filled rotating ellipsoids, revealing unexpected instabilities (Gledzer *et al.* 1974). Later, Gledzer (1975) investigated elliptical cylinders and found a similar instability. He observed that a linear stability analysis could be developed in the limit of vanishing ellipticity, predicting the instability of two inertial waves with azimuthal wavenumbers $m = \pm 1$ fixed in the frame of the elliptical distortion. Further studies on the geometry of the ellipsoid led to the development of a similar stability analysis that involved both axisymmetric modes and modes with an azimuthal wavenumber $m = \pm 2$ (Gledzer & Ponomarev 1977).

In the 1980s, Pierrehumbert (1986) and Bayly (1986) rediscovered the phenomenon in an elongated uniform vortex, demonstrating its instability to three-dimensional disturbances. Subsequent studies by Landman & Saffman (1987) and Waleffe (1989,1990) further clarified the physical mechanism involved and the effects of viscosity, predicting that the instability saturates supercritically. These studies highlighted the complex nonlinear interactions among triad modes, which confirmed the experimental observation made by Malkus (1989). More recently, Eloy & Le Dizès (1999) examined the viscous effects on the linear stability of Burgers and Lamb–Oseen vortices subjected to a perpendicular strain field.

In all these elliptic instabilities, the elliptical base flow, characterized by an azimuthal wavenumber $m = 2$, can couple two infinitely small Kelvin modes with azimuthal wavenumbers m' and m'' separated by 2, leading to their exponential growth through nonlinear interactions. These interactions occur only under specific triadic resonance conditions, which can be generally expressed as:

$$\begin{cases} |m'' - m'| = m \\ |k'' - k'| = k \\ |\varpi'' - \varpi'| = \varpi \end{cases} . \tag{1.75}$$

Here, we have used the notation introduced before for the Kelvin modes ($u \sim e^{i(\varpi t + m\theta + kz)}$). For the elliptic base flow, the associated elliptic deformation is treated as a degenerate Kelvin mode with $m = 2$, $k = 0$ and $\varpi = 0$.

In addition to the previously discussed cases, this resonance condition has also been experimentally observed in precessing cylinders (Meunier *et al.* 2008, Lagrange *et al.* 2008, Lagrange *et al.* 2011). In these cases, the base flow is more complex, as both k and ϖ are non-zero, with $m = 1$, corresponding to the forced Kelvin mode described

in section 1.2.6. A weakly nonlinear theory was developed that also considered the coupling with the geostrophic flow within the cylinder. Subsequent numerical studies confirmed these theoretical results (Albrecht *et al.* 2015,2016), validating the theory even for parameters that significantly deviate from the initial assumptions.

The work conducted during this thesis on this instability directly builds upon the findings in precessing cylinders, following a similar line of reasoning to identify differences in the various coefficients of linear stability while preserving the same underlying physics.

Following the work of Lagrange *et al.* (2011), we now introduce the formalism employed in our analysis. The theory is based on the linear stability analysis of the full Navier-Stokes equation (1.10) with a resonant forced Kelvin mode u_j defined in equation (1.31), with an amplitude A_j given by (1.63). This forced mode interacts with two free modes, u' and u'', resulting in the definition:

$$\mathbf{u} = A_j \mathbf{u}_j + A' \mathbf{u}' + A'' \mathbf{u}''. \tag{1.76}$$

The forced Kelvin mode u_j, which is the base flow, has a Fourier component represented as $e^{i(k_j z+\theta+t)}$, with an azimuthal wavenumber $m = 1$ and frequency $\varpi = 1$. We assume that the amplitude of this forced mode is small, such that it serves as a perturbation parameter: $A_j \propto \alpha E^{-1/2} \ll 1$. At resonance, α is assumed small and E not too small for this condition to hold. This leads to a range of validity for E, situated in a transient regime between stable flow and the onset of turbulence.

We search for a linear expansion of the free modes:

$$\mathbf{u}' = \mathbf{u}'_{(0)} + A_j \mathbf{u}'_{(1)} + \mathcal{O}(A_j)^2, \ (' \to ''). \tag{1.77}$$

At the zero order of this expansion, we arrive at the inviscid equation

$$\partial_t \mathbf{u}'_{(0)} + 2\hat{\mathbf{z}} \wedge \mathbf{u}'_{(0)} = -\nabla p'_{(0)}, \ (' \to ''). \tag{1.78}$$

This indicates that $\mathbf{u}'_{(0)}$ and $\mathbf{u}''_{(0)}$ are free Kelvin modes, as described by equation (1.27).

Assuming a slow growth of the free modes, characterized by $\partial_t A' \sim \mathcal{O}(A_j)$, the first order equation for the Fourier component $e^{i(k'' z+m''\theta+\varpi'' t)}$ is given by the expression

$$\mathcal{L}\mathbf{u}''_{(1)} + (\partial_t A'')\mathbf{u}''_{(0)} = \left[\mathbf{u}'_{(0)} \wedge \nabla \wedge \mathbf{u}_j + \mathbf{u}_j \wedge \nabla \wedge \mathbf{u}'_{(0)}\right] A' A_j. \tag{1.79}$$

The nonlinear forcing term on the right-hand side shares the same Fourier component as u'' if and only if the following conditions are met:

$$\begin{cases} m'' = m' + 1 \\ k'' = k' + k_j \\ \varpi'' = \varpi' + 1 \end{cases}. \tag{1.80}$$

These conditions clarify the resonance requirements necessary for triadic instability. The third condition is only satisfied for specific values of m' and m'' since ϖ' and ϖ''

are determined by the dispersion relation. For a tilted rotating cylinder at $h = 1.95$ this condition is satisfied with $m' = 5$ and $m'' = 6$. This is exactly what is observed in the experiments (Lagrange *et al.* 2008).

Multiplying by the adjoint mode of $\mathbf{u}''_{(0)}$ and integrating over the volume allows the first term to vanish, leading us to an amplitude equation for A'. By following a similar procedure for $\mathbf{u}'_{(0)}$, we arrive at the amplitude equations:

$$\begin{cases} \partial_t A' = N' \bar{A}_j A'' \\ \partial_t A'' = N'' A_j A' \end{cases}, \tag{1.81}$$

where $\bar{.}$ denotes complex conjugate. N' and N'' are analytical coefficients describing the nonlinear interaction, which are defined in Section 2.7.2.

Assuming an exponential growth for the amplitudes $A', A'' \sim e^{\sigma t}$ we derive the inviscid growth rate

$$\sigma = \sqrt{N'N''}|A_j|. \tag{1.82}$$

It is possible to correct this growth rate with Ekman pumping, that leads to the viscous threshold for the instability. It is in excellent agreement with the experiments for a cylinder (Meunier 2020). This theory will be further elaborated in Section 2.7.2 for an annular geometry.

1.3 Mixing

1.3.1 General Introduction to Mixing

In the annual review by Villermaux (2019), a comprehensive introduction to mixing is presented, which will be referenced in this paragraph.

Let us consider a passive scalar concentration field c within a flow $\mathbf{u}$, where its evolution is governed by the advective-diffusion equation:

$$\partial_t c + \nabla (\mathbf{u} c) = D \nabla^2 c, \tag{1.83}$$

where D is the diffusivity coefficient.

In the case of incompressible flow ($\nabla \cdot \mathbf{u} = 0$) this equation simplifies to

$$\partial_t c + (\mathbf{u} \cdot \nabla) c = D \nabla^2 c, \tag{1.84}$$

which is the case throughout the manuscript.

The equation above illustrates that the evolution of the concentration field is inextricably due to the two mechanisms of advection by the external field and diffusion due to the Brownian motion of the scalar molecules. This interplay is also evident in the experimental study of mixing in gas-gas, gas-liquid and liquid-liquid phases, where the evolution of the concentration field of a dye provides a means to quantify

the mixing process. Let us first explore the effects of advection and diffusion when considered separately.

In the case where we exclude diffusion ($D = 0$)[1], we are left with the equation

$$\frac{Dc}{Dt} = \partial_t c + (\mathbf{u} \cdot \nabla)\, c = 0, \tag{1.85}$$

which indicates that, from a Lagrangian perspective, the concentration of a fluid particle remains constant along its trajectory. Thus, while the fluid's position changes, the concentration value does not vary, resulting in a reshuffling of the concentration field without mixing. This implies that a macroscopic stirring process can elongate the concentration field into substructures that retain the same concentration value, failing to achieve the molecular-scale homogenization necessary for effective mixing.

Conversely, if we do not apply any external agitation ($\mathbf{u} = 0$), the problem is governed by diffusion

$$\partial_t c = D\nabla^2 c. \tag{1.86}$$

In this case, we can find an analytical solution to the diffusion equation using the Green's function:

$$c_{\mathrm{G}}(\mathbf{x}, t) = \frac{1}{(\pi 4Dt)^{3/2}} e^{-\frac{x^2}{4Dt}}. \tag{1.87}$$

This solution corresponds to the kernel of equation (1.86) with an impulse forcing described by Dirac's delta function $\delta(t)\delta(\mathbf{x})$.

Taking an initial distribution $c_0(\mathbf{x})$, the solution can be described as a convolution with the Green function

$$c(\mathbf{x}, t) = (c_{\mathrm{G}} * c_0)\,(\mathbf{x}, t) \coloneqq \int d^3y c_{\mathrm{G}}(\mathbf{x} - \mathbf{y}, t) c_0(\mathbf{y}). \tag{1.88}$$

This formulation allows us to study the evolution of the concentration field by analyzing Green's function, thereby gaining insights into the underlying physics of the diffusion process.

The first observation concerns the evolution of the maximum concentration, which decreases according to a power law $c_{\max} \propto (Dt)^{-d/2}$, with d is the dimension of the space, highlighting that Brownian motion is essential for observing changes in the concentration value. Furthermore, the evolution of Green's function allows us to define the growth of the support, commonly referred to as the diffusive thickness, which evolves as $\sim \sqrt{Dt}$. However, this diffusion process is slow for mixing; for instance, considering the diffusion coefficient of water $D \sim 10^{-5}\mathrm{cm}^2\mathrm{s}^{-1}$, a dyed portion with a size of 1 cm would result in a mixing time of approximately $\sim 10^5$s.

An elegant perspective on the role of diffusion was derived by Zeldovich (1937). He started from the advection-diffusion equation (1.84) and examined the evolution of

[1]This scenario is, of course, non-physical, as diffusion always occurs due to random collisions with the external fluid, which remains in agitation at a finite temperature. However, we can consider this limit as a case of scale separation, particularly when examining a stirring process that is fast enough to minimize the effects of diffusion.

fluctuations in the concentration field within a closed volume. Multiplying the equation by c and integrating over the entire volume, with the boundary condition $\mathbf{u} = 0$ at the boundary, the advective term simplifies as follows

$$\int d^3x c\,(\mathbf{u}\cdot\nabla)\,c = \frac{1}{2}\int d^3x \nabla(\mathbf{u}c^2) = \frac{1}{2}\oint (\mathbf{u}c^2)\cdot\hat{\mathbf{n}}d\Sigma = 0, \tag{1.89}$$

indicating that it has no effect on the fluctuations due to incompressibility.

Similarly, applying this treatment to the diffusive term yields

$$D\int d^3x c\nabla^2 c = D\left[\int d^3x \nabla\cdot(c\nabla c) - \int d^3x\,(\nabla c)^2\right] = -D\int d^3x\,(\nabla c)^2\,, \tag{1.90}$$

where the flux term is zero, resulting from the conservation of mass, which implies that $\nabla c\cdot\hat{\mathbf{n}} = 0$ at the boundary.

Taking all these considerations into account, we can express the evolution of fluctuations as follows

$$\partial_t\left(\langle c^2\rangle - \langle c\rangle^2\right) = -2D\langle(\nabla c)^2\rangle. \tag{1.91}$$

This equation quantitatively illustrates that the fluctuations in the concentration field decay in response to the gradients present when diffusion is involved. Intuitively, this means that the fluxes generated by diffusion work to smooth out the fluctuations of concentration field throughout the volume.

We are now ready to revisit the complete case of the advection-diffusion equation (1.84). While we aim to utilize the Green's function method for this equation, it is crucial to note that the exact fundamental solution of equation (1.86) is only valid when the advection velocity is uniform.

To advance in this direction, we are helped by the observation that self-similarity emerges in the evolution of a passive scalar: it form strips in the 2D case (Ottino 1989) and sheets in the 3D case (Buch & Dahm 1996, Fountain *et al.* 1998).

From these observations, it is natural to seek a framework that enables a simplified model description of the concentration field. This search has led to the definition of lamellae in 2D (Meunier & Villermaux 2003, Villermaux & Duplat 2003, Duplat & Villermaux 2008) and sheets in 3D (Martínez-Ruiz *et al.* 2018, Meunier & Villermaux (2022)). In these models, there exists a predominant direction of elongation where advection is the dominant mechanism, while the transverse direction is sufficiently small to allow diffusion to be efficient (see Figure 1.14).

These structures are formed by the strain rate tensor (Betchov (1956)), which, in the incompressible case, produces a primary space of elongation and a secondary direction of compression. This configuration allows diffusion to become efficient only in the direction of compression, while stretching is oriented in the direction of elongation.

With this in mind, we rewrite the equation (1.84) in a frame that follows the scalar and rotates with the orientation of the sheet, resulting in:

$$\partial_t c + \left(\mathbf{u}_{/\!/}\cdot\nabla_{/\!/} + u_n\partial_n\right)c = D(\nabla^2_{/\!/} + \partial_n^2)c, \tag{1.92}$$

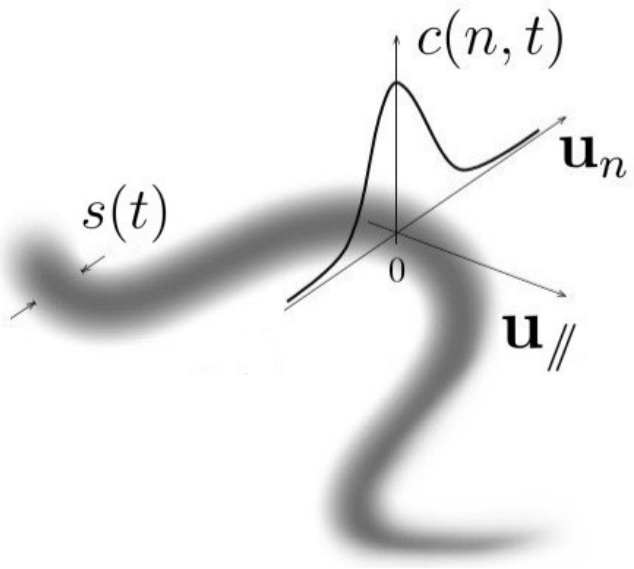


Fig. 1.14 A picturesque illustration of the lamellae (taken from Villermaux (2012)) used to explain the evolution of a concentration field. The figure shows the striation thickness $s(t)$ which evolves according to the local velocities $\mathbf{u}_n$ and $\mathbf{u}_\perp$.

separating the terms tangent to the sheet and in the normal direction to the sheet $\mathbf{n}$.

Mathematically, this separation can be justified by considering the sizes of the two spatial dimensions involved. If we denote the initial volume as $s_0\delta A_0$, the evolution of this portion of the field satisfies the condition $s(t) \ll \sqrt{\delta A(t)}$. By using these characteristic lengths, we can find the asymptotic ratios

$$\mathcal{O}\left(|u_n\partial_n c|/\|\mathbf{u}_{/\!/}\cdot\nabla_\perp c\|\right) = \sqrt{\delta A}/s \tag{1.93}$$

and

$$\mathcal{O}\left(|\partial_n^2 c|/|\nabla_{/\!/}^2 c|\right) = \left(\sqrt{\delta A}/s\right)^2. \tag{1.94}$$

Under our assumptions, these ratios allow us to neglect the parallel terms, leading us to the simplified form

$$\partial_t c + u_n\partial_n c = D\partial_n^2 c. \tag{1.95}$$

Since the frame follows the sheet, we have $u_n = 0$ at the sheet's surface ($n = 0$). To first order, this gives $u_n = -\gamma n$, where $-\gamma(t)$ represents the time-dependent compression rate of the sheet. Consequently, the striation thickness $s(t)$, i.e. the thickness in the absence of diffusion, evolves according to $\dot{s} = -\gamma s$. This compression rate allows us to define the Péclet number

$$Pe = \frac{\gamma s_0^2}{D}, \tag{1.96}$$

which characterizes the relative importance of advection to diffusion in the system.

The Péclet number plays a crucial role in the analysis, as it quantifies the separation between the timescales of diffusion and stirring. This separation allows the previous approximation to be exact in the limit $Pe \to \infty$. In our case, we have a finite Pe, but it is large enough to render the approximation nearly exact. For instance, in water, with an initial thickness $s_0 = 1$ cm and a shear rate $\gamma = 10^{-2}$ s^{-1}, we find $Pe \approx 10^3$, which justifies the validity of this approach.

We can now state a key point central to the thesis's discussion of mixing. As initially noted by Ranz (1979), the equation (1.95) can be transformed into a purely dimensionless diffusion equation using a nonlinear change of variables. Specifically, by defining the scaled coordinate and rescaled time as

$$\xi = \frac{n}{s(t)}, \quad d\tau = \frac{4Ddt}{s(t)^2}, \tag{1.97}$$

we can reformulate the advection-diffusion equation as

$$\partial_\tau c = \frac{1}{4}\partial_\xi^2 c. \tag{1.98}$$

This transformation shows that, under our assumptions, the diffusion principles derived above also apply to mixing when considered in the appropriate rescaled space-time framework. Thus, the evolution of concentration fields under stretching and diffusion can be described similarly to pure diffusion in this dimensionless form. This insight will be central in the analysis and modeling of mixing processes discussed in the thesis.

Once again, this coordinate transformation fully reflects the role of stretching as an enhancer for diffusion efficiency, due to the compression of the filament in the field.

We now discuss the Green's function in these coordinates since we have found that: mixing is fundamentally a 1D diffusion problem. Revisiting the previous calculation, we obtain the solution:

$$c_{\mathrm{G}}(\xi, \tau) = \frac{e^{-\frac{\xi^2}{\tau}}}{\sqrt{\pi\tau}}, \tag{1.99}$$

with a maximal concentration $c_{\max} = \frac{1}{\sqrt{\pi\tau}}$. So if we know the change of coordinate $\tau(t)$, we have the maximal concentration of the sheet. In the general case of advection-diffusion, we no longer have the derived power law in the purely diffusive case. In fact, in this case the decay of the maximum concentration is proportional to $1/\sqrt{\tau}$, which therefore depends on the stirring protocol.

The decay law of the maximal concentration allows us to define the mixing time t_{mix} as the time when the maximal concentration starts the asymptotic decay $1/\sqrt{\tau}$, in other word

$$\tau(t_{\mathrm{mix}}) = \mathcal{O}(1). \tag{1.100}$$

In general, the mixing time is determined by the stirring protocol time scale γ^{-1}, with a correction that depends on the Péclet number, Pe. Formally, we can express it as $t_{\mathrm{mix}} \sim 1/\gamma f(Pe)$, where f is a weak function that depends on the stirring process

(Typically a power law or a logarithm that can be considered a constant in the high Pe regime).

Returning to the initial normal coordinate, the thickness of the diffusive sheet is the Batchelor scale (Batchelor 1959)

$$\eta_{\mathrm{B}} \coloneqq s\Delta\xi = s(t)\sqrt{\tau(t)}. \tag{1.101}$$

This scale remain constant only when the stretching rate is constant. In other cases, it becomes time-dependent also dependent on Pe (see Villermaux 2019). The importance of this length scale lies in the fact that it is the smallest possible scale of field structures before diffusion dominates. From a spectral perspective, this length acts as a cutoff similar to the Kolmogorov scale in turbulence, where scales smaller than η_{B} are smoothed out by diffusion and entirely governed by microscopic dynamics.

Let us now recapitulate what has been described with the case of constant stretching γ. In this case we have that striation thickness follows the law of evolution

$$s(t) = s_0 e^{-\gamma t}. \tag{1.102}$$

The definition of the dimensionless time, defined in equation (1.97), then lead to the expression

$$\tau = \int_0^t \frac{4Ddt'}{s(t')^2} = \frac{2}{Pe}\left(e^{2\gamma t} - 1\right). \tag{1.103}$$

Recalling that we have defined the mixing time t_{mix} as in equation (1.100) in this case becomes

$$t_{\mathrm{mix}} = \frac{1}{2\gamma}\log(Pe/2 + 1) \xrightarrow{Pe\gg 1} \frac{1}{2\gamma}\log(Pe), \tag{1.104}$$

as mentioned above. Furthermore, if we consider that in a given flow there is a distribution of the stretching rate $P(\gamma)$ the above expression allows us to define the distribution of t_{mix} as

$$P(t_{\mathrm{mix}}) = \frac{d\gamma}{dt_{\mathrm{mix}}}P(\gamma) = -\frac{1}{2\gamma^2}\log(Pe)P(\gamma). \tag{1.105}$$

With the expression of τ we can also calculate the Batchelor scale, that from equation (1.101) is

$$\eta_B = s_0 e^{-2\gamma t}\sqrt{\frac{2}{Pe}\left(e^{2\gamma t} - 1\right)} \xrightarrow{t\gg t_{\mathrm{mix}}} \sqrt{\frac{2D}{\gamma}}, \tag{1.106}$$

the only case where this scale is constant and homogeneous over the whole field.

In addition using the conservation of mass the evolution of the maximal concentration can be found to be $c_{\max} \sim e^{-\gamma t}$. Which tells that the variance decays exponentially as well as

$$\langle c\rangle^2 = \langle c_0\rangle^2 e^{-2\gamma t}. \tag{1.107}$$

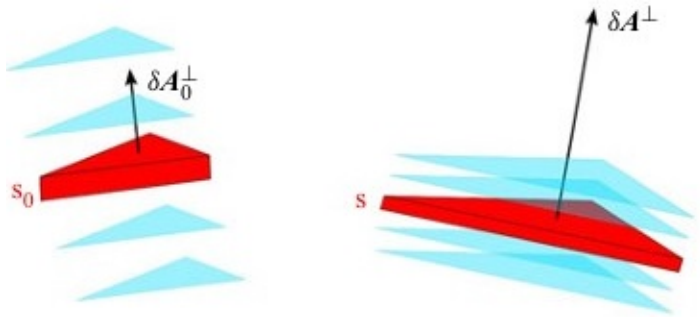


Fig. 1.15 Schematic representation of the evolution of a surface element, the diffuselet (shown in red), where the blue lines represent the iso-values of the scalar, compressed in the direction normal to the diffuselet. Image taken from Meunier & Villermaux (2022).

As we will see in the next section, we can arrive at the definition of "quanta" of the field and statistically describe the evolution of the concentration field as a statistical ensemble of these quanta.

1.3.2 Diffuselet Method

We have addressed in the previous paragraph how the evolution of a passive scalar can be represented as a collection of lamellae in 2D or sheets in 3D. In the following, we will focus on the 3D case and following the work of Meunier & Villermaux (2022), we will explore how to numerically describe the evolution of the field using N small individual elements, called diffuselets, to derive the global statistic of the field.

Each of these diffuselets is considered a Lagrangian tracer, that follows the advection of the external velocity field and experiences local stretching over time. The trajectories of this ensemble coincide with streamlines of the flow velocity $\mathbf{u}$:

$$\begin{cases} \frac{d\mathbf{x}_i}{dt} = \mathbf{u}\left(\mathbf{x}_i, t\right) \\ \mathbf{x}_i(0) = \mathbf{x}_0^i, \end{cases} \tag{1.108}$$

where $\mathbf{x}_0^i$ are the initial positions.

In view of what has been discussed on mixing in general, the Lagrangian tracer are small surface element with and area $\delta A_i(t)$ and a striation thickness $s_i(t)$ (see Figure 1.15). To describe the dynamics of the i-th diffuselet, we define the local $\mathbf{n}^i$, the vector normal to the surface, centered on the position $\mathbf{x}_i$. It can be shown that the surface vector $\delta\mathbf{A}_i = \delta A_i \hat{\mathbf{n}}^i$ evolves according to the stretching dynamics (for an incompressible flow):

$$\begin{cases} \frac{d\delta\mathbf{A}_i}{dt} = -\underline{\underline{\nabla \mathbf{u}}}^T \delta\mathbf{A}_i \\ \delta\mathbf{A}_i(t=0) = \delta\mathbf{A}_0^i \end{cases}, \tag{1.109}$$

where $\underline{\underline{\nabla \mathbf{u}}}^T$ is the transpose of the velocity gradient tensor

$$\underline{\underline{\nabla \mathbf{u}}}^T = \begin{pmatrix} \partial_x u & \partial_x v & \partial_x w \\ \partial_y u & \partial_y v & \partial_y w \\ \partial_z u & \partial_z v & \partial_z w \end{pmatrix}. \tag{1.110}$$

Thanks to the conservation of volume in the evolution of diffuselets $s_i(t)\delta A_i(t) = s_0^i \delta A_0^i$, where s_0^i is the initial striation thickness. The striation thickness is obtained numerically as

$$s_i(t) = \frac{s_0^i \delta A_0^i}{\|\delta \mathbf{A}_i(t)\|}, \tag{1.111}$$

where $\delta \mathbf{A}_i(t)$ is calculated using equation (1.109).

Since $s_i(t)$ is known, it is possible to define the dimensionless time τ_i as in equation (1.97), which after integration gives

$$\tau_i = 1 + \int_0^t \frac{4D}{s_i^2(t')} dt' = 1 + \frac{4D}{(s_0^i)^2} \int_0^t \frac{\|\delta A_i(t)\|^2}{(\delta A_0^i)^2} dt'. \tag{1.112}$$

The initial concentration of the diffuselets is considered Gaussian[2]. From equation (1.99), we can derive the diffusive profile for this small element as follows

$$c_i(n_i) = \frac{1}{\sqrt{\tau_i}} e^{-\frac{n_i^2}{s_i^2 \tau_i}}, \tag{1.113}$$

with a maximal concentration $1/\sqrt{\tau_i}$ and a diffusive thickness $s_i\sqrt{\tau_i}$. This solves numerically the problem of a Lagrangian tracer subjected to diffusion. These quantities depend on the initial orientation of the surface $\delta \mathbf{A}_0^i$.

This model can be extended to simultaneously predict the dynamics of many diffuselets, each with a different initial orientation but all initially located at x_0^i.

The evolution of the surface vector $\delta \mathbf{A}_i$ can be described by the surface dispersion tensor $\boldsymbol{\mathcal{L}}_i$, defined as

$$\begin{cases} \frac{d\boldsymbol{\mathcal{L}}_i}{dt} = -\underline{\underline{\nabla \mathbf{u}}}^T \boldsymbol{\mathcal{L}}_i \\ \boldsymbol{\mathcal{L}}_i(t=0) = \mathbb{1} \end{cases}, \tag{1.114}$$

then the surface vector can then be defined as

$$\delta \mathbf{A}_i(t) = \boldsymbol{\mathcal{L}}_i(t) \delta \mathbf{A}_0^i = \boldsymbol{\mathcal{L}}_i(t) \hat{\mathbf{n}}_0^i \delta A_0^i, \tag{1.115}$$

where $\hat{\mathbf{n}}_0^i$ is the initial orientation normal vector.

[2]We have observed that this is the Green's function of the problem, making diffuselets the de facto equivalent of wavelets for concentration fields. Furthermore, it can be shown (Villermaux 2019) that the Gaussian profile is the asymptotic behavior by the diffusion equation.

Introducing (1.115) into (1.112) yields

$$\tau_i = \mathbb{1} + \frac{4D}{(s_0^i)^2} \int_0^t \left(\boldsymbol{\mathcal{L}}_i(t)\hat{\mathbf{n}}_0^i\right)^T \boldsymbol{\mathcal{L}}_i(t)\hat{\mathbf{n}}_0^i dt'. \tag{1.116}$$

This identity can be rewritten as $\tau_i = (\hat{\mathbf{n}}_0^i)^T \boldsymbol{\mathcal{T}}_i \hat{\mathbf{n}}_0^i$, where the tensor extension of the dimensionless time is defined as:

$$\boldsymbol{\mathcal{T}}_i = \mathbb{1} + \frac{4D}{(s_0^i)^2} \int_0^t \left(\boldsymbol{\mathcal{L}}_i^T \boldsymbol{\mathcal{L}}_i\right)(t')dt'. \tag{1.117}$$

The maximal concentration $1/\sqrt{\tau_i}$ is thus easily obtained for any orientation $\hat{n}_0^i$ once the tensor $\boldsymbol{\mathcal{T}}_i$ is calculated.

To perform ensemble averaging over the initial orientations of the diffuselets, we parameterize the orientations in spherical coordinates relative to the eigenvectors of the tensor $\boldsymbol{\mathcal{T}}_i$ as

$$\hat{\mathbf{n}}_0^i = (\sin\theta\cos\phi, \sin\theta\sin\phi, \cos\theta)\,, \tag{1.118}$$

where θ and ϕ span in the range $[0, \pi/2]$ to avoid over counting in the ensemble.

The advantage of this method lies in its ability to calculate the necessary observables a posteriori using only the eigenvalues of the tensor $\boldsymbol{\mathcal{T}}_i$, denoted as $\eta_i'' \leq \eta_i' \leq \eta_i$.

As demonstrated in Meunier & Villermaux (2022), we can calculate the variance averaged over all initial orientations as

$$\langle c_i^2 \rangle = \frac{\sqrt{2}\delta A_0 s_0}{\sqrt{\pi}} \int_0^{\pi/2} \frac{\sinh^{-1}\left(\sqrt{\eta_i/G_i(\phi) - 1}\right)}{\sqrt{\eta_i - G_i(\phi)}} d\phi, \tag{1.119}$$

where $G_i(\phi) = \eta_i'' \cos^2\phi + \eta_i' \sin^2\phi$. The variance can then also be averaged over all initial positions x_0^i by summing over all the diffuselets

$$\langle c^2 \rangle = \sum_{i=1}^{N} \langle c_i^2 \rangle. \tag{1.120}$$

The PDF of the concentration can be calculated as

$$P(c) = \int_c^1 \frac{\sum_{i=1}^N Q_i(x)}{c\sqrt{\log(x/c)}} dx, \tag{1.121}$$

where

$$Q_i(c) = \frac{\delta A_0^i s_0^i}{\pi c^4} \begin{cases} \frac{1}{\sqrt{\eta_i - \eta_i'}\sqrt{c^{-2} - \eta_i''}} F\left[\frac{2(\eta_i' - c^{-2})(\eta_i - \eta_i'')}{(c^{-2} - \eta_i'')(\eta_i - \eta_i')}\right] & \eta_i'' < c^{-2} < \eta_i' \\ \frac{1}{\sqrt{\eta_i - c^{-2}}\sqrt{\eta_i' - \eta_i''}} F\left[\frac{2(c^{-2} - \eta_i')(\eta_i - \eta_i'')}{(\eta_i - c^{-2})(\eta_i' - \eta_i'')}\right] & \eta_i' < c^{-2} < \eta_i \end{cases}, \tag{1.122}$$

with $F(x) = \sqrt{8/x}K(-2/x)$ (K is the complete elliptic integral of the first kind) that can be approximated by

$$F(x) = \log\left|\left(\frac{4}{x}+1\right)+\sqrt{\left(\frac{4}{x}+1\right)^2-1}\right| - \frac{1.6}{\sqrt{x+1.4}}. \tag{1.123}$$

Also in the case of PDF, the formula written above is the result of averaging over both the initial orientations and initial positions.

1.4 Content of the Manuscript

The objective of this thesis is to study mixing within a soft mixer, aiming to provide essential data for the applications mentioned above. Primarily, this study seeks to enhance the production of fragile cells in bioreactor applications. Additionally, the findings may inform geodynamo studies, with similar methodologies potentially applicable to spheroidal cases.

Chapter 2 focuses on the study of the annular soft mixer, detailing the basic flow and stability by measuring the shear rate up to the turbulent regime. This chapter provides valuable data for bioreactor applications. Experimental studies of mixing were also conducted across a range of parameters.

Chapter 3 describes the implementation of the code used for simulating numerical results with the Diffuselet method. This chapter outlines the validation of the code and its application to a cylindrical soft mixer, as well as an example of its use in homogeneous turbulence.

Following this, Chapter 4 offers an in-depth discussion on the use of experimental data from the flow and mixing of the soft mixer in a cylindrical configuration. The goal is to establish the necessary parameters for the Diffuselet method code to accurately predict the variance trend and PDF evolution across a broad parameter range. These predictions are compared with experimental data, showing strong agreement.

With a slight modification to the configuration, Chapter 5 presents preliminary experimental work on characterizing flow in the soft mixer in a cylindrical setup involving a stratified fluid. Flow stability is measured as the Froude number varies, with instability bands predicted using a simplified theory based on the amplitudes of various modes.

Finally, Chapter 6 concludes with a summary and presents the future directions of this study.

Chapter 2

Resonances and Instabilities in a tilted rotating Annulus

This chapter is dedicated to a theoretical and experimental study of the flow and mixing in the annular configuration of the soft mixer. This is a reproduction of a publication that appeared in the *Journal of Fluid Mechanics* (Scollo *et al.* 2023). I emphasize that the experimental part of this work was done by Clément Nobili.

2.1 Introduction

Large-scale bioreactors used in industry suffer from severe limitations due to slow cell growth (Garcia-Ochoa & Gomez 2009). This problem is due to a lack of good blending, transfer and mixing of the gases and nutrients necessary for cell life. This is why generally, an additional convective stirring is performed by introducing bubbles or using rotating blades. These methods partially solves the problem but also creates a strong shear that inhibits the growth of many cells and can even be lethal for fragile cells (Cherry & Papoutsakis 1986, Doran 1999). Recently, a soft mixer consisting in a tilted rotating cylinder (Meunier 2020) was proposed as a suitable bioreactor for the culture of microalgae. This set-up creates a flow similar to precessing flows, which are known to create an efficient mixing (Goto *et al.* 2014). But the soft mixer is simpler since the forcing of the flow is due to the free surface, which remains flat by gravity. The free surface can also create an efficient mixing in a rotating sphere (Watanabe & Goto 2022). However, the cylindrical and spherical geometries limit the amount of light (necessary for photosynthesis) that can be brought inside the photobioreactor. The use of a cylindrical annulus instead of a cylinder is thus an excellent solution to increase the illumination which can enter through both the inner and the outer cylinders.

From a physical point of view, the soft mixer is a cylinder rotating around its own axis, tilted with respect to the gravity. Thompson (1970) showed that the free surface generates a flow that can be resonant for specific heights of fluids. In fact, this excitation is a particular case of the forcing by a tilted cover rotating at a different velocity than the rotating cylinder, as studied by McEwan (1970). This type of forcing

is very similar to the case of precessing flows, which have been largely studied due to their application to the precession of the Earth (Le Bars *et al.* 2015) and for their abilities to drive a dynamo (Giesecke *et al.* 2018).

In a precessing cylinder, the flow becomes highly energetic and turbulent due to the resonance of global inertial modes, also called Kelvin modes (Kelvin 1880), which are the equivalent of inertial waves in the cylindrical geometry. These modes are resonant when the height of the cylinder is equal to an odd multiple of the half wavelength of the inertial mode (Manasseh 1992, Manasseh 1994). The inertial modes are saturated at low Ekman number by surface Ekman pumping (Gans 1970, Meunier *et al.* 2008) leading to an amplitude scaling as the square root of the Ekman number. The nonlinear saturation is harder to describe analytically because the inviscid nonlinear interaction of the inertial mode with itself does not generate any geostrophic mode (i.e. axisymmetric and axially invariant), as stated by Greenspan (1969). However, the viscous and nonlinear interaction of the inertial mode with itself leads to a spin-down of the fluid which detunes the resonance and creates a nonlinear saturation (Albrecht *et al.* 2021, Gao *et al.* 2021).

The nonlinear interactions can also trigger triadic instabilities (Kerswell 1999), in which the forced inertial mode can couple with two free inertial modes that grow simultaneously (Lagrange *et al.* 2008). The viscous growth rate can be predicted analytically, in excellent agreement with the experimental results (Lagrange *et al.* 2011) and the numerical results (Albrecht *et al.* 2015, Giesecke *et al.* 2015, Albrecht *et al.* 2018 , Lopez & Marques 2018). The transition to a fully turbulent flow depends on the parameters of the precession and is strongly related to the mean axisymmetric flow (Pizzi *et al.* 2021). This transition may even by subcritical with a relaminarization after a probability distribution of lifetime as in pipe flows (Herault *et al.* 2015).

Despite the numerous works on precessing cylinders, there are very few studies on precessing annuli although Lin *et al.* (2014) showed that the global inertial modes and the triadic resonance instabilities are very similar. Recently, Xu & Harlander (2020) studied experimentally the case of a rotating annulus tilted with respect to the gravity. As in the cylinder, they found a resonance of the forced Kelvin mode for specific heights of fluid. The flow then destabilises at low Ekman number thanks to a triadic resonance at small tilt angles and thanks to a shear instability at larger tilt angles.

The goal of this paper is to characterize this flow and its mixing properties. The experimental apparatus to study the flow is described in Section 2.2. Experimental and theoretical characterization of the forced flow and of the instabilities are done in Section 2.3 and 2.4 respectively. Finally we address preliminary results on mixing (Section 2.5) inside this new soft mixer.

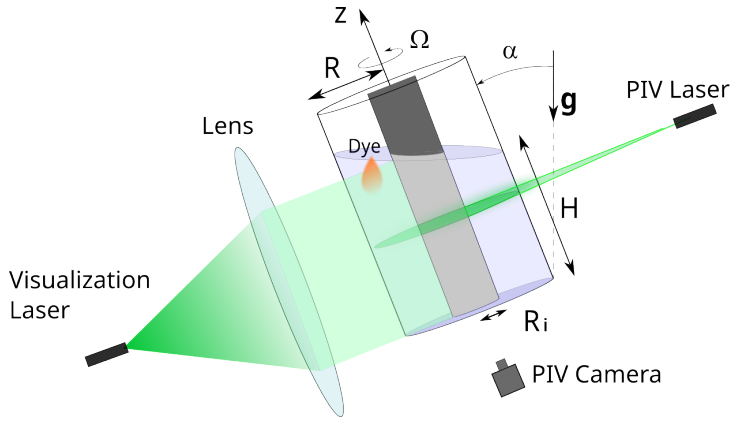


Fig. 2.1 Experimental set-up of a tilted rotating annulus.

2.2 Materials and methods

2.2.1 Experimental set-up

We are interested in studying a mixer formed by an annular cavity (See Figure 2.1), with outer radius $R = 9$ cm and inner radius equal to $R_i = 3$ and 5 cm. The peripheral walls and the bottom are made in polymethylmethacrylate (PMMA) for visualisation. The annulus rotates around its own axis, defined as the z-axis, with angular velocity Ω measured with an accuracy of 0.1 rpm thanks to a DC brushless motor with a reduction of 3.7. The axis of rotation is tilted at an angle α with respect to gravity $\mathbf{g}$, α varying from 0.5° to 10° with an accuracy of 0.1°. In addition, the annulus is filled with water (with kinematic viscosity ν, known within 1% thanks to temperature measurement) at a height H, which is measured before the cylinder is tilted. A blob of dye, characterized by the molecular diffusivity in water κ, is introduced to study the mixing properties of the flow.

2.2.2 Non-dimensional parameters

The system is characterized by 5 non-dimensional parameters:

- **The aspect ratio** $r_i = R_i/R$ is the parameter characterizing the flow geometry. Two different values $r_i = 0.33; 0.56$ are used in the experiments to observe how the flow depends on the confinement.

- **The non-dimensional height** $h = H/R$ is the parameter that can be tuned to select the different resonances of the flow (see Section 2.3). In the experiment, we consider values $0.5 \leq h \leq 2$ to excite four different resonances.

- **The tilting angle** α is the parameter describing the intensity of the forcing applied by the free surface. In the experiment, we consider values $1° \leq \alpha \leq 10°$.

– **The Ekman number**

$$E = \frac{\nu}{\Omega R^2} \tag{2.1}$$

quantifies the ratio of the viscous term over the Coriolis force. In the experiment, it is varied from $E = 10^{-5}$ to $E = 10^{-3}$;

– **The Froude number**

$$Fr = \frac{\Omega^2 R}{g} \tag{2.2}$$

is defined as the square of the ratio of inertial velocity to surface gravity wave speed. This parameter is chosen to be small ($Fr \lesssim 10^{-1}$) to neglect the curvature of the free surface in the theory;

– **The Schmidt number**

$$Sc = \frac{\nu}{\kappa} \tag{2.3}$$

is defined as the ratio of the viscous diffusion rate and molecular diffusion rate. In the experiment, where we used rhodamine B, we have a value of $Sc = 2.3 \times 10^3$ such that the dye streaks are much thinner than the coherent structures of the flow.

2.2.3 Measurement techniques

The flow was characterized using three different methods, particle visualization (Gauthier *et al.* 1998), Laser Induced Fluorescence (LIF) and Particle Image Velocimetry (PIV).

Particle visualizations are made with a vertical laser sheet and introducing flat mica particles (average diameter of 50 µm) in the fluid to qualitatively underline the coherent structures of the flow. This allowed us to observe the presence and the onset time of instabilities.

PIV measurements are obtained using a double pulsed yttrium-aluminium-garnet laser of 150 mJ per pulse at 532 nm with a frequency of 10 Hz and with a time between pulses varying from 0.1 ms to 100 ms. The laser sheet is normal to the axis of the annulus and has a thickness close to 5 mm. It is reflected with two vertical mirrors in order to prevent the shade made by the inner cylinder. The images are acquired by a 4 megapixel camera, positioned below the annulus to decrease the distortion caused by the water, synchronized with the pulsing of the laser. Since the camera is fixed, it does not rotate with the experiment, the images of the second laser pulse are rotated, to remove the solid body rotation and measure the velocity in the annulus frame. The time interval could thus be enlarged in order to increase the accuracy of the velocity field measurements. In the end, vortices of the order of 1% of the solid body rotation can be detected. The images are processed by a cross-correlating algorithm optimized for large velocity gradients (Meunier & Leweke 2003).

Furthermore, using the temporal Fourier transform of the vorticity field filtered by the acquisition frequency, it is possible to measure the frequencies of the observed

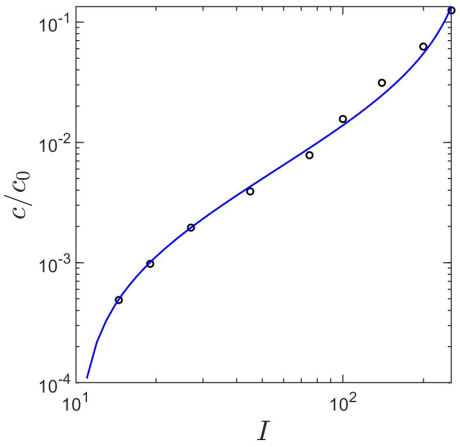


Fig. 2.2 Calibration between the intensity I measured by the camera and the normalized concentration of rhodamine c/c_0.

motions. Finally, the amplitudes of motion are measured by taking the scalar product of the experimental velocity field with the theoretical modes (see Equation (2.56)).

LIF was made by inserting a blob of rhodamine B at the free surface and illuminating with a continuous 532 nm and 100 mW diode to create a laser sheet. The laser sheet is made parallel to the bottom thanks to a large spherical lens with diameter of 20 cm, in order to have a uniform intensity in the annulus. The intensity I recorded by the camera is calibrated for each experiment as a function of the concentration by placing inside the annulus test tubes of rhodamine at a known concentration. The data are fitted, with an accuracy of 10%, by the empirical law (see Figure 2.2)

$$\frac{c(I)}{c_0} = \Gamma \frac{I - I_0}{1 - I/I_{\text{sat}}}, \tag{2.4}$$

where I_0 and I_{sat} are the intensity of background and saturation of dye respectively with the empirical parameter Γ.

2.3 Forced mode

Using R and Ω^{-1} as length and time scale, we define the non-dimensional variables $r = r^*/R$, $t = \Omega t^*$ and $z = z^*/R$ from the dimensional variables (r^*, z^*, t^*). We use cylindrical coordinates for the position (r, θ, z) and for the velocity $\mathbf{u} = (u, v, w)$.

For small Froude number (defined in Equation (2.2)), the free surface is horizontal and motionless in the laboratory frame. In the reference frame rotating with the annulus, it is thus located at a height

$$\zeta(r, \theta) = h - \alpha r \cos(\theta + t). \tag{2.5}$$

This position oscillates at a non-dimensional frequency $\varpi = 1$ because the free surface rotates at angular velocity $-\Omega$ (in dimensional unit) in the rotating frame. The normal velocity $w = d\zeta/dt$ of the free surface generates a forcing excitation with azimuthal wavenumber $m = 1$:

$$w(z = \zeta) = \alpha r \sin(\theta + t). \tag{2.6}$$

The flow is made by a constructive interference of inertial waves which lead to global Kelvin modes (Kelvin 1880), as shown by Thompson (1970) for a cylinder and by Xu & Harlander (2020) for an annulus. The annular modes can be derived by considering the linearized Navier-Stokes equations in the frame of the annulus

$$\begin{cases} \partial_t \mathbf{u} + 2\hat{\mathbf{z}} \wedge \mathbf{u} = -\nabla p + E\nabla^2 \mathbf{u} \\ \nabla \cdot \mathbf{u} = 0 \end{cases}, \tag{2.7}$$

where we have introduced the reduced pressure $p = P - \rho g z + \rho r^2 \Omega^2/2$.

This equation is solved in the limit of $E \to 0$ by deriving the equation for pressure. The easiest way to derive it is to take the divergence and curl of the equation, with the incompressibility condition and assuming that $(\mathbf{u}, p) \to (\mathbf{u}, p)e^{i\varpi t}$, which combined give the Poincaré equation (Greenspan 1968)

$$\nabla^2 p(r, \theta, z) - \frac{4}{\varpi^2} \partial_z^2 p(r, \theta, z) = 0. \tag{2.8}$$

By decomposing the pressure in Fourier mode in z and θ is it possible to show that the previous equation becomes the Bessel equation

$$\frac{d^2}{dr^2} p(r) + \frac{1}{r} \frac{d}{dr} p(r) + \left[k^2 \left(\frac{4}{\varpi^2} - 1 \right) - \frac{m^2}{r^2} \right] p(r) = 0, \tag{2.9}$$

where m and is the azimuthal wavenumber and k is the axial wavenumber.

The general solution with $m = 1$ and frequency $\varpi = 1$ is given by (see Lin *et al.* 2014)

$$\mathbf{u} = \sum_{j=1}^{\infty} \mathrm{Re}\left[A_j \begin{pmatrix} u_j(r)\cos(k_j z) \\ v_j(r)\cos(k_j z) \\ w_j(r)\sin(k_j z) \end{pmatrix} e^{i(\theta+t)} \right] \quad , \quad p = \sum_{j=1}^{\infty} \mathrm{Re}\Big[A_j p_j(r)\cos(k_j z) e^{i(\theta+t)} \Big], \tag{2.10}$$

with

$$\begin{cases} p_j(r) = c_j^J J_1(\sqrt{3}k_j r) + c_j^Y Y_1(\sqrt{3}k_j r) \\ u_j(r) = -\dfrac{i}{3}\Big(\partial_r p_j + \dfrac{2}{r}p_j\Big) \\ \qquad = -\dfrac{i}{3r}\left[c_j^J\left(J_1(\sqrt{3}k_j r) + \sqrt{3}k_j J_0(\sqrt{3}k_j r)\right) + c_j^Y\left(Y_1(\sqrt{3}k_j r) + \sqrt{3}k_j Y_0(\sqrt{3}k_j r)\right)\right] \\ v_j(r) = \dfrac{1}{3}\Big(2\partial_r p_j + \dfrac{1}{r}p_j\Big) \\ \qquad = -\dfrac{1}{3r}\left[c_j^J\left(J_1(\sqrt{3}k_j r) + 2\sqrt{3}k_j r J_0(\sqrt{3}k_j r)\right) + c_j^Y\left(Y_1(\sqrt{3}k_j r) + 2\sqrt{3}k_j r Y_0(\sqrt{3}k_j r)\right)\right] \\ w_j(r) = -ik_j p_j = -ik_j\left(c_j^J J_1(\sqrt{3}k_j r) + c_j^Y Y_1(\sqrt{3}k_j r)\right) \end{cases}, \tag{2.11}$$

where J and Y are the Bessel function of the first and second kind and Re means real part.

The ratio c_j^J/c_j^Y of coefficients of the real solution is found from the boundary condition at $r = 1$

$$u(r = 1) = 0, \quad \forall\theta, z. \tag{2.12}$$

We choose (although this is valid within a multiplicative constant)

$$c_j^J = Y_1(\sqrt{3}k_j) + k_j\sqrt{3}Y_0(\sqrt{3}k_j) \quad , \quad c_j^Y = -\Big[J_1(\sqrt{3}k_j) + k_j\sqrt{3}J_0(\sqrt{3}k_j)\Big]. \tag{2.13}$$

In general, the slip boundary condition at $r = r_i$

$$u(r = r_i) = 0, \quad \forall\theta, z, \tag{2.14}$$

gives the dispersion relation between the axial wavenumber k and the frequency of the modes ϖ. In our case, the forcing frequency is equal to $\varpi = 1$, which fixes discrete values of the axial wavenumber k_j thanks to the dispersion relation

$$c_j^J\left[J_1(\sqrt{3}k_j r_i) + \frac{k_j\sqrt{3}}{r_i}J_0(\sqrt{3}k_j r_i)\right] + c_j^Y\left[Y_1(\sqrt{3}k_j r_i) + \frac{k_j\sqrt{3}}{r_i}Y_0(\sqrt{3}k_j r_i)\right] = 0. \tag{2.15}$$

Numerical values for $r_i = 0.333$ and $r_i = 0.556$ are given in Table 2.1.

The structure of the first Kelvin mode is shown in Figure 2.3. It exhibits a global flow toward negative x in the upper part of the cylinder (see Figure 2.3 (a)) and a global flow toward positive x in the lower part of the cylinder (see Figure 2.3 (a)). This is due to the choice of the height $h = 1.306$ corresponding to half a wavelength of this Kelvin mode. This creates a meridional recirculation observed in Figure 2.3 (b).

The vorticity of the Kelvin mode can be calculated using the Kelvin modes property $\boldsymbol{\omega} = -2i\partial_z\mathbf{u}$,

(a)

j	1	2	3	4
k_j	2.406	5.245	8.024	10.776
h_j	1.306	0.599	0.392	0.292

(b)

j	1	2	3	4
k_j	3.928	8.089	12.200	16.299
h_j	0.800	0.388	0.258	0.193

Table 2.1 Numerical values of the first 4 resonance wave-numbers and height of the j-th Kelvin mode given by the dispersion relation in Equation (2.15), for $r_i = 0.333$ (a) and $r_i = 0.556$ (b).

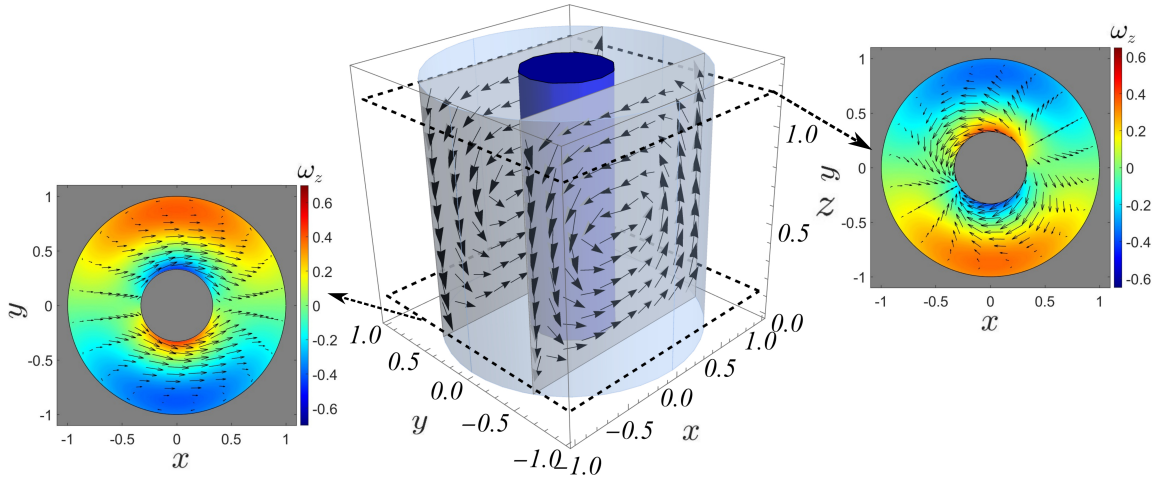


Fig. 2.3 Structure of the first Kelvin mode (2.10) with azimuthal wavenumber $m = 1$. (b) Visualisation of the velocity field in two sections parallel to the z-axis showing the meridional recirculation. Two sections normal to the z-axis are shown for $z = 0.13 \equiv z_{\text{laser}}$ in (a) and for $z = 1.18 \equiv h_1 - z_{\text{laser}}$ in (c). The amplitude A_1 is given by the viscous theory (2.21) for $r_i = 0.333$, $E = 4.1 \times 10^{-4}$, $h = 1.31$ and $\alpha = 3°$.

$$\omega_z = \sum_{j=1}^{\infty} \text{Re}\Big[-2k_j^2 A_j p_j(r) \cos(k_j z) e^{i(\theta+t)} \Big]. \tag{2.16}$$

Near the free surface, the global flow creates an outer lobe of negative vorticity for y positive and an outer lobe of positive vorticity for y negative. The axial antisymmetry is simply due to the azimuthal wavenumber $m = 1$. Additional small lobes of vorticity with opposite sign are located close to the inner cylinder.

The amplitude of the modes must be set in order to fulfill the boundary condition at the free surface (2.6). This boundary condition is also valid at $z = h$ rather than at

$z = \zeta$ at first order in α. Multiplying by $r\bar{\mathbf{u}}$ and integrating on r gives[1]

$$A_j = \frac{\alpha F}{T \sin(k_j h)}, \tag{2.17}$$

with

$$F = \int_{r_i}^{1} r^2 \Big[c_j^J J_1(\sqrt{3} k_j r) + c_j^Y Y_1(\sqrt{3} k_j r) \Big] dr, \tag{2.18}$$

and

$$T = k_j \int_{r_i}^{1} r \Big[c_j^J J_1(\sqrt{3} k_j r) + c_j^Y Y_1(\sqrt{3} k_j r) \Big]^2 dr. \tag{2.19}$$

It is interesting to note that the term F can be integrated analytically as given in (2.51). Numerical values of T and F are given in Table 2.2. This theory is similar to the one given in Xu & Harlander (2020) except that we give analytical predictions of the amplitudes whereas they calculated the amplitudes numerically by fitting the theoretical solution with five modes to the top boundary condition (2.6).

From this expression it is clear that the amplitude diverges when $\sin(k_j h) = 0$, i.e. for $k_j = n\pi/h$. It means that the jth Kelvin mode is resonant when the height of fluid h is an integer multiple of the half-wavelength (see Table 2.1), i.e. when $h = n h_j$ with

$$h_j = \pi / k_j. \tag{2.20}$$

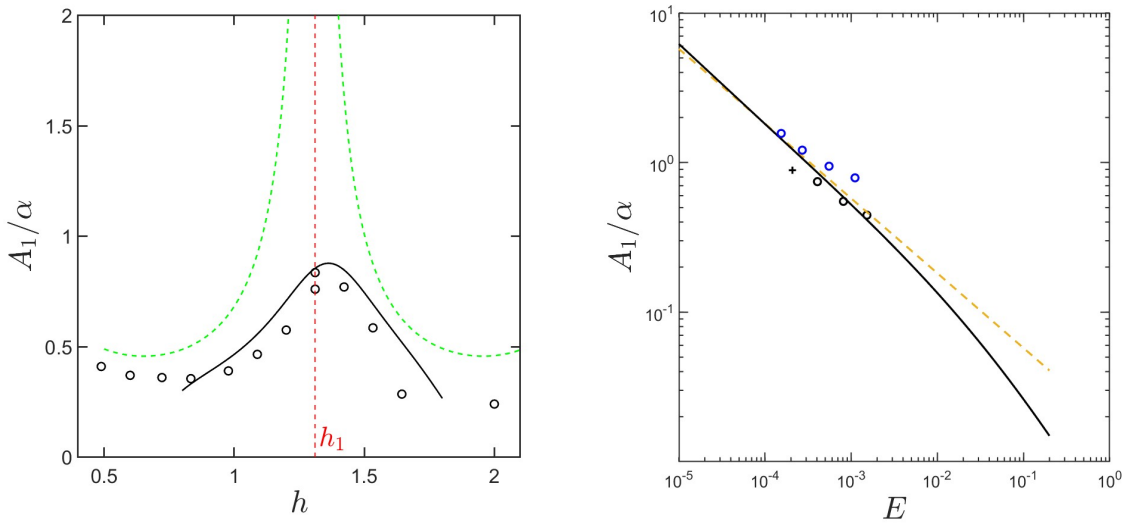
In that case, the axial velocity of the mode vanishes at $z = h$ and is thus unable to contribute to fulfill the boundary condition (2.6) unless its amplitude is infinite. This is similar to the resonance of a string excited by an oscillation of its end when the end is located at the node of a mode.

This inviscid prediction is plotted in Figure 2.4 (a) as a green dashed line. It clearly exhibits a divergence at $h = h_1$. Outside the resonance (for $h < 0.8$), the theoretical value is close (within 20%) but slightly larger than the experimental value. Here, the experimental value is measured by projecting the total velocity field at $z_{\text{laser}} = 0.13$ onto the inviscid Kelvin mode (see for further details Meunier *et al.* 2008).

Obviously, the experimental amplitude does not diverge at the resonance because of viscous and non-linear effects. As a first step, we have calculated the saturation due to the Ekman pumping and volumetric damping. It can be accounted for analytically by doing an analysis similar to the case of a cylinder (Gans 1970, Meunier *et al.* 2008, Meunier 2020). As shown in appendix 2.7.1, the Ekman pumping $\tilde{\mathbf{u}}$ has a simple expression as a function of the z-derivative and the normal derivative of the normal velocity (2.35). The amplitude is then found by a solvability condition including the Ekman pumping at the bottom, the inner and the outer cylinders (see Appendix 2.7.1). It leads to an analytic expression for the amplitude

$$A_j = \frac{\alpha F}{T \sin(k_j h) + \sqrt{E}\Big(B + C_e + C_i\Big) + EV}, \tag{2.21}$$

[1]To find the amplitude we use the orthogonality rules $\int_{r_i}^{1} w_i(r) w_j(r) r dr \propto \delta_{ij}$.



(a) (b)

Fig. 2.4 Amplitude of the first mode of the first resonance A_1/α for $r_i = 0.333$. It is plotted as a function of h for $E = 4.1 \times 10^{-4}$ (a) and as a function of E for $h = h_1$ (b). Experimental measurements are obtained at $\alpha = 3°$ (black symbols) and at $\alpha = 1°$ (blue symbols). Experimental data are represented by $\circ$ for stable experiments, $+$ for unstable experiment. The dashed green line corresponds to the inviscid theory (2.17) and the black solid line corresponds to the viscous theory (2.21). In (b) the dashed orange line is the viscous amplitude neglecting the volumic term (i.e. with $V = 0$).

	$r_i = 0.33$	$r_i = 0.56$
F	$-i0.493\cos(2.406h)$	$-i0.222\cos(3.928h)$
T	$i1.080\cos(2.406h)$	$i1.117\cos(3.928h)$
B	$-3.286 + i2.225$	$-5.546 + i3.756$
C_e	$-6.110(1+i)\Big[h/2 + 0.104\sin(4.811h)\Big]$	$-14.788(1+i)\Big[h/2 + 0.064\sin(7.855h)\Big]$
C_i	$-21.965(1+i)\Big[h/2 + 0.104\sin(4.811h)\Big]$	$-27.776(1+i)\Big[h/2 + 0.064\sin(7.855h)\Big]$
V	$-86.551h - 5.490\sin(4.811h)$	$-377.867h - 13.660\sin(7.855h)$

Table 2.2 Numerical values of the viscous correction terms, for $r_i = 0.33$ and $r_i = 0.56$ as a function of h.

where F is the forcing term, $(B + C_e + C_i)$ describe the surface Ekman pumping term (bottom, external and internal cylinder) and V is the volumetric term (see Table 2.2 for reference values).

This theoretical amplitude is shown in Figure 2.4 (a) as a black solid line. It is in excellent agreement with the experiment around the resonance, with no fitting parameter. It should be noted that viscous corrections lead to a small shift of the maximum amplitude to $h = 1.1h_1$ due to the imaginary part of $B + C_e + C_i$.

When varying the Ekman number (Figure 2.4 (b)), the scaling of the amplitudes change from $A_1 \propto E^{-1/2}$, at small E where the surface term is dominant, to $A_1 \propto E^{-1}$ when the volumetric term becomes dominant. There is again a good agreement between the experimental and numerical values.

Finally, we would like to note the fact that the free surface in the experiment cannot be considered completely clean and that the presence of contaminants changes the boundary condition on the free surface. However, it should be noted that in the extreme case of no-slip boundary (where a liquid surface covered by a rigid layer of non-mobile surfactants) the amplitude of the flow is altered by a maximum of 15% in absolute value. We have therefore, consciously, not accounted for surface contamination in the present analysis of the flow, but do acknowledge that it may need to be in other particular cases.

Figure 2.5 shows a comparison of the velocity and vorticity fields obtained experimentally and numerically (using a finite element code). They exhibit the same structures and amplitudes, with a mean flow toward positive x. This is in fair agreement with the theoretical prediction of Figure 2.3 (c) despite a larger vorticity by a factor 2. The main difference with theory is due to the presence of the Ekman layer.

To conclude, we have given an analytic solution for the forced mode with no fitting parameter, in good agreement with the observation in experimental and numerical results.

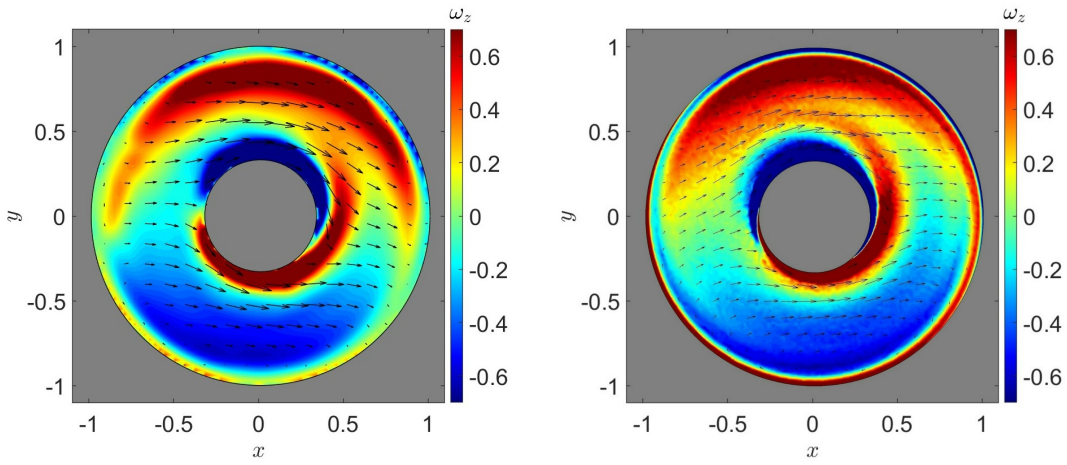


Fig. 2.5 Axial vorticity ω_z and velocity field at $z = 0.13$ for $\alpha = 3°$, $E = 4.1 \times 10^{-4}$ and $r_i = 0.33$. The experimental PIV measurement (a) is compared to a Direct Numerical Simulation (DNS) obtained with the finite element code Comsol (b).

2.4 Instabilities of the flow

As in a tilted cylinder and in precessing containers, the flow becomes unstable when E decreases. This can be addressed experimentally by using PIV and visualizations.

2.4.1 Onset time of the instability

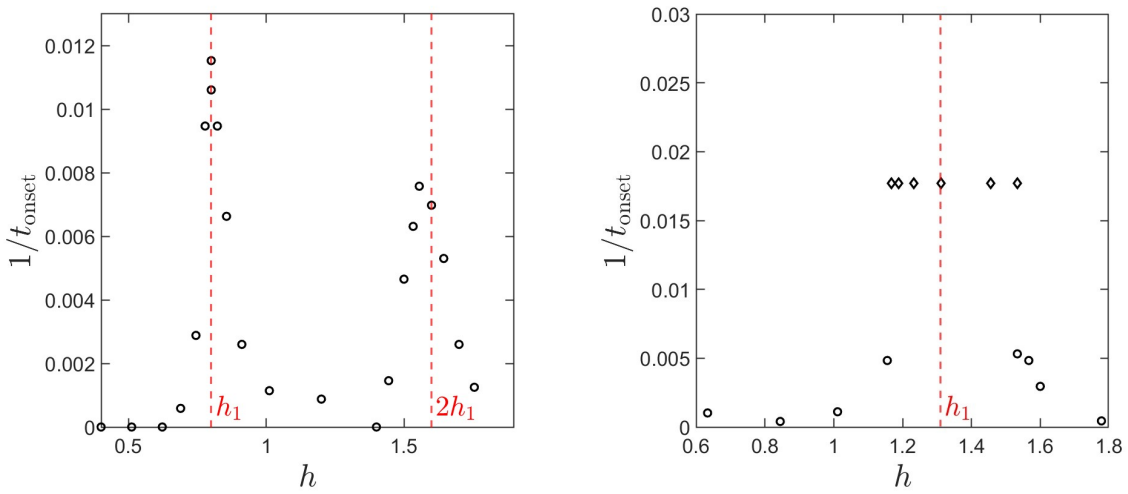
The experimental protocol consisted in getting the solid body rotation without tilt, and then tilting smoothly the annulus within a few seconds. Particle visualisations exhibited periodic coherent structures appearing in the laser sheet after a time depending on the height of fluid and on the Ekman number. This onset time t_{onset} is plotted as a function of h in Figure 2.6 for the two aspect ratios $r_i = 0.33$ and $r_i = 0.56$. The Ekman number E was chosen small enough for an instability to appear.

Because the instabilities are triggered from the amplitudes A_j of the forced mode, the instability occurs faster when the height of water is near the resonant heights h_j. Indeed, experiments at $r_i = 0.56$ show that t_{onset} reaches its minimum value at the first and second resonances of the first Kelvin mode. In between these two resonances, the onset time is 10 times larger. For $r_i = 0.33$, the flow is strongly unstable, but the onset time saturates at $1/0.017$ which correspond to the time needed for the forced mode to grow.

In the following we will focus only on the resonant heights.

2.4.2 Triadic instability

Figure 2.7 shows the experimental vorticity fields of the instability at mid-height and at a quarter of height for $r_i = 0.33$ and $h = h_1$. The vorticity fields have been extracted



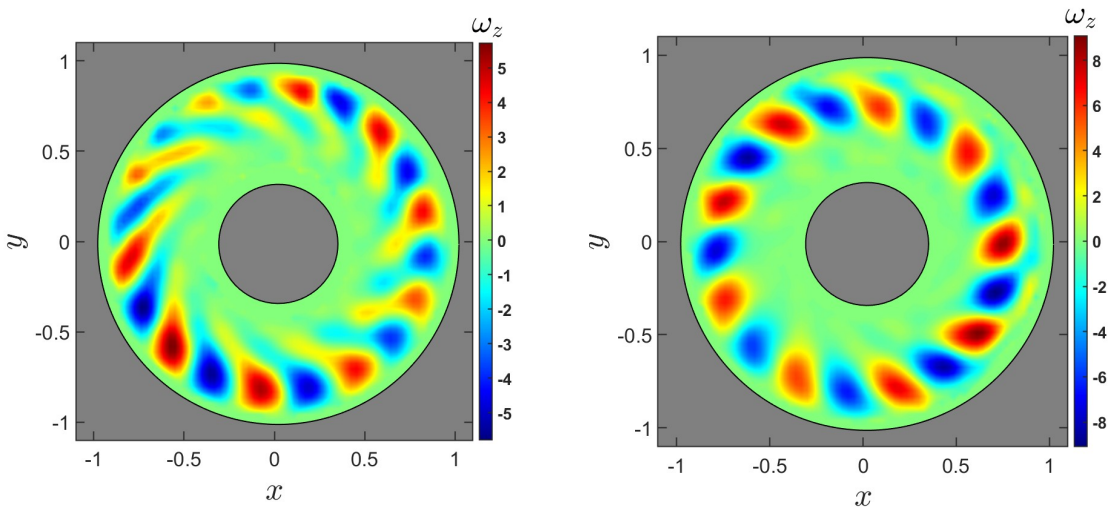
(a) (b)

Fig. 2.6 Inverse of the onset time t_{onset} as a function of the height h for $E = 3.6 \times 10^{-5}$, $\alpha = 3°$ and $r_i = 0.56$ (a) and $r_i = 0.33$ (b). Red dashed lines represent the theoretical values of the resonances, while experimental data are indicated by ○ for a triadic instability and ◇ for a centrifugal instability.

from the mean forced mode by calculating the temporal Fourier component at the frequency -9.58 in the laboratory frame of reference. The instability exhibits a ring of alternate vortices with an azimuthal wavenumber $m' = 9$ at a quarter of height and an azimuthal wavenumber $m'' = 10$ at mid-height. Although these PIV measurements have been done separately, the difference in azimuthal wavenumber is not due to randomness since it always gives the same result. Xu & Harlander (2020) have actually shown that the two modes are present at the same time. However, the Kelvin modes have an axial vorticity proportional to $\cos(kz)$ (such that $w \sim \sin(kz)$ vanishes at $z = 0$). If the first mode has an axial wavenumber $k' = \pi/h_1$, it will not be visible at mid-height. Similarly, if the second mode has an axial wavenumber $k'' = 2\pi/h_1$ it will not be visible at a quarter of height. This explains the simultaneous presence of the two modes and their separate measurements in two well chosen sections.

Theoretically, the first Kelvin modes with $(m', k') = (9, \pi/h_1)$ and $(m'', k'') = (10, 2\pi/h_1)$ have frequencies $\varpi' = -0.348$ and $\varpi'' = 0.649$ which give almost the same frequency (equal to -9.348 and -9.351) in the laboratory frame of reference (obtained by adding $-m'\Omega$ or $-m''\Omega$ with $\Omega = 1$ from dimensionalisation), very close to the experimental frequency -9.58. To conclude, the modes seem to respect the following conditions

$$k'' - k' = k_1, \tag{2.22}$$



(a) (b)

Fig. 2.7 Vorticity field at the resonance, filtered at the frequency -9.58 in the laboratory frame of reference and averaged over one rotation. For $E = 10^{-4}$, $r_i = 0.33$, $\alpha = 1°$ and two different positions of the laser sheet: $h_{\text{laser}} = 0.25$ (a) and $h_{\text{laser}} = 0.5$ (b). The position of the laser sheet is chosen in order to separate the two free modes (respectively at the nodes of m' and m'' mode) thus revealing the azimuthal wavenumbers $m' = 9$ (a) and $m'' = 10$ (b).

where $k_1 = \pi/h_1$ is the axial wavenumber of the forced resonant mode;

$$m'' - m' = m, \tag{2.23}$$

where $m = 1$ is the azimuthal wavenumber of the forced resonant mode;

$$\varpi'' - \varpi' = \varpi, \tag{2.24}$$

where $\varpi = 1$ is the frequency of the forced resonant mode. This is fulfilled theoretically only for modes $m' = 9$ and $m'' = 10$. These conditions are exactly similar to the case of precessing cylinders (Lagrange *et al.* 2011, Albrecht *et al.* 2015) and of tilted cylinders (Meunier 2020) where modes of azimuthal wavenumbers $m' = 5$ and $m'' = 6$ were observed. The higher azimuthal wavenumbers in the annulus probably come from the radial confinement. Moreover, it should be noted that theoretically these conclusions can also be drawn with arguments of symmetry of the problem (Marques & Lopez 2015).

These conditions indicate that a triadic resonance between the three modes is possible : the forced mode may feed simultaneously the two free modes by non-linear interactions, leading to a triadic resonance instability (TRI). Although the theory has been done for a precessing cylinder (Lagrange *et al.* 2011) and for a tilted cylinder (Meunier 2020), it has never been done for an annulus despite experimental evidences for

a precessing annulus (Lin *et al.* 2014) and a tilted annulus (Xu & Harlander 2020). We derive here the linear stability analysis for the annulus. Assuming that the amplitudes A' and A'' of the two modes have a temporal variation of the first order (proportional to $A_1 \propto \alpha/\sqrt{E}$) and considering only the first order terms in these amplitudes, it is possible to derive the amplitude equations (see Appendix 2.7.2)

$$\begin{cases} \partial_t A' = N' \bar{A}_1 A'' - D' A' \\ \partial_t A'' = N'' A_1 A' - D'' A'' \end{cases}, \tag{2.25}$$

where N' and N'', defined in Appendix 2.7.2 are analytic coefficients describing the non-linear interaction of the forced mode and the free one's, and $\bar{A}_1$ is the complex conjugate of the amplitude A_1 defined in (2.21). They are given by integrals in Appendix 2.7.2 which can be calculated analytically in the case of a small gap using an asymptotic expansion (see Appendix 2.7.3).

The parameters

$$D' = \sqrt{E}s' + Ev' + i\Delta k' q', \quad D'' = \sqrt{E}s'' + Ev'' + i\Delta k'' q'', \tag{2.26}$$

are also analytical (see Appendix 2.7.2 for definition of the coefficients and numerical values). The first two terms describe the viscous corrections, with s for the Ekman damping on the edges and v for the volumetric damping. The last term is the detuning effect, due to the fact that the free modes are not exactly resonant with the forced mode.

The set of equations is exactly similar to Equations (4.13 a,b) in Lagrange *et al.* (2011) and can be easily integrated with an exponential solution of the type $A', A'' \propto e^{\sigma t}$ leading to a growth rate σ satisfying

$$\left(\sigma + D'\right)\left(\sigma + D''\right) = \left|A_1\right|^2 N' N''. \tag{2.27}$$

The flow is stable if $\mathrm{Re}(\sigma) < 0$ which leads to the threshold tilt angle (in degrees) as:

$$\alpha(E) = \frac{180}{\pi} \frac{1}{\left|A_1/\alpha\right|\sqrt{N'N''}} \sqrt{D'_{\mathrm{Re}} D''_{\mathrm{Re}} \left(1 + \frac{\left(D'_{\mathrm{Im}} - D''_{\mathrm{Im}}\right)^2}{\left(D'_{\mathrm{Re}} + D''_{\mathrm{Re}}\right)^2}\right)}, \tag{2.28}$$

where D_{Re} and D_{Im} are real and imaginary part of the viscous correction.

This stability curve is plotted in Figure 2.8-2.9 for the two different aspect ratios. It is in excellent agreement with the experimental data for $r_i = 0.333$ with an accuracy of about 10%. It should be noted that there are no fitting parameters in this viscous theory since all coefficients can be computed analytically. The agreement is not as good for $r_i = 0.56$ but still correct with an error smaller than 30%. The effect of the detuning is very small for $r_i = 0.56$ and invisible for $r_i = 0.33$.

The scaling of the threshold curves can be explained asymptotically. First, we consider only the surface damping of the forced Kelvin mode (which is valid for

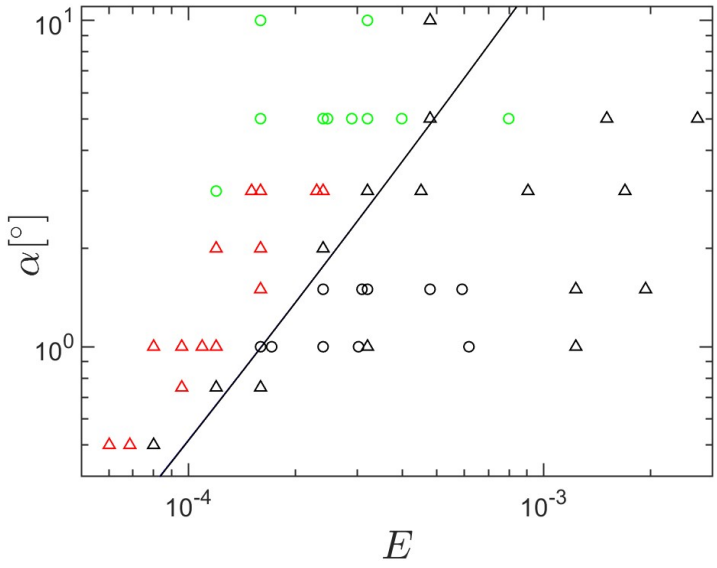


Fig. 2.8 Stability diagram in the parameter space α and E, for $r_i = 0.33$ and $h = h_1$. Color symbols represent unstable experiments (red for triadic instability and green for centrifugal instability) and black symbols represent stable experiments. The experiments are visualised using PIV △ and Particle visualisations ○. The black solid line corresponds to the theoretical threshold of Eq.(2.28) with coefficients given in Table 2.3 for the most unstable modes $(m', m'') = (9, 10)$

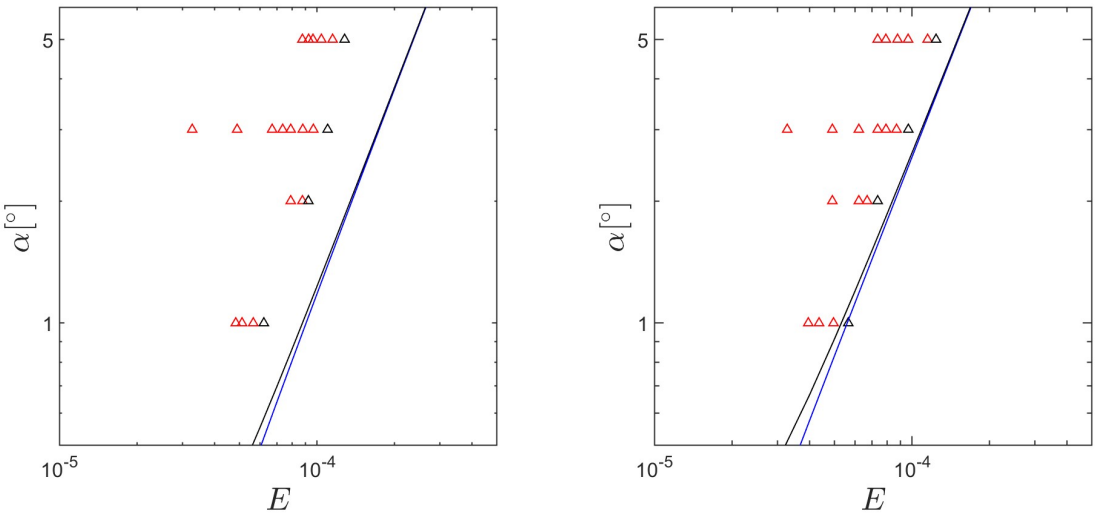


Fig. 2.9 Stability diagram in the parameter space α and E, for $r_i = 0.55$ and $h = h_1$ (a) and $h = 2h_1$ (b). Red symbols represent unstable experiments and black symbols represent stable experiments. The theoretical triadic resonance critical curves of Equation (2.28) with the coefficients given in Table 2.3 are shown in black with detuning and in blue without detuning for the most unstable modes $(m', m'') = (17, 18)$.

$E \lesssim 10^{-3}$, see Figure 2.4 (b)). It leads to a scaling of the forcing amplitude as $A_1 \sim F/\sqrt{E}S$ (where $S = (B + C_e + C_i)$). Then, Equation (2.28) has 3 different scalings depending whether the detuning, the surface damping of the free modes or the volumic damping of the free modes is dominant (see also Lagrange *et al.* 2011):

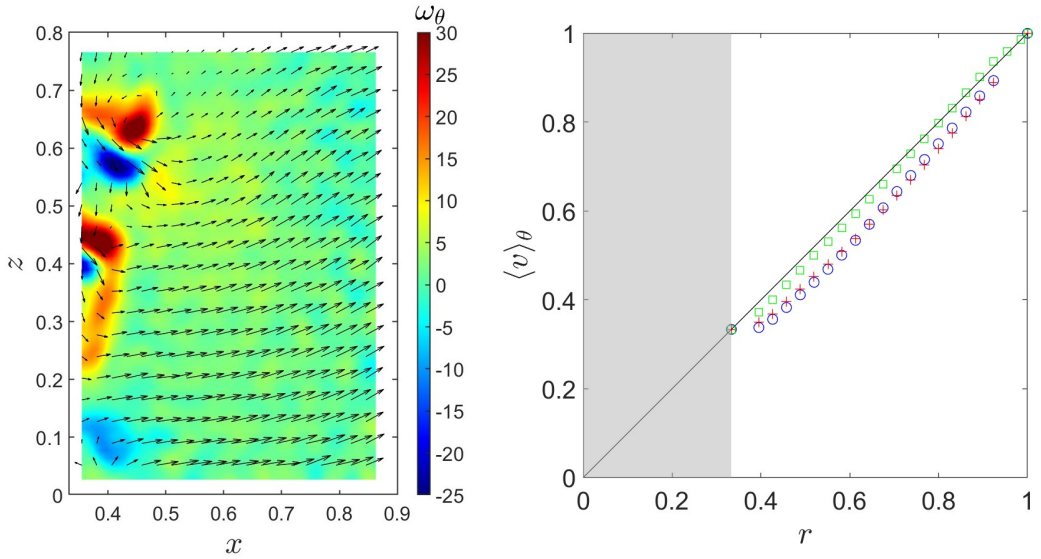
$$\alpha(E) \sim \begin{cases} E^{1/2}\left|\frac{S}{F}\right|\sqrt{\frac{|\Delta k' q' \Delta k'' q''|}{N'N''}}, & \text{for } E \lesssim E_c^{(1)} \\ E\left|\frac{S}{F}\right|\sqrt{\frac{s'_{\mathrm{Re}} s''_{\mathrm{Re}}}{N'N''}\left[1+\left(\frac{s'_{\mathrm{Im}}-s''_{\mathrm{Im}}}{s'_{\mathrm{Re}}+s''_{\mathrm{Re}}}\right)^2\right]}, & \text{for } E_c^{(1)} \lesssim E \lesssim E_c^{(2)}, \\ E^{3/2}\left|\frac{S}{F}\right|\sqrt{\frac{v'v''}{N'N''}}, & \text{for } E \gtrsim E_c^{(2)} \end{cases} \tag{2.29}$$

where $E_c^{(i)}$ are the critical values given by the formulas

$$E_c^{(1)} = \left|\frac{|\Delta k' q' \Delta k'' q''|}{s'_{\mathrm{Re}} s''_{\mathrm{Re}}}\left[1+\left(\frac{s'_{\mathrm{Im}}-s''_{\mathrm{Im}}}{s'_{\mathrm{Re}}+s''_{\mathrm{Re}}}\right)^2\right]^{-1}\right|, \tag{2.30}$$

$$E_c^{(2)} = \left|\frac{s'_{\mathrm{Re}} s''_{\mathrm{Re}}}{v'v''}\left[1+\left(\frac{s'_{\mathrm{Im}}-s''_{\mathrm{Im}}}{s'_{\mathrm{Re}}+s''_{\mathrm{Re}}}\right)^2\right]\right|. \tag{2.31}$$

In the experiments, the Ekman number is always close to $E_c^{(2)}$ such that the scaling exponent is between 1 and 3/2.



(a) (b)

Fig. 2.10 (a) Instantaneous PIV measurements of the meridional velocity and the toroidal vorticity for $E = 3.6 \times 10^{-4}$ during the onset of the instability. (b) Azimuthally averaged tangential velocity in the frame of reference of the laboratory at $\alpha = 5°$, $h = h_1 = 1.31$, $r_i = 0.33$ and $z = 0.33$ for $E = 7.3 \times 10^{-4}$ in green, $E = 3.6 \times 10^{-4}$ in red and $E = 2.2 \times 10^{-4}$ in blue. The black line corresponds to the solid body rotation of the annulus.

2.4.3 Centrifugal instability

For large tilt angles the flow exhibited an instability different to the triadic resonance instability studied above. For $r_i = 0.33$, this instability was found at tilt angles larger than 3 degrees, as shown by the green symbols of Figure 2.8. In this case, the particle visualizations and the PIV measurements highlighted the presence of small toroidal vortices of alternate sign close to the inner cylinder (see Figure 2.10 (a)). This structure is reminiscent of a centrifugal instability (Rayleigh 1917, Taylor 1923) occurring in Taylor-Couette flows.

For an axisymmetric flow, it is well known that the centrifugal instability occurs when the Rayleigh discriminant becomes negative

$$\frac{d}{dr}\left(r^2 v_\theta^2\right) < 0. \tag{2.32}$$

In our case, the forced mode is not exactly axisymmetric, but we can use the azimuthal average of the velocity $\langle v \rangle_\theta$ to define a Rayleigh discriminant. In the limit of vanishing tilt angles, the solid body azimuthal profile is equal to r. This prediction is plotted as a black line in Figure 2.10 (b). For large Ekman number (i.e. when the resonant Kelvin mode is strongly damped), the experimental value is close to this prediction. However, when the Ekman number decreases, the experimental value decreases because the resonant Kelvin mode decelerates the solid body rotation by

self non-linear interaction (Albrecht *et al.* 2021, Gao *et al.* 2021). The value of v_θ is thus a decreasing function of r close to the inner cylinder (between $r = 0.33$ and $r = 0.4$) leading to a negative Rayleigh discriminant. We can thus expect a centrifugal instability close to the inner cylinder, which is consistent with the alternate toroidal vortices observed in the PIV measurements. It should be noted that the value of v_θ was not measured by PIV on the inner cylinder but it must be equal to r_i for a no-slip boundary condition.

2.4.4 Turbulent flow regime

When the Ekman number E is decreased further below the threshold, the flow becomes more and more turbulent. As found for a cylinder (Lopez & Marques 2016), the amplitude of the free modes first become time dependent. Then other azimuthal Fourier modes appear. It leads to smaller structures that can be observed (see Figure 2.11 (a)), although superimposed to the vorticity of the forced mode (positive on one side and negative on the other side). The maximal vorticity is close to 3.

Figure 2.11 (b) shows the strain rate s defined as the largest eigenvalue of the horizontal symmetric velocity gradient tensor

$$B_{ij} = \frac{1}{2}\Big[\partial_i u_j + \partial_j u_i\Big], \quad i, j = 1, 2. \tag{2.33}$$

The small scale structures of strain are smaller than their vortical counterpart with a maximum shear of the order of 1.

Finally, Figure 2.11 (c) shows the 2D divergence $\partial_x u + \partial_y v$ of the flow which exhibits again small scale structures with a maximum value close to 2.

In order to measure quantitatively the turbulent fluctuations, we have calculated the root-mean-square value of the vorticity (see Figure 2.11 (d)). It increases when the Ekman number decreases and saturates at a value close to 1. These experimental values are larger by a factor 2 than the theoretical prediction in the stable case. However, it was already observed for the forced mode that the vorticity maximum was larger in the experiments and the DNS than in the theory (see Figures 2.5 and 2.3).

The root-mean-square (rms) value of the strain rate is plotted in Figure 2.11 (e). It also increases when the Ekman number decreases and saturates at a value close to 0.5. These experimental values are again larger by a factor 2 than the theoretical prediction in the stable case.

Finally, the root-mean-square value of the 2D divergence is plotted in Figure 2.11 (f). Again,it increases when the Ekman number decreases and saturates at a value close to 0.5.

The values found here for an annulus are larger by a factor almost 3 than for a tilted cylinder. This is possibly due to the radial confinement which creates smaller structures and thus increases the velocity gradients. Fortunately, these values are still one order of magnitude smaller than for a Rushton turbine, consisting of six vertical

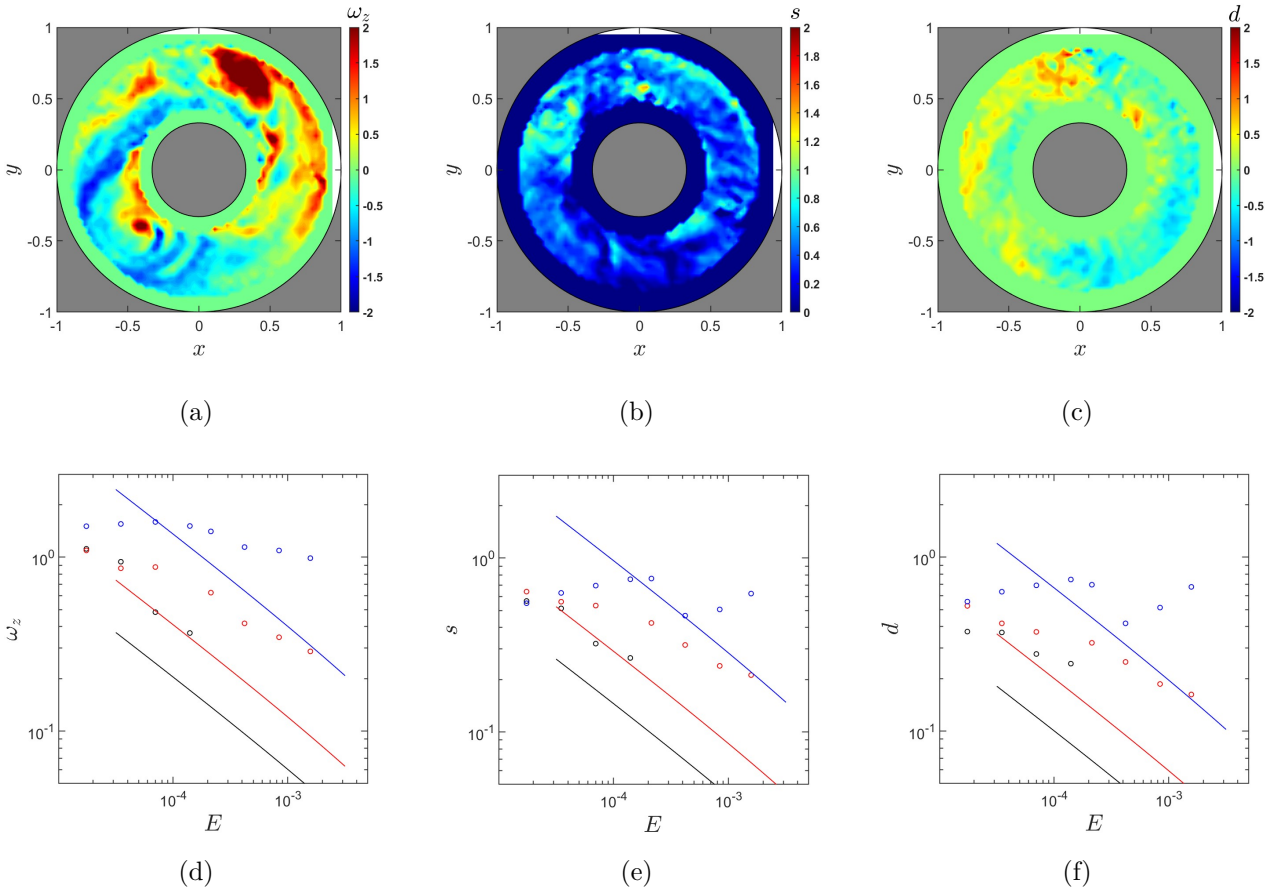
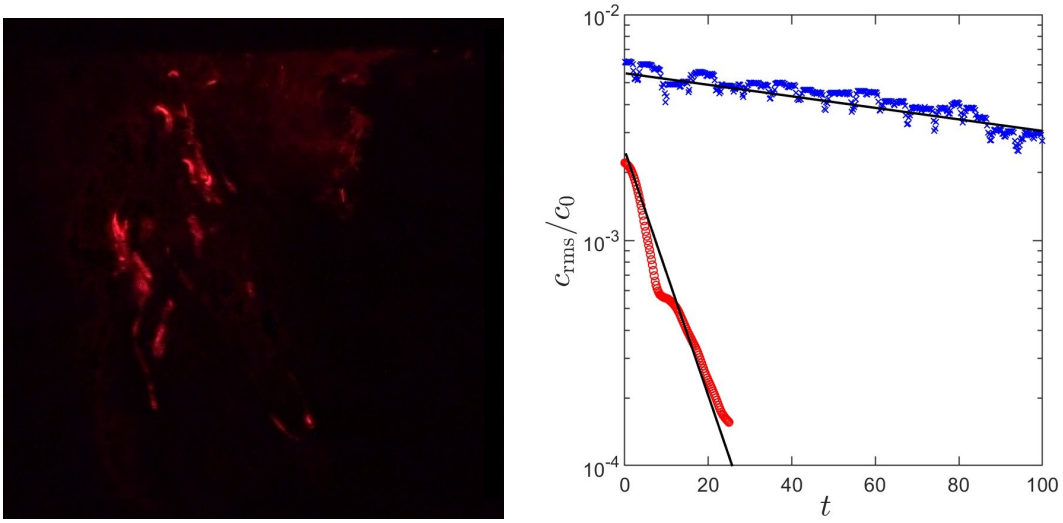


Fig. 2.11 Turbulent fluctuations characterized by the axial vorticity (a,d), the strain rate (b,e) and the horizontal divergence (c,f). (a,b,c) Examples of instantaneous fields are shown for $\alpha = 3^\circ$ and $E = 6.9 \times 10^{-5}$. (d,e,f) The rms values are plotted for $\alpha = 1.5^\circ$ in black, $\alpha = 3^\circ$ in red and $\alpha = 10^\circ$ in blue. The solid lines correspond to the stable forced mode with the forced Kelvin mode at an amplitude given by (2.21). $r_i = 0.33$, $h = h_1$.



(a) (b)

Fig. 2.12 (a) Example of observed pattern of the injected dye inside the fluid after one rotation.(b) Temporal evolution of the variance of concentration c_{rms}/c_0 for $h = h_1 = 1.306$ in red and $h = 1.57$ in blue, both with $r_i = 0.33$, $\alpha = 3°$ and $E = 2.1 \times 10^{-5}$. The two black lines are exponential fits $c_0 e^{-t/\tau}$ with $\tau = 8$ for $h = h_1$ and $\tau = 170$ for $h = 1.57$.

blades and a rotating horizontal disk (Nagata 1975) at the same angular velocity. This tilted annulus is thus possibly a good soft mixer if the mixing is sufficiently fast.

2.5 Mixing

To study quantitatively the mixing properties of this flow, we injected a blob of dye inside the fluid while the annulus is tilted. The dye is stretched and folded by the flow, leading to thin streaks of dye (see Figure 2.12 (a)). When the distance between two streaks is smaller than the diffusive thickness, the concentration becomes uniform if the streaks are homogeneously spread over the whole volume.

2.5.1 Variance of concentration

The efficiency of the mixing can be measured quantitatively by calculating the variance of the concentration

$$\frac{c_{\mathrm{rms}}}{c_0} = \frac{\sqrt{\langle c^2 \rangle - \langle c \rangle^2}}{c_0}. \tag{2.34}$$

Indeed, the variance decreases with time and eventually vanishes when the dye concentration is uniform. The variance is plotted in Figure 2.12 (b) for two different heights of fluid. It is clear that the variance decays much faster at the resonant height $h = h_1$ (red symbols) than at a height only 15% larger (blue symbols). This highlights

the fact that this flow is very sensitive to the height of the fluid due to the resonance of the forced Kelvin mode.

Figure 2.12 (b) also indicates that the concentration variance decreases exponentially with time. This is classical in turbulent flows and it can be explained by looking at a single lamella subject to a straining field γ. The length in the direction of the strain is proportional to $e^{\gamma t}$, which by conservation of mass leads to an exponential contraction of the thickness as $e^{-\gamma t}$ at early stages. When the thickness reaches the Batchelor scale $\sqrt{\kappa/\gamma}$ (Batchelor 1959), the lamella fades away. The thickness remains constant and the maximum concentration c must decay as $e^{-\gamma t}$ for mass conservation. The concentration variance is thus proportional to the length times the maximal amplitude squared, which decreases as $e^{-\gamma t}$. The characteristic time of mixing can thus be characterized empirically by the decay rate of c_{rms}/c_0, which is fitted by $e^{-t/\tau}$ for each experiment. In order to get a systematic picture of the efficiency of mixing, the time τ has been measured for different heights of fluids h, tilt angles α and Ekman numbers.

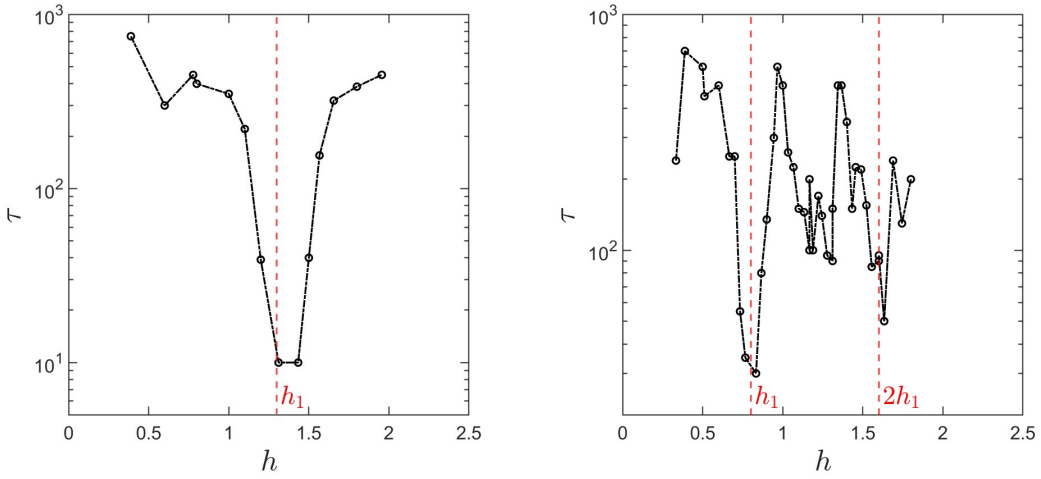
2.5.2 Decaying time as a function of h

A set of experiments is conducted at an Ekman number $E = 2.1 \times 10^{-5}$ sufficiently low for the instability to occur at the resonance (see Figure 2.13). As explained above, the mixing is much more efficient at the resonance of the forced Kelvin mode ($h = h_1$) than outside of the resonance. For an aspect ratio $r_i = 0.33$, the decaying time τ decreases by a factor 20 at $h = h_1$ compared to its average value outside of the resonance. This band of fast mixing has a width approximately equal to 20% of the resonant height. The faster decaying time is approximately equal to 10, which means that the variance decays by a factor e in less than two rotation periods.

For a larger aspect ratio $r_i = 0.56$ (see Figure 2.13 (b)), the decaying time has also two minima at the resonances of the first Kelvin mode ($h = h_1$ and $h = 2h_1$). It also seems to have another weaker minimum around $h = 1.2$, which could correspond to the third resonance of the second Kelvin mode ($h = 3h_2 = 1.16$). For this aspect ratio $r_i = 0.56$, the decaying time τ at the resonance is generally larger by a factor 2 than for $r_i = 0.33$. It may come from the weaker unstable flow due to the larger Ekman damping (see Section 2.4). It may also come from the narrow shape of the annulus, which prevents an efficient advection of the dye from the top to the bottom.

2.5.3 Decaying time as a function of E

The effect of the Ekman number is then studied for various tilt angles α and at the resonant heights (see Figure 2.14). For all experiments, the decaying time τ increases with the Ekman number. For example for $r_i = 0.33$, $h = h_1$ and $\alpha = 3°$ (see Figure 2.14 (a)), the decaying time increases rapidly from $\tau \sim 10$ to $\tau = 100$ when the Ekman number increases by factor 5 from $E = 2 \times 10^{-5}$ to $E \sim 10^{-4}$. The decaying time then seems to saturate when the Ekman number increases further. It should be noted that the flow becomes unstable at a critical value $E = 3 \times 10^{-4}$ for these parameters. It



(a) (b)

Fig. 2.13 Decaying time τ of the concentration variance as a function of h for (a) $r_i = 0.33$ and (b) $r_i = 0.56$. The red dashed lines indicate the theoretical resonance heights of the first mode. $E = 2.1 \times 10^{-5}$, $\alpha = 3°$.

means that the Ekman number must be at least 5 to 10 times smaller than the critical Ekman number for the flow to be sufficiently turbulent to create an efficient mixing. This behavior is quantitatively similar to the case of a tilted cylinder (Meunier 2020), where it was shown that it mixes as fast as using a Rushton turbine with a mixing time $\tau \sim 10$.

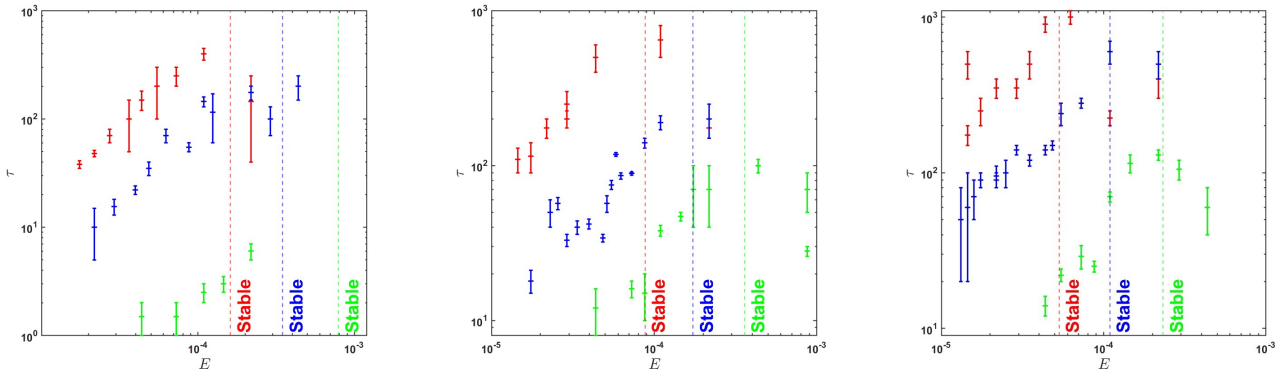
For a larger tilt angle $\alpha = 10°$, the decaying time τ evolves similarly than for $\alpha = 3°$ but it is 10 times faster. This result is expected since the amplitude of the turbulent fluctuations increases with α. At Ekman numbers smaller than 10^{-4} the decaying time seems to reach a plateau although experimental limitations prevent the study of smaller Ekman numbers.

Changing the aspect ratio from $r_i = 0.33$ to $r_i = 0.56$ does not change the behavior of the results. But it leads to a decrease in efficiency as already observed in Figure 2.13, with an increase by a factor at least two in the decaying time. Finally, changing the height of the water from $h = h_1$ to $h = 2h_1$ increases even more the decaying time by a factor about 2.

To conclude, the mixing is as efficient as in a tilted cylinder or using a Rushton turbine for a moderate aspect ratio $r_i = 0.33$ but slightly weaker for a large aspect ratio $r_i = 0.56$.

2.6 Conclusion

The flow inside a rotating annulus tilted with respect to the gravity has been characterized theoretically and experimentally. At low Froude numbers the free surface



(a) (b) (c)

Fig. 2.14 Decaying time τ of the concentration variance as a function of E for (a) $r_i = 0.33$ and $h = h_1$, (b) $r_i = 0.56$ and $h = h_1$ and (c) $r_i = 0.56$ and $h = 2h_1$. The symbols display different angles $\alpha = 1°$ (+), $\alpha = 3°$ (+) and $\alpha = 10°$ (+). The vertical dashed lines are positioned at the critical E value for the various experiments passing from stable (on the right) to unstable (on the left).

remains horizontal, which creates a counter-clockwise forcing of azimuthal wavenumber $m = 1$ in the frame rotating with the annulus. As already observed by Xu & Harlander (2020), it excites global inertial modes which can become resonant if the height of fluid is equal to a multiple of the half wavelength of the mode. Indeed, the excitation is then located at the node of the mode, such that the mode must have an infinite amplitude to satisfy the boundary condition imposed by the free surface.

The linear and viscous theory used for the cylinder (Meunier 2020) can be extended to the case of the annular cavity. The forced mode has been described analytically with no fitting parameter and is in excellent agreement with the experiments. At low Ekman numbers, the flow becomes unstable thanks to a triadic resonance instability where the forced mode triggers two free global modes of azimuthal wavenumbers $m = 9$ and $m = 10$, as already observed experimentally by Xu & Harlander (2020). We have developed a linear stability analysis which predicts the viscous threshold of the instability. It is in excellent agreement with the experiments despite the lack of fitting parameters. As far as we know, it is the first time that such an analysis is done in a rotating annulus. The annular geometry also generates a different type of instability which seems to be related to a centrifugal instability. Indeed, at large tilt angles, the solid body rotation is slowed down by the forced Kelvin mode. The inner cylinder tends to accelerate the fluid, leading to a centrifugally unstable forced mode in a narrow region around the inner cylinder.

The mixing efficiency of this flow is then characterized experimentally by injecting small blobs of dye. The characteristic mixing time (defined as the decaying time of the variance of concentration) is as fast as in a tilted cylinder or using a Rushton turbine at the same angular velocity for a moderate aspect ratio $r_i = 0.33$ (between the inner and outer radius). The mixing time is slightly slower for a larger aspect ratio

$r_i = 0.56$. Since the shear is slightly larger (by a factor 2) in a tilted annulus than in a tilted cylinder, it seems that this annular mixer is not as smooth as a tilted cylinder. However, the shear is still an order of magnitude smaller than using a Rushton turbine for the same characteristic mixing time.

This annular mixer is thus an excellent candidate for large photobioreactors which are used for example for the growth of microalgae. Indeed, it allows for a simultaneous illumination from the outer and the inner cylinders. It thus increases the total amount of light delivered to the photobioreactor while remaining below the maximum intensity that creates photobleaching of the microalgae. This geometry is especially efficient for large concentrations of microalgae since the light is strongly attenuated after a few centimeters. For such concentrations, a cylindrical photobioreactor would be limited to diameters of the order of 10 to 20 centimeters, corresponding to volumes of the order of 5 to 50 liters. With an annular photobioreactor, it is possible to reach volumes of the order of 600 liters with inner and outer radii equal to 50 and 70 centimeters respectively (for $h = 2h_1$).

2.7 Appendix

2.7.1 Amplitude viscous correction

We have seen that the amplitudes in the linear theory are divergent. This is obviously a nonphysical behavior. In fact the viscous effects saturate the resonance at a finite value of the amplitude. This effect due to the Ekman pumping (Greenspan 1968) near the walls where there is the Ekman boundary layer (Ekman 1905). In the layer, of depth $\propto \sqrt{E}$, there is an additional motion due to the viscous damping of order $\sqrt{E}$

$$\tilde{\mathbf{u}} \cdot \hat{\mathbf{n}} = \sqrt{E}\Big[- \frac{\delta_- + \delta_+}{2}(\hat{\mathbf{n}} \cdot \nabla)(\mathbf{u_b} \cdot \hat{\mathbf{n}}) + \frac{\delta_- - \delta_+}{\varpi}\partial_z(\hat{\mathbf{n}} \cdot \mathbf{u_b})\Big]. \tag{2.35}$$

where we have defined

$$\delta_+ = \begin{cases} \frac{1-i}{\sqrt{2(\varpi - f)}}, & \text{for } \varpi > f \\ \frac{1+i}{\sqrt{2|\varpi - f|}}, & \text{for } \varpi < f \end{cases}, \quad \delta_- = \begin{cases} \frac{1-i}{\sqrt{2(\varpi + f)}}, & \text{for } \varpi + f > 0 \\ \frac{1+i}{\sqrt{2|\varpi + f|}}, & \text{for } \varpi + f < 0 \end{cases}, \tag{2.36}$$

and $f = 2\cos(\hat{n} \cdot \hat{\Omega})$.

To see that we consider the solubility condition, obtained by multiplying the N-S equation with the complex conjugate of the jth mode

$$\bar{\mathbf{u}}_j = \Big(\bar{u}_j \cos(k_j z), \bar{v}_j \cos(k_j z), \bar{w}_j \sin(k_j z)\Big) e^{-i(\theta + t)}, \tag{2.37}$$

and integrating over the cylinder excluding Ekman boundary layers ($\tilde{V}$)

$$\iiint_{\tilde{V}} \bar{\mathbf{u}}_j \cdot \Big[i\mathbf{u} + 2\hat{\mathbf{z}} \wedge \mathbf{u} + \nabla p - E\nabla^2 \mathbf{u} \Big] d^3r = 0. \tag{2.38}$$

To find a better expression we consider the scalar product of $\mathbf{u}$ and the N-S equation for $\bar{\mathbf{u}}_j$

$$-i\mathbf{u} \cdot \bar{\mathbf{u}}_j + 2\mathbf{u} \cdot \hat{\mathbf{z}} \wedge \bar{\mathbf{u}}_j = -\mathbf{u} \cdot \nabla \bar{p}_j, \tag{2.39}$$

the symmetry $2\mathbf{u} \cdot \hat{\mathbf{z}} \wedge \bar{\mathbf{u}}_j = -2\bar{\mathbf{u}}_j \cdot \hat{\mathbf{z}} \wedge \mathbf{u}$ and the incompressibility condition to have [2]

$$\oint_{\partial \tilde{V}} \Big(\bar{p}_j \mathbf{u} + p \bar{\mathbf{u}}_j \Big) \cdot \mathbf{n} d\Sigma - E \iiint_{\tilde{V}} \bar{\mathbf{u}}_j \cdot \nabla^2 \mathbf{u} d^3x = 0. \tag{2.40}$$

First consider the top surface (free surface) we have from the first term ($\propto \bar{p}_j u$)

$$-\int_0^{2\pi} \int_{r_i}^1 d\theta r dr \Big[\bar{p}_j(r, z = h) e^{-i(\theta + t)} \Big(\alpha r \sin(\theta + t) \Big) \Big] \equiv -\alpha F, \tag{2.41}$$

and the second term ($\propto p\bar{u}_j$)

$$-\int_0^{2\pi} \int_{r_i}^1 d\theta r dr \Big[p(r, z = h) \bar{w}_j(r, z = h) e^{-i(\theta + t)} \Big] \equiv A_j \sin(k_j h) T. \tag{2.42}$$

The bottom contribution comes only from the first term

$$\int_0^{2\pi} \int_{r_i}^1 d\theta r dr \left[\bar{p}_j(r, z = 0) e^{-i(\theta + t)} \tilde{\mathbf{u}} \cdot \hat{n} \right], \tag{2.43}$$

and using the expression of the Ekman pumping (2.35)

$$\int_0^{2\pi} \int_{r_i}^1 d\theta r dr \left[\bar{p}_j(r, z = 0) e^{-i(\theta + t)} \left(\frac{\sqrt{E}}{2} \Big(-3\delta_+ + \delta_- \Big) \partial_z w \Big|_{z=0} \right) \right] \equiv A_j \sqrt{E} B, \tag{2.44}$$

where $\delta_+ = (1 + i)/2$ and $\delta_- = (1 - i)/\sqrt{6}$.

The same happens for the inner and outer cylinders:

$$\int_0^{2\pi} \int_0^h d\theta dz \Big[\bar{p}_j(r = 1, z) e^{-i(\theta + t)} \left(-\delta \partial_r u \Big|_{r=1} \right) \Big] \equiv A_j \sqrt{E} C_e, \tag{2.45}$$

$$\int_0^{2\pi} \int_0^h d\theta dz \Big[\bar{p}_j(r = r_i, z) e^{-i(\theta + t)} \left(-\delta \partial_r u \Big|_{r=ri} \right) \Big] \equiv A_j \sqrt{E} C_i, \tag{2.46}$$

where $\delta = (1 - i)/\sqrt{2}$.

[2]The surface integrals are carried out by considering $\mathbf{n}$ oriented towards the inside of the annular cavity.

Finally the last term (volume integral) has an easy analytical expression

$$\iiint_{\tilde{V}} \bar{\mathbf{u}}_j \cdot \nabla^2 \mathbf{u} d^3x = -4k_j^2 \iiint_{\tilde{V}} \bar{\mathbf{u}}_j \cdot \mathbf{u} d^3x \equiv A_j EV. \tag{2.47}$$

With these definitions we can write the equation for viscous amplitude at the resonance

$$A_j = \frac{\alpha F}{T \sin(k_j h) + \sqrt{E}\Big(B + C_e + C_i\Big) + EV}. \tag{2.48}$$

All the corrections calculated are $\propto E$ and in the limit $E \to 0$ we have the inviscid theory (see Equation (2.17)) and from the definition it is easy to prove it.

These coefficients can be given analytically as:

$$C_e = \frac{2\sqrt{2}h(1+i)(1+k_j^2)}{\pi} \left[1 + \mathrm{sinc}(2hk_j)\right] \tag{2.49}$$

with $\mathrm{sinc}(x) = \sin(x)/x$

$$C_i = \frac{\sqrt{2}h(1+i)(1+k_j^2 r_i^2) c_j^J \left[c_j^J J_1(\sqrt{3}k_j r_i) + c_j^Y Y_1(\sqrt{3}k_j r_i)\right]}{r_i^2 \left[Y_1(\sqrt{3}k_j r_i) + \sqrt{3}k_j r_i Y_0(\sqrt{3}k_j r_i)\right]} \left[1 + \mathrm{sinc}(2hk_j)\right] \tag{2.50}$$

$$F = 2i\pi \frac{c_j^J \left[J_2(\sqrt{3}k_j) - r_i^2 J_2(\sqrt{3}k_j r_i)\right] + c_j^Y \left[Y_2(\sqrt{3}k_j) - r_i^2 Y_2(\sqrt{3}k_j r_i)\right]}{\sqrt{3}k_j} \cos(k_j h) \tag{2.51}$$

$$T = 2i\pi k_j \cos(k_j h) I \tag{2.52}$$

$$B = i\pi k_j^2 \left(\frac{1-i}{\sqrt{6}} - 3\frac{1+i}{\sqrt{2}}\right) I \tag{2.53}$$

with

$$I = \int_{r=r_i}^{1} \left[c_j^J J_1(\sqrt{3}k_j r) + c_j^Y Y_1(\sqrt{3}k_j r)\right]^2 dr. \tag{2.54}$$

2.7.2 Amplitude equations for triadic instability

This result is achieved by doing a linear stability analysis, thanks to the fact that we have the small parameters α and E, of the complete Navier-Stokes equation. To perform the linear stability analysis a perturbation is added to the forced Kelvin mode

$$\mathbf{u} = \mathbf{u}_f + A'\mathbf{u}' + A''\mathbf{u}'', \tag{2.55}$$

where $\mathbf{u}_f$ is the forced Kelvin mode given in (2.10) and $\mathbf{u}'$, $\mathbf{u}''$ are the two free Kelvin modes triggered by the forced mode.

In general the free Kelvin modes are defined by (Xu & Harlander 2020)

$$\mathbf{u}' = \mathrm{Re}\left[A' \begin{pmatrix} u'(r)\cos(k'z) \\ v'(r)\cos(k'z) \\ w'(r)\sin(k'z) \end{pmatrix} e^{i(m'\theta+\varpi' t)}\right], \tag{2.56}$$

where

$$\begin{cases} p'(r) = c'^J J_{m'}\left(\sqrt{\frac{4}{\varpi'^2}-1}k'r\right) + c'^Y Y_{m'}\left(\sqrt{\frac{4}{\varpi'^2}-1}k'r\right) \\ u'(r) = -\frac{i}{4-\varpi'^2}\left(\varpi'\partial_r p' + \frac{2m'}{r}p'\right) \\ v'(r) = \frac{1}{4-\varpi'^2}\left(2\partial_r p' + \frac{\varpi' m'}{r}p'\right) \\ w'(r) = -i\frac{k'}{\varpi'}p' \end{cases}, \tag{2.57}$$

and

$$\begin{cases} c'^J = \frac{1}{2}\sqrt{\frac{4}{\omega'^2}-1}k'\varpi'\left[Y_{m'-1}\left(\sqrt{\frac{4}{\omega'^2}-1}k'\right) - Y_{m'+1}\left(\sqrt{\frac{4}{\omega'^2}-1}k'\right)\right] + 2m'Y_{m'}\left(\sqrt{\frac{4}{\omega'^2}-1}k'\right) \\ c'^Y = \frac{1}{2}\sqrt{\frac{4}{\omega'^2}-1}k'\varpi'\left[J_{m'+1}\left(\sqrt{\frac{4}{\omega'^2}-1}k'\right) - J_{m'-1}\left(\sqrt{\frac{4}{\omega'^2}-1}k'\right)\right] - 2m'J_{m'}\left(\sqrt{\frac{4}{\omega'^2}-1}k'\right) \end{cases}. \tag{2.58}$$

At the resonance of the jth forced Kelvin mode the amplitude scales as $A_j \sim \alpha E^{-1/2}$ and is taken as the parameter for the analysis. Assuming a small dependence in time on A' and A'' ($\partial_t A' \sim A_j$) and that the two free modes are not exactly resonant ($k' = k'_{\mathrm{res}} + \Delta k'$ with $\Delta k \sim \mathcal{O}(A_j)$), we find the evolution equation (Lagrange *et al.* 2011)

$$\begin{cases} \partial_t A' = N'\bar{A}_j A'' - D'A' \\ \partial_t A'' = N''A_j A' - D''A'' \end{cases}, \tag{2.59}$$

where the non-linear terms are [3]

$$N' = \frac{-i\left(\frac{k''}{\varpi''} - k\right) I_{\mathrm{coupling}}}{\int_{r_i}^1 \left(|u'|^2 + |v'|^2 + |w'|^2\right) r dr}, \tag{2.60}$$

$$N'' = \frac{i\left(k - \frac{\pm k'}{\varpi'}\right) I_{\mathrm{coupling}}}{\int_{r_i}^1 \left(|u''|^2 + |v''|^2 + |w''|^2\right) r dr}, \tag{2.61}$$

[3]We want to stress the fact that this result is different from the one found in Lagrange *et al.* (2011) because we use a different basis.

with

$$I_{\text{coupling}} = \int_{r_i}^{1} \begin{vmatrix} u'' & u' & u \\ -v'' & v' & v \\ -w'' & \pm w' & w \end{vmatrix} r dr, \tag{2.62}$$

where $|.|$ is the determinant and the plus sign corresponds to the case $k'' = |k + k'|$ and the minus sign corresponds to the case $k'' = |k - k'|$.

These formulae can be linked to the values found in the literature in the case of the cylinder taking the limit $r_i \to 0$. In this limit the coefficient c^Y vanishes such that the solution (2.11) is equivalent to the classical solution in a cylinder (Meunier 2020) except that it is $c^J/2$ times larger. It should be noted that the boundary condition $u = 0$ at $r = r_i$ virtually disappears when r_i tends to 0 since this boundary condition creates a perturbation of the flow only in a small region of size r_i, that disappears when r_i tends to 0. The Kelvin modes of an annulus with very small r_i are thus exactly the same as the Kelvin modes of a cylinder.

The non linear coefficients given by Meunier (2020) are related to our coefficient by the relation

$$\begin{cases} N'_{\text{Meu}} = \lim_{r_i \to 0} \frac{i2c_5^J}{c_6^J c_1^J} N' \\ N''_{\text{Meu}} = \lim_{r_i \to 0} \frac{-i2c_6^J}{c_5^J c_1^J} N'' \end{cases}, \tag{2.63}$$

due to the observation $c^Y \ll c^J$ for $r_i \to 0$.

The dispersion relation gives the resonance for $m' = 5$ and $m'' = 6$ with resonant height $h = 1.99$, same value of the cylinder, and non linear coefficient

$$\begin{cases} N'_{\text{Meu}} = -1.26 \\ N''_{\text{Meu}} = -1.95 \end{cases}, \tag{2.64}$$

that gives a value of the growth rate with an error of 2%.

The other term

$$D' = s'\sqrt{E} + v'E + i\Delta k' q', \tag{2.65}$$

describes the viscous corrections

$$s' = \frac{k'\left[-\left(\frac{1}{2}\left(\delta'_+ + \delta'_-\right) + \frac{1}{\varpi'}\left(\delta'_+ - \delta'_-\right)\right)\right] \int_{r_i}^1 p'w' r dr - \frac{\delta'}{2h}\left[\left(p'\partial_r u'\right)\Big|_{(r=r_i)} + \left(p'\partial_r u'\right)\Big|_{(r=r_i)}\right]}{\int_{r_i}^1 \left(|u'|^2 + |v'|^2 + |w'|^2\right) r dr}, \tag{2.66}$$

$$v' = \frac{4k'^2}{\varpi'^2}, \tag{2.67}$$

and the detuning effect

$$q' = -ik' \frac{\int_{r_i}^1 w'p' r dr}{\int_{r_i}^1 \left(|u'|^2 + |v'|^2 + |w'|^2\right) r dr}. \tag{2.68}$$

	$r_i = 0.33\ h = h_1$	$r_i = 0.56\ h = h_1$	$r_i = 0.56\ h = 2h_1$
N'	$1.574i$	$2.249i$	$2.249i$
N''	$-1.990i$	$-3.142i$	$-3.142i$
s'	$0.351 + 0.591i$	$-0.828 - 0.721i$	$-0.211 - 0.563i$
s''	$1.297 + 0.163i$	$-1.771 + 0.060i$	$-1.147 - 0.231i$
v'	191.071	517.223	517.223
v''	219.945	583.887	583.887
q'	0.332	$0.332i$	$0.332i$
q''	-0.596	$-0.590i$	$-0.590i$
$\Delta k'$	0.012	-0.039	-0.039
$\Delta k''$	-0.012	0.039	0.039

Table 2.3 Numerical values of the viscous terms for the triadic resonance, for $r_i = 0.33$ ($m' = 9$, $m'' = 10$) and $r_i = 0.56$ ($m' = 17$, $m'' = 18$) at the resonance $h = h_1$ and $h = 2h_1$.

The numerical values of the correction terms used for comparison with the experiments are given in Table 2.3.

2.7.3 Small gap limit

We want to study the solution in the small gap limit ($r_i \to 1$ or $\epsilon \to 0$, where $\epsilon = 1 - r_i$ is the gap). In this limit we can rewrite the pressure equation (2.9) with the rescaling $\tilde{r} = (r-1)/\epsilon$. In this variable the term $r^{-1}\partial_r$ is subdominant with respect to ∂_r^2, so under the assumption of large wavenumber k and m (which are of order ϵ^{-1}) the equation becomes (when coming back to the variable r)

$$(\partial_r^2 + \lambda^2)p(r) = 0, \quad \lambda = \sqrt{k^2\left(\frac{4}{\varpi^2} - 1\right) - m^2}. \tag{2.69}$$

Adding the boundary conditions $u(1) = u(1-\epsilon)$ gives the solution

$$p(r) = c\left(\cos[\lambda(r-1)] - \frac{2m}{\varpi\lambda}\sin[\lambda(r-1)]\right), \quad \sin(\lambda\epsilon) = 0. \tag{2.70}$$

We want to connect this solution with the forced mode in equation (2.11) by imposing to have the same amplitude in the limit of small ϵ. Taking the asymptotic formula for J_m and Y_m, in equations (2.58) and (2.57), we can show that the two relations are equal if $c = 2\varpi/\pi$.

Finally, using the relationships between flow and pressure, we find the complete solution

$$\begin{cases} p = \frac{2}{\pi\lambda}\left(\varpi\lambda\cos[\lambda(r-1)] - 2m\sin[\lambda(r-1)]\right) \\ u = \frac{2i(\lambda^2\varpi^2+4m^2)}{\pi\lambda(4-\varpi^2)}\sin[\lambda(r-1)] \\ v = -\frac{2}{\pi\lambda(4-\varpi^2)}\left[m\lambda(4-\varpi^2)\cos[\lambda(r-1)] + 2\varpi(\lambda^2+m^2)\sin[\lambda(r-1)]\right] \\ w = -i\frac{2k}{\pi\lambda\varpi}\left(\varpi\lambda\cos[\lambda(r-1)] - 2m\sin[\lambda(r-1)]\right) \end{cases} . \quad (2.71)$$

For the forced mode, $m = 1$ and $\varpi = 1$, the dispersion relation (2.69) gives the asymptotic axial wavenumber $k_j = j\pi/\sqrt{3}\epsilon$, so the forced mode is resonant when h is a multiple of half wavelength $h_j = \pi/k_j$.

Assuming

$$\begin{cases} \varpi'' - \varpi' = 1 \\ m'' - m' = 1 \end{cases} , \quad (2.72)$$

we have the triadic resonant instability, with non linear coefficient N' and N'' given by the equation (2.60)-(2.61). Assuming the case $k'' = |k+k'|$ for simplicity of description[4], these identities can be calculated for small ϵ, by changing $rdr \to dr$ in all integrals, and are

$$N' = \frac{i\left(\frac{k''}{\varpi''} - k\right)\pi^2\lambda'^2\varpi'^2}{16k'^2(k'^2+m'^2)\epsilon} I_{\text{coupling}}, \quad (2.73)$$

$$N'' = \frac{-i\left(k - \frac{k'}{\varpi'}\right)\pi^2\lambda''^2\varpi''^2}{16k''^2(k''^2+m''^2)\epsilon} I_{\text{coupling}}, \quad (2.74)$$

where I_{coupling} can be also calculated analytically.

If $\lambda'' + \lambda' + \lambda$ is an odd multiple of the fundamental wavelength π/ϵ

$$\begin{aligned} I_{\text{coupling}} = & \frac{-16}{\pi^3(\lambda-\lambda'-\lambda'')(\lambda+\lambda'-\lambda'')(\lambda-\lambda'+\lambda'')(\lambda+\lambda'+\lambda'')} \\ & \left[(k'm''-k''m')\left((-\lambda^2+\lambda'^2+\lambda''^2)+\frac{8k'k''}{\varpi'\varpi''}\right)\frac{(k^2+m^2)}{\varpi}\right. \\ & + (k''m-km'')\left((\lambda^2-\lambda'^2+\lambda''^2)+\frac{8kk''}{\varpi\varpi''}\right)\frac{(k'^2+m'^2)}{\varpi'} \\ & \left. + (k'm-km')\left((\lambda^2+\lambda'^2-\lambda''^2)+\frac{8kk'}{\varpi\varpi'}\right)\frac{(k''^2+m''^2)}{\varpi''}\right] \end{aligned} . \quad (2.75)$$

[4]At the end of the subsection we give the change in all the equations in the case $k'' = |k - k'|$.

λ''	λ'	λ	k''	k'	k	m'	ϖ''	ϖ'	$\epsilon^2\sigma$
$2\pi/\epsilon$	π/ϵ	π/ϵ	$2\pi/\sqrt{3}\epsilon$	$\pi/\sqrt{3}\epsilon$	$\pi/\sqrt{3}\epsilon$	$9/\epsilon$	0.628	-0.374	0.702
$3\pi/\epsilon$	π/ϵ	$2\pi/\epsilon$	$4\pi/\sqrt{3}\epsilon$	$2\pi/\sqrt{3}\epsilon$	$2\pi/\sqrt{3}\epsilon$	$6.5/\epsilon$	0.604	-0.393	0.659
$3\pi/\epsilon$	$2\pi/\epsilon$	π/ϵ	$2\pi/\sqrt{3}\epsilon$	$\pi/\sqrt{3}\epsilon$	$\pi/\sqrt{3}\epsilon$	$19/\epsilon$	0.647	-0.370	2.733
$4\pi/\epsilon$	$2\pi/\epsilon$	$2\pi/\epsilon$	$4\pi/\sqrt{3}\epsilon$	$2\pi/\sqrt{3}\epsilon$	$2\pi/\sqrt{3}\epsilon$	$18/\epsilon$	0.628	-0.374	2.806
π/ϵ	π/ϵ	$2\pi/\epsilon$	$4\pi/\sqrt{3}\epsilon$	$2\pi/\sqrt{3}\epsilon$	$2\pi/\sqrt{3}\epsilon$	$20/\epsilon$	0.675	-0.353	2.406
π/ϵ	π/ϵ	π/ϵ	$2\pi/\sqrt{3}\epsilon$	$\pi/\sqrt{3}\epsilon$	$\pi/\sqrt{3}\epsilon$	$10/\epsilon$	0.654	-0.341	0.306
$2\pi/\epsilon$	$2\pi/\epsilon$	$2\pi/\epsilon$	$4\pi/\sqrt{3}\epsilon$	$2\pi/\sqrt{3}\epsilon$	$2\pi/\sqrt{3}\epsilon$	$20/\epsilon$	0.654	-0.341	0.613
$3\pi/\epsilon$	$3\pi/\epsilon$	$3\pi/\epsilon$	$6\pi/\sqrt{3}\epsilon$	$3\pi/\sqrt{3}\epsilon$	$3\pi/\sqrt{3}\epsilon$	$30/\epsilon$	0.654	-0.341	0.919
$4\pi/\epsilon$	$4\pi/\epsilon$	$4\pi/\epsilon$	$8\pi/\sqrt{3}\epsilon$	$4\pi/\sqrt{3}\epsilon$	$4\pi/\sqrt{3}\epsilon$	$40/\epsilon$	0.654	-0.341	1.225
$2\pi/\epsilon$	$2\pi/\epsilon$	π/ϵ	$2\pi/\sqrt{3}\epsilon$	$\pi/\sqrt{3}\epsilon$	$\pi/\sqrt{3}\epsilon$	$10/\epsilon$	0.654	-0.341	0.190
$2\pi/\epsilon$	$2\pi/\epsilon$	$3\pi/\epsilon$	$6\pi/\sqrt{3}\epsilon$	$3\pi/\sqrt{3}\epsilon$	$3\pi/\sqrt{3}\epsilon$	$7.7/\epsilon$	0.571	-0.426	0.038
$4\pi/\epsilon$	$4\pi/\epsilon$	π/ϵ	$2\pi/\sqrt{3}\epsilon$	$\pi/\sqrt{3}\epsilon$	$\pi/\sqrt{3}\epsilon$	$20/\epsilon$	0.675	-0.341	0.607
$4\pi/\epsilon$	$4\pi/\epsilon$	$3\pi/\epsilon$	$6\pi/\sqrt{3}\epsilon$	$3\pi/\sqrt{3}\epsilon$	$3\pi/\sqrt{3}\epsilon$	$20/\epsilon$	0.624	-0.341	0.347

Table 2.4 Examples of growth rate in the asymptotic theory for $h = \pi/k$. All of them show that for $\epsilon \lesssim 0.01$ the value of $\epsilon^2\sigma$ becomes constant. The table shows some different cases in the triad of λ satisfying the condition (2.72) and $k'' = k + k'$.

Than if $\lambda''+\lambda'+\lambda$ is an even multiple of the fundamental wavelength π/ϵ, $I_{\text{coupling}} = 0$ unless $\lambda'' = |\lambda \pm \lambda'|$, in that case

$$I_{\text{coupling}} = \frac{-4\epsilon}{\pi^3}\Bigg[(k'k'' + m'm'')\left(\frac{k''}{\varpi''\lambda''} + \frac{k'}{\varpi'(\pm\lambda')}\right)\frac{(k^2+m^2)}{\lambda} - (kk'' + mm'')\left(\frac{k''}{\varpi''\lambda''} + \frac{k}{\varpi\lambda}\right)\frac{(k'^2+m'^2)}{(\pm\lambda')} - (kk' + mm')\left(\frac{k'}{\varpi'(\pm\lambda')} - \frac{k}{\varpi\lambda}\right)\frac{(k''^2+m''^2)}{\lambda''}\Bigg] \quad , \tag{2.76}$$

where the plus sign corresponds to the case $\lambda'' = |\lambda+\lambda'|$ and the minus sign corresponds to the case $\lambda'' = |\lambda - \lambda'|$. In the case of $k'' = |k - k'|$ all the equations written before are valid under the transformation $k' -> -k'$.

Some examples from the above formulae are given in Table 2.4.

The interesting case for comparing asymptotic and exact theory is $\lambda'' = \lambda' = \lambda = \pi/\epsilon$, we can plot the numerical values of the growth rate as a function of ϵ of the exact and asymptotic theory, as shown in Figure 2.15.

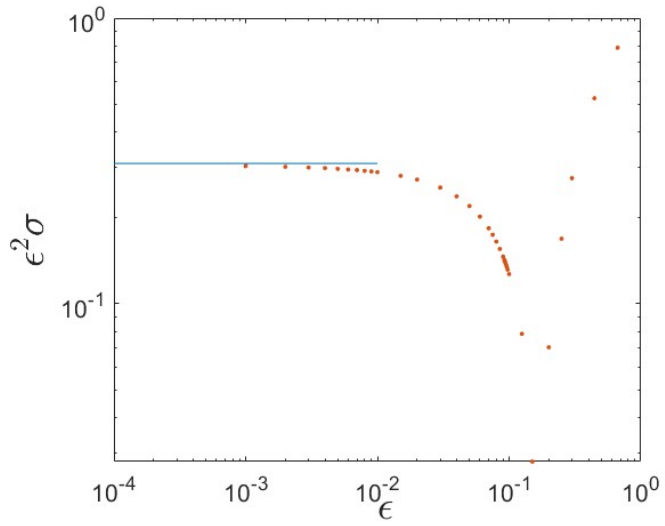


Fig. 2.15 Comparison of asymptotic (blue) and exact theory (red) in growth rate values. It can be seen that the exact theory is asymptotically equivalent to the case where $\lambda'' = \lambda' = \lambda = \pi/\epsilon$.

Chapter 3

Diffuselet Method : Numerical Implementation

3.1 Numerical Cost

When it comes to numerical calculations, especially in the DNS domain, the first problem that arises is the demand for the resources required to perform the simulation.

In the case of fluid dynamics, when one wants to describe the evolution of a fluid in the most general cases, one has to solve the Kolmogorov scale $\eta_{\mathrm{K}} = \left(\nu^3/\langle\epsilon\rangle\right)^{1/4}$, where $\langle\epsilon\rangle$ is the mean kinetic energy dissipation rate. Considering a uniform square mesh of size Δl in a volume $V = L^3 = (N\Delta l)^3$, it is necessary to consider a number of points $N^3 = \left(L/\eta_{\mathrm{K}}\right)^3 = (Re^{3/4})^3$ to solve the Kolmogorov scale. For instance, at $Re = 10^4$, the required resolution demands approximately 1 GB of memory.

By introducing a passive scalar into the dynamics, a new parameter, the Schmidt number comes into play. Associated with this dynamic, as we saw earlier, we must consider the Batchelor scale $\eta_{\mathrm{B}} = \left(\nu D^2/\epsilon\right)^{1/4} = \eta_{\mathrm{K}}/Sc^{1/2}$. Under the assumption of large Schmidt number ($Sc \gg 1$), Batchelor's scale is smaller than Kolmogorov scale, so if we wish to simulate the evolution of the scalar field up to the dissipative regime, we must resolve this scale. Similarly to the flow case, it follows that the number of points to be considered for the simulation becomes $N^3 = \left(L/\eta_{\mathrm{B}}\right)^3 = (Re^{3/4}Sc^{1/2})^3$. Thus, large Schmidt's number greatly increases the resources required to simulate the mixing of a passive scalar. Introducing a passive scalar with $Sc = 10^3$ in the example above, where $Re = 10^4$, increases the memory requirement to approximately 100 TB.

An alternative approach has been proposed (Meunier & Villermaux 2010), called diffusive strip method, for the study a 2D scalar mixing valid in the large Péclet number limit. This method makes it possible to approximate the evolution of the scalar field by using strips, discretized by N Lagrangian points. Thus, having a prescribed field, which in general can be simulated in parallel using DNS, one does not have to solve the Batchelor scale, it simplifies the simulation to just the calculation of the Lagrangian trajectories of the strip and the addition of a posteriori diffusion. Subsequently, this

method was extended to the 3D case (Martínez-Ruiz *et al.* 2018) by means of sheets using the same calculation principle.

In the methods set out above, the approximating elements of the field are thought of as a discrete mesh of the sheet itself, i.e. they are considered connected so that it is possible to reconstruct the scalar field at the desired time. If we weaken this assumption by considering independent surface elements, as representatives of the statistical ensemble to characterize the field, we arrive at the method introduced theoretically in Section 1.3.2 called the Diffuselet method.

In the following, we will describe the algorithm used to simulate the evolution of this ensemble and calculate the observables required for mixing.

3.2 From the theory to the algorithm

Let us consider that we have a prescribed velocity field $\mathbf{u}(\mathbf{x}, t)$. This field may be known analytically (in time and space), greatly simplifying the algorithm and avoiding the need to use a mesh for possible positions. Alternatively, if the field is known on a mesh (again in time and space), as a result of a DNS or through experimental data, the point velocity required for the advection calculation is interpolated from the mesh by the most appropriate method.

Once the velocity field is fixed, the initial conditions for the concentration field must be defined. That is, the number of diffuselets N must be fixed, each with an initial position $\{\mathbf{x}_i^0\}_{i=1,..,N}$ and geometric parameters $\{s_i^0\}_{i=1,..,N}$ and $\{\delta A_i^0\}_{i=1,..,N}$.

The first step of the algorithm is then to calculate the trajectories of the diffuselets, via discretization of advective equation (1.108). For this, a fourth-order Runge-Kutta method was chosen. So fixing the time step Δt the algorithm for the advection can be calculated as follows:

$$\mathbf{x}_i(t + \Delta t) = \mathbf{x}_i(t) + \frac{\Delta t}{6} \left(\mathbf{k}_1 + 2\mathbf{k}_2 + 2\mathbf{k}_3 + \mathbf{k}_4 \right), \tag{3.1}$$

where we used the weighted average of four increments

$$\begin{cases} \mathbf{k}_1 = \mathbf{u}(\mathbf{x}_i(t), t) \\ \mathbf{k}_2 = \mathbf{u}\left(\mathbf{x}_i(t) + \frac{\Delta t}{2}\mathbf{k}_1, t + \frac{\Delta t}{2}\right) \\ \mathbf{k}_3 = \mathbf{u}\left(\mathbf{x}_i(t) + \frac{\Delta t}{2}\mathbf{k}_2, t + \frac{\Delta t}{2}\right) \\ \mathbf{k}_4 = \mathbf{u}\left(\mathbf{x}_i(t) + \Delta t\mathbf{k}_3, t + \Delta t\right) \end{cases} . \tag{3.2}$$

Explicitly the different increments are given by the slopes (see Figure 3.1):

- The first slope $\mathbf{k}_1$ is given by the Euler's method at the point $\mathbf{x}_i(t)$.
- The second slope $\mathbf{k}_2$ is calculated at the midpoint $\mathbf{x}_i(t) + \frac{\Delta t}{2}\mathbf{k}_1$.
- The third slope $\mathbf{k}_3$ refine the calculation at the midpoint $\mathbf{x}_i(t) + \frac{\Delta t}{2}\mathbf{k}_2$.

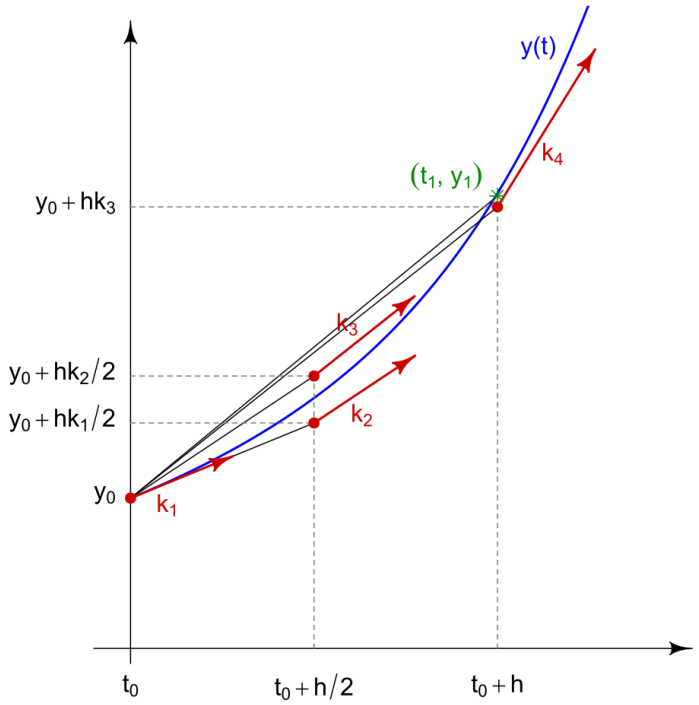


Fig. 3.1 Geometrical construction of a fourth-order Runge-Kutta method, expliciting the various step and slopes to achieve it. (Picture take from https://en.wikipedia.org/wiki/Runge%E2%80%93Kutta_methods).

- The last slope $\mathbf{k}_4$ is calculated at the end of the interval with the refined slope $\mathbf{k}_3$.

Once the evolution of the positions has been calculated, the local stretching of each diffuselet must be calculated. As we have seen, this results in the calculation of the evolution of the surface dispersion tensor $\boldsymbol{\mathcal{L}}_i$ defined in Equation (1.114).

In this equation, we need to know the velocity gradient tensor $\underline{\underline{\nabla \mathbf{u}}}$. Again, if the field is known analytically, the values of the tensor are derived trivially from the definition. In the case where the field is discrete, the calculation of the gradient tensor is non-trivial and must be defined with caution, so the interpolation scheme must be adapted. Assuming, therefore, that we have an appropriate definition of the velocity gradient tensor, we must fix the discretization of equation (1.114).

Discretization is again carried out using a fourth-order Runge-Kutta method. The scheme was chosen due to the observation that incompressibility ($\mathrm{Tr}(-\underline{\underline{\nabla \mathbf{u}}}^T) = -\nabla \cdot \mathbf{u} = 0$) leads to the integral of motion $\det(\boldsymbol{\mathcal{L}}_i) = e^{\int \mathrm{Tr}(-\underline{\underline{\nabla \mathbf{u}}}^T)dt} = 1$. It is shown (Girimaji & Pope 1990) that the discretisation that preserves the determinant most accurately is defined as:

$$\boldsymbol{\mathcal{L}}_i(t+\Delta t) = \boldsymbol{\mathcal{L}}_i(t) + \frac{\Delta t}{6}\Big\{\boldsymbol{H}(t)\cdot\boldsymbol{\mathcal{L}}_i(t) + [\boldsymbol{H}(t)+\boldsymbol{H}(t+\Delta t)]\cdot(\boldsymbol{L}_1+\boldsymbol{L}_2) + \boldsymbol{H}(t+\Delta t)\cdot\boldsymbol{L}_3\Big\}, \tag{3.3}$$

where we used the increments

$$\begin{cases} \boldsymbol{L}_1 = \boldsymbol{\mathcal{L}}_i(t) + \frac{\Delta t}{2}\boldsymbol{H}(t)\cdot\boldsymbol{\mathcal{L}}_i(t) \\ \boldsymbol{L}_2 = \boldsymbol{\mathcal{L}}_i(t) + \frac{\Delta t}{4}\left[\boldsymbol{H}(t)+\boldsymbol{H}(t+\Delta t)\right]\cdot\boldsymbol{L}_1 \\ \boldsymbol{L}_3 = \boldsymbol{\mathcal{L}}_i(t) + \frac{\Delta t}{2}\left[\boldsymbol{H}(t)+\boldsymbol{H}(t+\Delta t)\right]\cdot\boldsymbol{L}_2 \end{cases}, \tag{3.4}$$

and defined the tensor $\boldsymbol{H}(t) \coloneqq -\underline{\underline{\nabla \mathbf{u}}}^T(\mathbf{x}_i(t),t)$.

We want to note that the calculation performed here for surface stretching differs from the classical calculation of pair dispersion Lyapunov exponents, where $\boldsymbol{H}(t) = \underline{\underline{\nabla \mathbf{u}}}$.

Finally, to add the effect of diffusion, we see how we calculated the dimensionless time tensor defined in Equation (1.117). In this case, a three-point Adams-Bashforth method was used as follows:

$$\begin{aligned} \boldsymbol{\mathcal{T}}_i(t+\Delta t) = \boldsymbol{\mathcal{T}}_i(t) + \frac{4D}{(s_0^i)^2}\frac{\Delta t}{12}\Big[&23\left(\boldsymbol{\mathcal{L}}_i^T\boldsymbol{\mathcal{L}}_i\right)(t+\Delta t) - 16\left(\boldsymbol{\mathcal{L}}_i^T\boldsymbol{\mathcal{L}}_i\right)(t) \\ &+ 5\left(\boldsymbol{\mathcal{L}}_i^T\boldsymbol{\mathcal{L}}_i\right)(t-\Delta t)\Big], \end{aligned} \tag{3.5}$$

with an initial time step given by the trapezoid approximation

$$\boldsymbol{\mathcal{T}}_i(\Delta t) = \mathbb{1} + \frac{4D}{(s_0^i)^2}\frac{\Delta t}{2}\left[\left(\boldsymbol{\mathcal{L}}_i^T\boldsymbol{\mathcal{L}}_i\right)(\Delta t) + \mathbb{1}\right], \tag{3.6}$$

where the identity matrices are due to the initial conditions $\boldsymbol{\mathcal{T}}_i(0) = \mathbb{1}$ and $\left(\boldsymbol{\mathcal{L}}_i^T\boldsymbol{\mathcal{L}}_i\right)(0) = \mathbb{1}$.

The written code uses a time loop connecting the described equations, as schematized in the block diagram in Figure 3.2.

We are now ready to describe the calculation process for field variance and PDF at a given time. As mentioned above, the first step in this direction is the calculation of the eigenvalues $\eta_i'' \leq \eta_i' \leq \eta_i$ of the dimensionless time tensor $\boldsymbol{\mathcal{T}}_i$.

The calculation of the variance follows from the definition in Equation (1.120), which in our case invokes the use of the *integral* function in MATLAB, otherwise a discretization with the trapezoid method is sufficiently accurate for the purpose.

A regularization is necessary for the first time steps in order to avoid NaN values due to the divergence, when $G_i(\phi) = \eta_i$, in the integral defined in Equation (1.119). That is, in the first time steps there is a condition where $\eta_i'' = \eta_i' = \eta_i$ and the mean over the orientations is not well defined. If the variance has a NaN value, it is replaced by

$$\langle c_i^2 \rangle = \frac{\sqrt{\pi}\delta A_0 s_0}{\sqrt{2}}\frac{1}{\sqrt{\eta_i}}. \tag{3.7}$$

Concerning the calculation of the PDF, using the integral defined in Equation (1.121), what was said for the calculation of variances also applies here. Again, we have pathological cases, in this case for initial and final times in which the PDF is

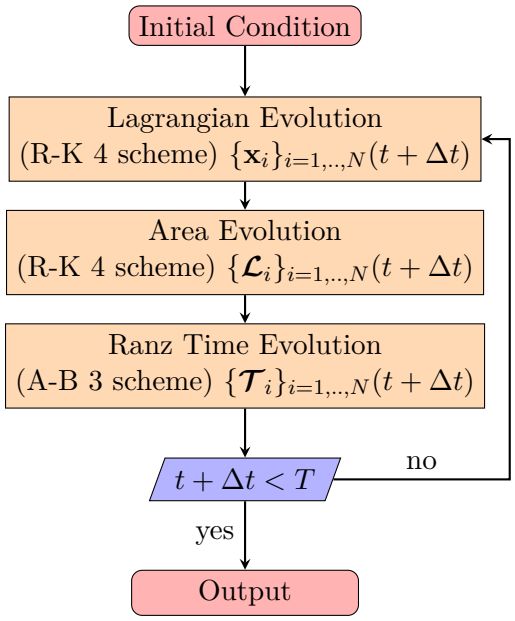


Fig. 3.2 Logical diagram of the algorithm used in the time evolution of the Diffuselet Method.

described by Dirac delta functions, as follows

$$P(c) = \begin{cases} \delta(c-1) & \text{for } t \simeq 0, \text{ i.e. } \eta_i < 1 + 10^{-6} \\ \delta(c) & \text{for } t >> t_{\text{mix}}, \text{i.e. } 1/\sqrt{\eta_i''} < 10^{-6} \end{cases}. \tag{3.8}$$

3.3 Validation of the code

For the validation of the code, we used two known cases that admit an analytical solution to the problem, namely the case of a linear shear flow and a 2D stagnation point. These cases are well known in the literature and obviously the Diffuselet method formalism is certainly not useful, but we will derive these solutions with this formalism to show an application of the method and check the program.

We fix the shear flow acting in the x direction with a constant proportional to y, i.e. we define the flow

$$\mathbf{u} = \begin{pmatrix} y \\ 0 \\ 0 \end{pmatrix}, \tag{3.9}$$

which gives us the velocity gradient tensor

$$-\underline{\underline{\nabla \mathbf{u}}}^T = \begin{pmatrix} 0 & 0 & 0 \\ -1 & 0 & 0 \\ 0 & 0 & 0 \end{pmatrix}. \tag{3.10}$$

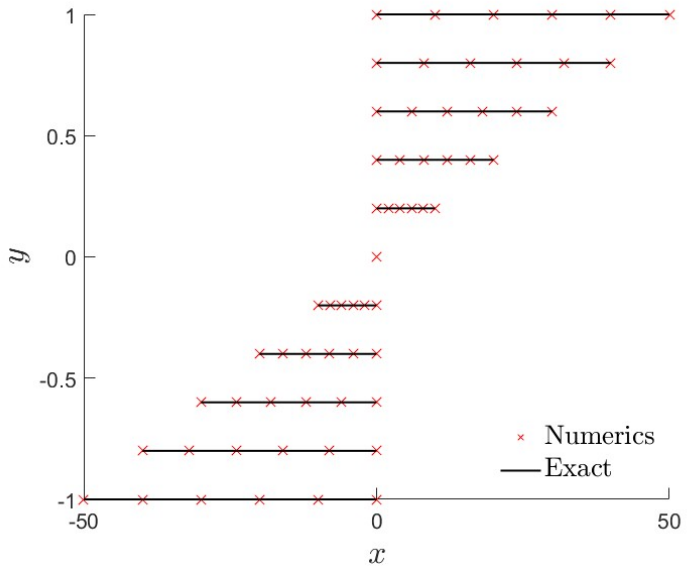


Fig. 3.3 Trajectories comparison of exact and numerical solution in a shear flow configuration. A time step $\Delta t = 0.01$ s is used.

Taking a sheet initially in the x=0 plane, we can approximate it with N diffuselets of initial conditions $x_0^i = (0, y_0^i, 0)$ with initial orientation $\mathbf{n}_0^i = (1, 0, 0)$.

The trajectory of the diffuselet are trivially found to be

$$\mathbf{x}_i(t) = \begin{pmatrix} y_0^i t \\ y_0^i \\ 0 \end{pmatrix}. \tag{3.11}$$

This gives the first validation for the solver in the trajectories as in Figure 3.3.

We can then move on to the calculation of surface dispersion tensor which is calculated analytically as follows

$$\boldsymbol{\mathcal{L}}_i(t) = \boldsymbol{\mathcal{L}}_i(0) e^{\int_0^t (-\underline{\underline{\nabla \mathbf{u}}}^T) dt'} = \exp\left[\begin{pmatrix} 0 & 0 & 0 \\ -t & 0 & 0 \\ 0 & 0 & 0 \end{pmatrix}\right] = \mathbb{1} + \begin{pmatrix} 0 & 0 & 0 \\ -t & 0 & 0 \\ 0 & 0 & 0 \end{pmatrix}, \tag{3.12}$$

with which it is possible to calculate the Ranz time tensor

$$\boldsymbol{\mathcal{T}}_i = \mathbb{1} + \frac{4D}{(s_0^i)^2} \int_0^t \left(\boldsymbol{\mathcal{L}}_i^T \boldsymbol{\mathcal{L}}_i\right)(t') dt' = \mathbb{1} + \frac{4D}{(s_0^i)^2} \begin{pmatrix} t + t^3/3 & -t^2/2 & 0 \\ -t^2/2 & t & 0 \\ 0 & 0 & t \end{pmatrix}. \tag{3.13}$$

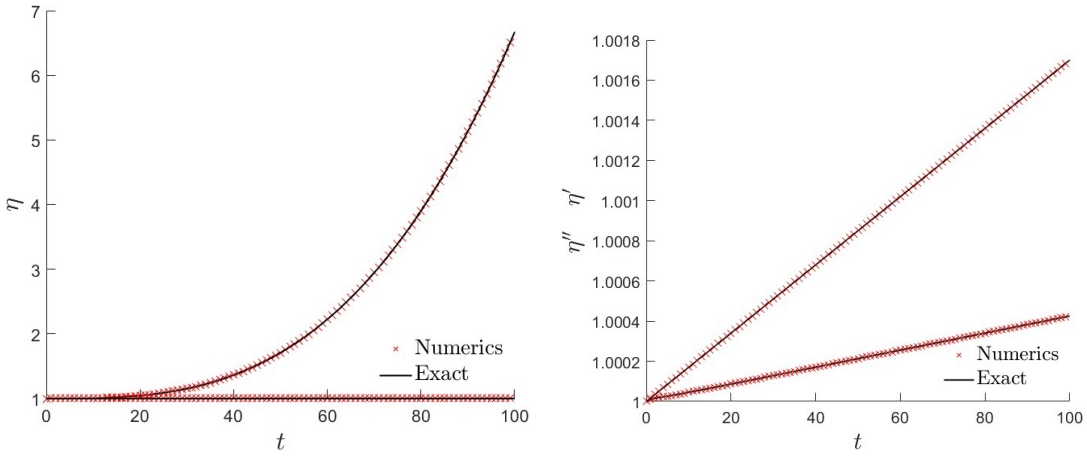


Fig. 3.4 Comparison of Ranz time eigenvalues between the exact and numerical solution in the shear flow configuration. The parameter used here are $s_0 = 1$ cm, $\delta A_0 = 1$ cm^2 and $D = 4.25 * 10^{-6}$ cm^2/s, typical values for fluorescein in water. Plot of the major eigenvalue η on the left and the minor eigenvalues η' and η'' on the right. A time step $\Delta t = 0.01$ s is used.

Calculating the eigenvalues

$$\begin{cases} \eta = 1 + \frac{2Dt}{3(s_0^i)^2}\left[(6+t^2) + t\sqrt{9+t^2}\right] \\ \eta' = 1 + \frac{4Dt}{(s_0^i)^2} \\ \eta'' = 1 + \frac{2Dt}{3(s_0^i)^2}\left[(6+t^2) - t\sqrt{9+t^2}\right] \end{cases} \tag{3.14}$$

we can use it to validate the calculation of the two previous tensors as shown in Figure 3.4. We then validated the code in the simple case of a shear flow.

In order to see its stability in the case of exponential values, we move on to the case of a stagnation point. We define the flow as compressing $-\gamma$ on the x axis and stretching γ in the y axis that translate in the definition

$$\mathbf{u} = \gamma \begin{pmatrix} -x \\ y \\ 0 \end{pmatrix}, \tag{3.15}$$

with a velocity gradient tensor

$$-\underline{\underline{\nabla \mathbf{u}}}^T = \begin{pmatrix} \gamma & 0 & 0 \\ 0 & -\gamma & 0 \\ 0 & 0 & 0 \end{pmatrix}. \tag{3.16}$$

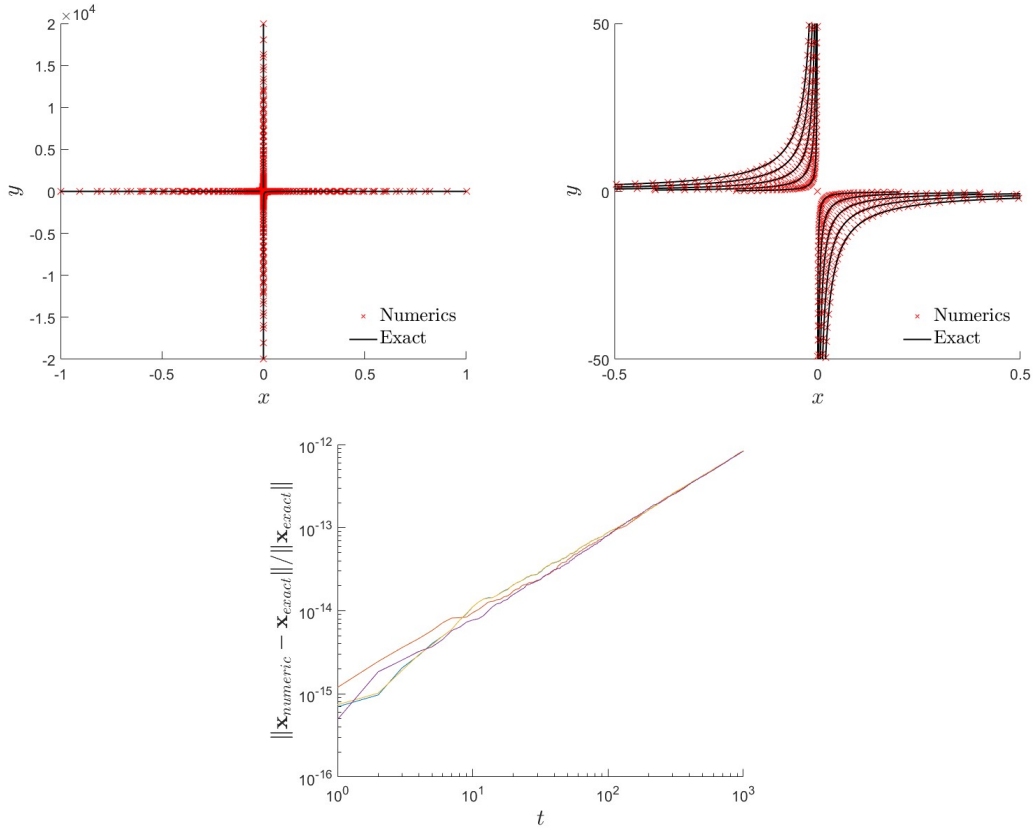


Fig. 3.5 Trajectories comparison for the stagnation point, of magnitude $\gamma = 0.1$ s^{-1}, between exact and numeric solution on the top (The two plots show the same simulation with a zoom to show the pattern near the stagnation point on the right). On the bottom, relative error calculated using the norm distance of exact and numeric solution versus time for the different diffuselets. A time step $\Delta t = 0.01$ s is used.

In this case we take a sheet in the plan $y_0 = -x_0$ to explore both compression and stretching. In this case the trajectories are

$$\mathbf{x}_i(t) = \begin{pmatrix} x_0^i e^{-\gamma t} \\ y_0^i e^{\gamma t} \\ 0 \end{pmatrix}, \tag{3.17}$$

as shown in Figure 3.5, as long as the position vector remains within the specified precision, the code does not experience error blow-up.

As before we continue the calculation by first the surface stretching tensor

$$\boldsymbol{\mathcal{L}}_i(t) = \boldsymbol{\mathcal{L}}_i(0) e^{\int_0^t (-\underline{\underline{\nabla \mathbf{u}}}^T) dt'} = \exp\left[\begin{pmatrix} \gamma t & 0 & 0 \\ 0 & -\gamma t & 0 \\ 0 & 0 & 0 \end{pmatrix}\right] = \begin{pmatrix} e^{\gamma t} & 0 & 0 \\ 0 & e^{-\gamma t} & 0 \\ 0 & 0 & 1 \end{pmatrix}, \tag{3.18}$$

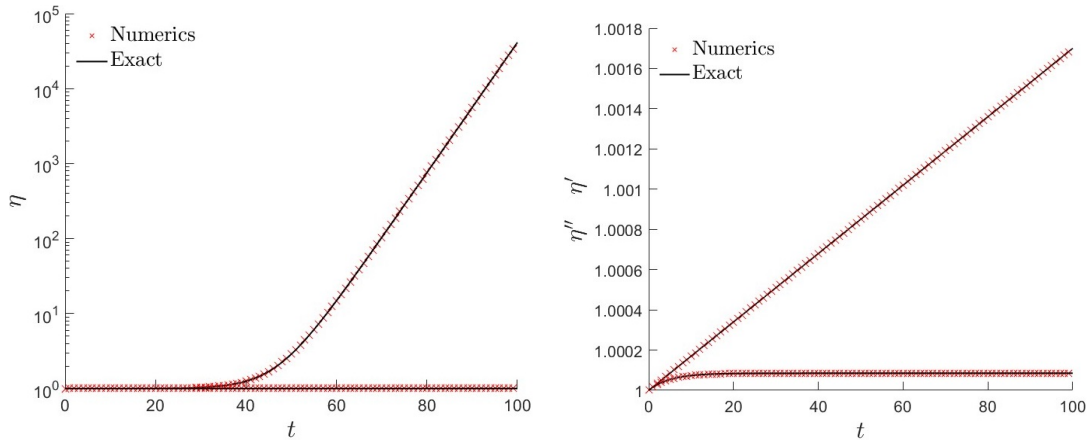


Fig. 3.6 Comparison of Ranz time eigenvalues between the exact and numerical solution in the stagnation point configuration with magnitude $\gamma = 0.1$ s$^{-}1$. The parameter used here are $s_0 = 1$ cm, $\delta A_0 = 1$ cm^2 and $D = 4.25 * 10^{-6}$ cm^2/s, typical values for fluorescein in water. Plot of the major eigenvalue η on the left and the minor eigenvalues η' and η'' on the right. A time step $\Delta t = 0.01$ s is used.

leading to a Ranz time tensor

$$\boldsymbol{\mathcal{T}}_i = \mathbb{1} + \frac{4D}{(s_0^i)^2}\int_0^t \left(\boldsymbol{\mathcal{L}}_i^T \boldsymbol{\mathcal{L}}_i\right)(t')dt' = \mathbb{1} + \frac{4D}{(s_0^i)^2}\begin{pmatrix} (e^{2t}-1)/2 & 0 & 0 \\ 0 & (e^{-2t}-1)/2 & 0 \\ 0 & 0 & t \end{pmatrix}. \quad (3.19)$$

The last step is to calculate the eigenvalues to verify the code, which in this case are:

$$\begin{cases} \eta = 1 + \frac{2D}{s_0^2}(e^{2t}-1) \\ \eta' = 1 + \frac{2Dt}{s_0^2} \\ \eta'' = 1 - \frac{2D}{s_0^2}(e^{-2t}-1) \end{cases}. \quad (3.20)$$

The comparison is plotted in Figure 3.6, showing that the code is stable on the eigenvalues calculation as long as the numbers are in the range of precision.

3.4 Convergence Study of the code for the Soft Mixer

The code described in the previous section was used to study the mixing characteristics of the soft-mixer, in the case of cylindrical geometry. In particular, as we shall see in the next chapter, the results obtained were compared with experiments. In this section we focus on the study of the convergence of the code with the flow used for the comparison.

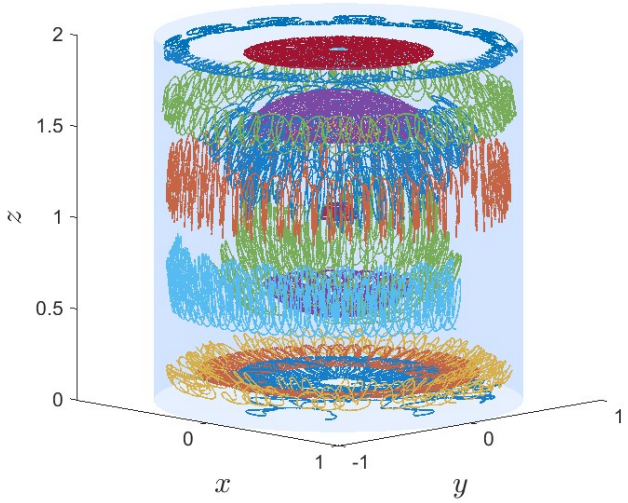


Fig. 3.7 Sample of the trajectories in the model used for the convergence test. This plot shows $N = 15$ particles, running for a dimensionless time $T = 100$.

As described in the introduction, the theoretically expected motions are described by the forced resonant mode, the geostrophic mode and the modes generated by triadic instability. The comparison showed that the model that best describes the experimental flow contains more motions than expected. A simpler model with larger amplitudes than those observed was chosen for convergence in order to have a test with a more energetic flow as the upper extreme of the simulations performed.

The flow used in the convergence test is defined as follows:

$$\mathbf{u} = \mathrm{Re}\left[A_1 \begin{pmatrix} u_1(r)\cos(k_1 z) \\ v_1(r)\cos(k_1 z) \\ w_1(r)\sin(k_1 z) \end{pmatrix} e^{i(\theta+t)} + A_5 \begin{pmatrix} u_5(r)\cos(k_1 z) \\ v_5(r)\cos(k_1 z) \\ w_5(r)\sin(k_1 z) \end{pmatrix} e^{i(5\theta+\varpi_5 t)}\right], \tag{3.21}$$

where the amplitudes were fixed at $A_1 = 0.2$ and $A_5 = 0.03$ and the axial wavenumber $k_1 = 1.579$ is the value for the first resonance of the forced mode. The frequency of the fifth mode $\varpi_5 = -0.341$ is found from the dispersion relation (1.28) combined with the definition of the radial wavenumber defined in (1.26). The axial wavenumber is fixed at $k_5 = k_1$ as in the triadic resonant condition, that gives also the choice of negative frequency. The radial flow $\mathbf{u}_1$ is defined in equation (1.32) and $\mathbf{u}_5$ is defined in equation (1.27) for the parameter described above (explicitly the radial wavenumber has the value $\lambda_5 = 9.116$).

The first test performed concerns the calculation of trajectories in this flow. A sample of the trajectories of the particles in this flow is given in Figure 3.7. From these trajectories, it was possible to observe that the particles do not escape the cylinder whenever the chosen time step is small enough so that the displacements of the particles at the edge of the cylinder is never outside it. In various tests it has been observed

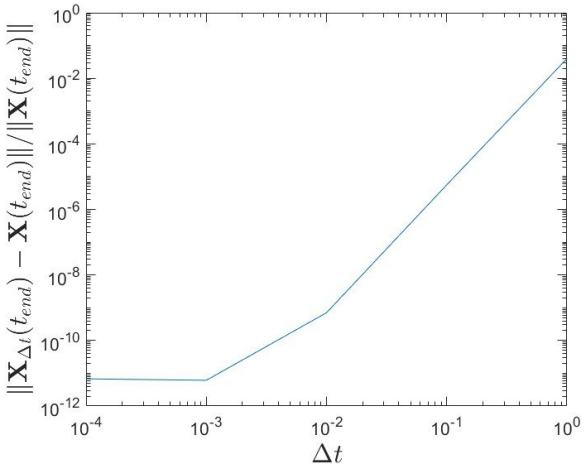


Fig. 3.8 Convergence of the position for $N = 1$ varying Δt, using the last position of the particle at $t_{\text{end}} = 1000$.

empirically that for a time step $\Delta t \lesssim 0.1$ this condition is fulfilled, avoiding the use of additional numerical boundary conditions.

Since the trajectories are regular within the entire domain, a random particle was taken for the convergence test. So fixing the initial conditions, we varied the time step Δt from 1 to 10^{-5} in the simulations up to the final time $t_{\text{end}} = 1000$. The trajectory for $\Delta t = 10^{-5}$ is considered to be the exact solution as it is highly converged. The relative error of the final position of the various trajectories with respect to the exact one was used as a measure of convergence, defined as $\|\mathbf{x}_{\Delta t}(t_{\text{end}}) - \mathbf{x}(t_{\text{end}})\|/\|\mathbf{x}(t_{\text{end}})\|$, with with $x(t_{end})$ the value for the smallest Δt.

The results are shown in Figure 3.8. The error on the trajectories is found to scale as Δt^4, with an error less then 1% for a $\Delta t \lesssim 0.1$.

To check the convergence of the tensors $\boldsymbol{\mathcal{L}}_i$ and $\boldsymbol{\mathcal{T}}_i$ we used the same approach as for the trajectories. We then considered the maximum eigenvalues μ and η on a single particle at time $t_{\text{end}} = 1000$ varying Δt, again defining the relative errors with respect to the solution at $\Delta t = 10^{-5}$. The results shown in Figure 3.9. The error scales as Δt^2 in both cases where the upper bound is given by the convergence of μ that has an error less than 1% for a $\Delta t \lesssim \times 10^{-2}$. The error does not scale as δt^4 although the numerical scheme looks like fourth-order Runge-Kutta scheme. Indeed, the gradient of velocity is not calculated at mid step as it should be done in a real Runge-Kutta scheme.

Finally, the observable used to fix the time step and the number of particles is the variance of the scalar field. Fixing a final time $t_{\text{end}} = 500$ to avoid the variance to become smaller than the precision, we did two different tests.

First fixing $N = 1$ and varying Δt we did the same test as before calculating the relative error of the final value with respect to the solution at $\Delta t = 10^{-5}$. The second test concerns the scaling of the variance with the number of particles N at the same final time $t_{\text{end}} = 500$, calculating the relative error with respect to the solution for $N = 1000$.

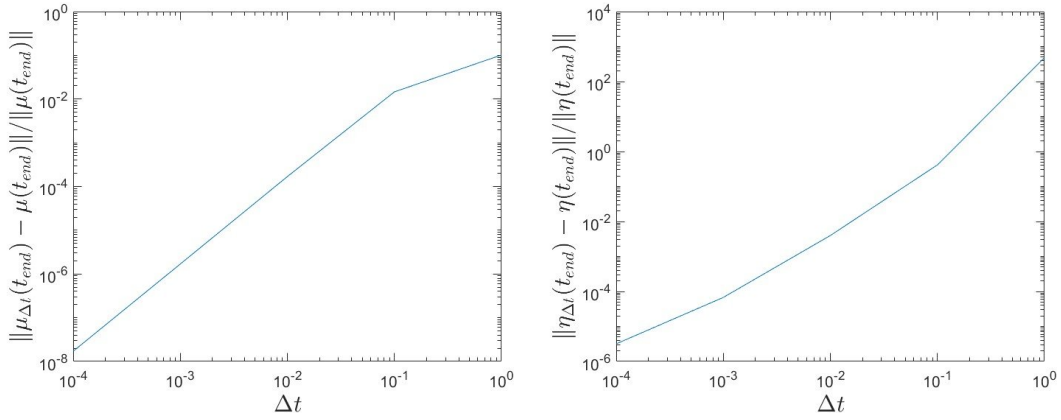


Fig. 3.9 Convergence of the larger eigenvalue of the tensor $\mathcal{L}$ (a) and $\mathcal{T}$ (b) for $N = 1$ varying Δt at the final time $t_{\text{end}} = 1000$.

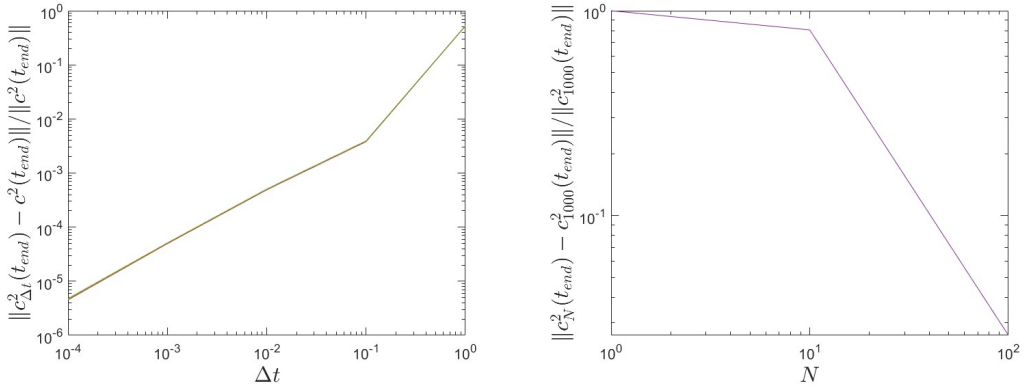


Fig. 3.10 Convergence of the variance at $t_{\text{end}} = 500$ for $D = 4.25 \times 10^{-6}/\Omega$ cm^2, varying the parameter $s_0 = 0.5, 0.1, 0.05, 0.01, 0.005, 0.001$ cm and $\Omega = 0.1, 20$ rad/s for $N = 1$ (a) and varying N for $\Delta t = 0.01$, $s_0 = 0.001$ cm and $\Omega = 20$ rad/s (b).

The results in Figure 3.10 again show a scaling with respect to the time step as Δt^1 with a relative error of 0.05% for $\Delta t = 10^{-2}$, in the bounds found previously. Thus, the time step is fixed at $\Delta t = 10^{-2}$ for all simulations performed. Furthermore, to confirm the calculation of the variance, the parameters s_0 and D (which varies as time is dimensionalised via Ω) were varied, resulting in no change in the error values as expected. Concerning the number of particles we observed that the error is of the order of a few percents for N=100 particles. Thus $N = 100$ was adopted in the simulations to avoid a huge increase in the calculation time, with the observation that over long times, the effect is balanced by the exploration of the ergodicity of the flow.

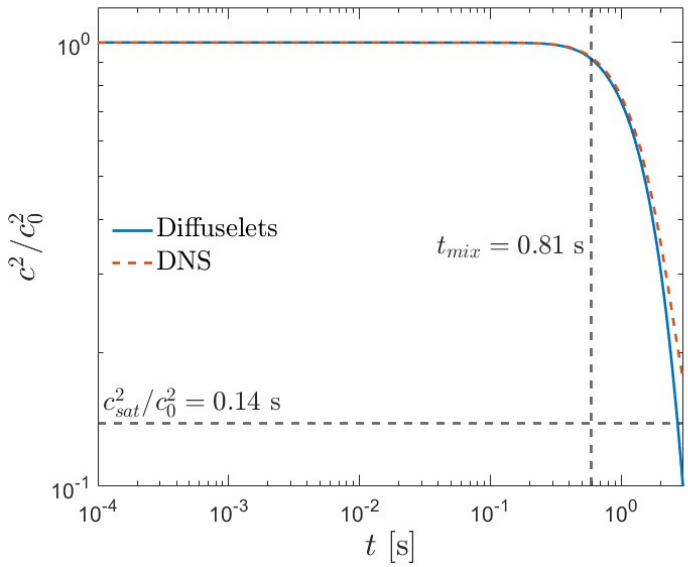


Fig. 3.11 Evolution of the variance comparison between Diffuselet and DNS in a 3D homogeneous isotropic turbulence at $Sc = 70$.

3.5 Results in Turbulent DNS

In collaboration with the Fluid Mechanics Group research at TU Ilmenau, in particular the PhD student Vladyslav Pushenko, the diffuslet method was applied to a homogeneous isotropic turbulence in a statistically steady state flow.

Then the algorithm described above was included and validated in the DNS workflow simulating the flow. The logic followed is therefore to take the flow $\mathbf{u}$, the velocity gradient tensor $\underline{\underline{\nabla \mathbf{u}}}$ and the surface dispersion tensor $\boldsymbol{\mathcal{L}}_i$ as input for the calculation of $\boldsymbol{\mathcal{T}}_i$, the concentration variance and the PDF evolution.

Furthermore, DNS has the possibility of calculating the evolution of a scalar liability within the flow, with the limitations described above. This gave the possibility of comparing the Diffuselet method with a DNS at a moderate Schmidt number, $Sc = 70$, such that the possibilities of the DNS were not exceeded while remaining at a value large enough for the assumptions of the Diffuselet method.

We present here an example of the results for the comparison between the Diffuselet method and DNS. The simulation is in a cubic domain with periodic boundary condition of volume $V = L^3$, with L=25.6 cm, equipped with a homogeneous cubic mesh of size $\Delta x = 1.25^{-2}$ cm so $L = 2048\Delta x$. The flow is determined by the parameters $Re = 1634$ with mean kinetic energy dissipation rate $\langle \epsilon \rangle = 33$ cm^2/s^2, defined by the kinetic energy dissipation rate field $\epsilon(\mathbf{x}, t) = \nu/2 \left(\underline{\underline{\nabla \mathbf{u}}} + \underline{\underline{\nabla \mathbf{u}}}^T \right)^2$. The Kolmogorov scale of the flow $\eta_K = \nu^{3/4}/\langle \epsilon \rangle = 0.1$ cm$:= 8\Delta x$, for $\nu = 1.5 \times 10^{-1}$ cm^2/s valid for simulation in air at temperature around $T = 20°$, that gives also an average stretching rate $\gamma = \sqrt{\langle \epsilon \rangle / (2\nu)} = 10.5$ s^{-1}.

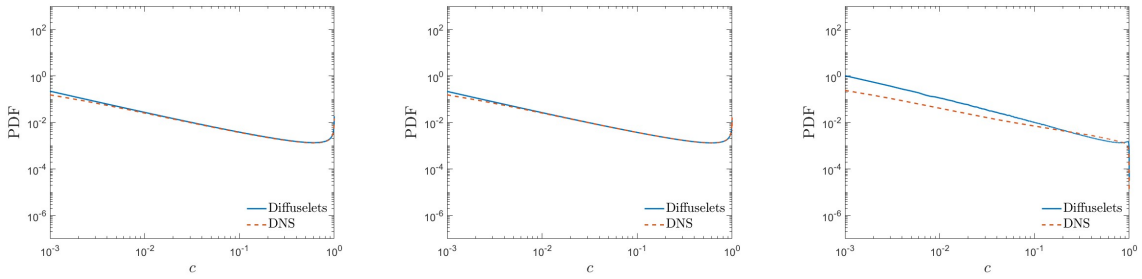


Fig. 3.12 PDF evolution comparison between Diffuselet and DNS in a 3D homogeneous isotropic turbulence at $Sc = 70$. From left to right the plots are taken at simulation times $t = 0$ s, $t = 0.2$ s and $t = 1$ s.

With regard to the scalar field, the example under consideration presents a number $Sc = 70$, a number in which the convergence of the Diffuselet method is at its limit, showing the limit of validity of the model. Specifically, an initial condition of the scalar field distributed over a flat sheet of size $s_0 = 80\Delta x = 1$ cm was considered with an initial Gaussian transversal profile of standard deviation $\sigma = s_0/2$ centered on the sheet. In this configuration the mixing time is given by $t_{\text{mix}} = 1/\gamma \log(\gamma s_0^2/D) = 0.81$ s, where we have used the value of the diffusivity coefficient $D = \nu/Sc \approx 2.14 \times 10^{-3}$ cm^2/s.

The diffuselets were then placed in this plane, homogeneously on the simulation lattice every 8 nodes resulting in a number of them $N = 256^2$, with the initial striation thickness equivalent to that of the concentration $s_0 = 80\Delta x$ and an initial surface area $\delta A_0 = 4^{-2}$ cm^2.

The comparison of the field variance between Diffuselet and DNS is shown in Figure 3.11. From this plot we can see that the mixing time is equivalent in the two cases, with good agreement of the theoretical value discussed above. Furthermore, we observe that the evolution for $t > t_{\text{mix}}$ of the variances deviates slightly. This trend is not surprising since the Diffuselet method is derived under the assumption of infinite volume such that the mean value is zero and the variance tends to 0 for long times. In the DNS, the variance saturates at a value $c_{sat}^2/c_0^2 = 2\sqrt{\pi}s_0/L$. However, despite this detail the decay of the variances is comparable over one decade.

Turning to the evolution of the PDF, shown in Figure 3.12, we again observe a deviation in the evolution for times $t > t_{\text{mix}}$ which we can again attribute to the observations for the decay of the variance, i.e. a different treatment of the mean and the definition of the background. The aggregation of neighboring sheets also modifies the PDF in the DNS, although this effect is not taken into account with the Diffuselet Method. However, this again shows that it is possible to have a good approximation of the field with a much simpler numerical calculation. This Diffuselet Method can also be used for larger Schmidt number, which would not be possible with a DNS method.

This work is still in progress by Vladyslav Pushenko and will be published soon, as well as included in his doctoral thesis.

Chapter 4

Diffuselet Method in the rotating tilted Cylinder

In this chapter, we describe the results found with the Diffuselet method in the flow generated by the soft mixer in the cylindrical configuration. This work was carried out by performing PIV experiments to measure the flow in the cylinder, which is used in the calculation of the evolution of diffuselets. In addition, mixing experiments were carried out to measure the evolution of the concentration of a dye introduced in the rotating flow. Finally, the results of the experiments and Diffuselet are compared, showing good agreement of the observations, even though a theoretical model of the velocity field was used without performing a DNS of the flow.

4.1 Description of the flow

The flow inside a rotating tilted cylinder has been extensively described in Section 1.2. In this section we will use this theory to fit the flow measured by PIV experiments. We start with the description of the parameter space used in the experiments.

4.1.1 Non-dimensional parameters

The system is characterized by 4 non-dimensional parameters:

- **The non-dimensional height** $h = H/R$ is the parameter that can be tuned to select the different resonances of the flow. In the experiment, we consider values $h = 2$ to excite the first resonance.
- **The tilt angle** α is the parameter describing the intensity of the forcing applied by the free surface. In the experiment, we consider values $1^\circ \leq \alpha \leq 10^\circ$.
- **The Ekman number** In the experiment, it is varied from $E \approx 10^{-4}$ to $E \approx 10^{-3}$;
- **The Froude number** This parameter is chosen to be small ($Fr \lesssim 10^{-1}$) to neglect the curvature of the free surface in the theory;

– **The Schmidt number** In the experiment, where we used rhodamine B, we have a value of $Sc = 2.3 \times 10^3$ such that the dye streaks are much thinner than the coherent structures of the flow.

4.1.2 Fitting model

The fitting model for experiments uses the basis of Kelvin modes derived in the theory, since they have been observed close to threshold. We need to make assumptions about the basis used since the experimental data are not given for the whole volume, instead, they are obtained from measurements taken in 2D horizontal sections of the flow. We need to find a way to reconstruct the 3D flow and we will use a subset of Kelvin modes.

Decomposing the flow in Kelvin modes with m as azimuthal wavenumber and k as axial wavenumber the model is given by

$$\mathbf{u}_f = \sum_{m=1}^{\infty}\sum_{j=1}^{\infty} \mathrm{Re}\left[A_m^j \begin{pmatrix} u_m^j(r)\cos(k_m z) \\ v_m^j(r)\cos(k_m z) \\ w_m^j(r)\sin(k_m z) \end{pmatrix} e^{i(m\theta+\varpi_m^j t)}\right], \tag{4.1}$$

which respects $w = 0$ at $z = 0$.

We have used a single axial wavenumber k_m for each azimuthal wavenumber instead of taking an infinite number of axial wavenumbers.

The assumptions about the wavenumbers are as follows:

- The axial wavenumbers k_m have been defined by assuming that the modes are obtained by a cascade of triadic resonances that respect the resonance condition (1.80). By fixing the wavenumbers of the forced mode at the first resonance $k_1 = \pi/h$, because we are at the resonance of the forced Kelvin mode, and assuming that the triad start at $m \geq 3$ we have

$$k_m = \begin{cases} \pi/h & \text{if} \quad m = 2l+1,\ l \geq 1 \\ 2\pi/h & \text{if} \quad m = 2l,\ l \geq 2 \end{cases}. \tag{4.2}$$

  In these assumptions, the modes $m = 2$ were not included because they cannot couple to form a triad. Therefore it was assumed $k_2 = \pi/h$ as the forced mode. In the following the notation for axial wavenumbers is simplified to k_m since in these assumptions there is no dependence on j.

- The frequencies ϖ_m^j of the modes follow from the dispersion relation (1.28) and the definition of the radial wavenumbers as in equation (1.26). They are the solutions of the equation:

$$mJ_m\left(k_m\sqrt{\frac{4}{\varpi_m^2}-1}\right) + k_m\sqrt{\frac{2+\varpi_m}{2-\varpi_m}}J_{m-1}\left(k_m\sqrt{\frac{4}{\varpi_m^2}-1}\right) = 0. \tag{4.3}$$

There is an infinity of solutions defined by the index j, for each azimuthal wavenumber m.

We emphasize that once wavenumbers and frequencies are fixed, the flow is defined and the radial functions are given by the formula (1.27).

4.1.3 Geostrophic flow

In the cylinder there is also another main component in the flow and this is the geostrophic flow. The geostrophic flow, as introduced in section 1.2.3, is solution of the equation (1.14) that has a general solution

$$\mathbf{u}_0 = A_0 \begin{pmatrix} 0 \\ v_0(r) \\ 0 \end{pmatrix}, \tag{4.4}$$

where $v_0(r)$ can be any function satisfying $v_0(0) = 0$.

The fitting model adopted here is

$$\mathbf{u}_0(r) = \sum_{j=1}^{\infty} A_0^j \begin{pmatrix} 0 \\ -J_1(d_j r) \\ 0 \end{pmatrix}, \tag{4.5}$$

where the minus sign was introduced because the geostrophic motion is retrograde. The radial wavenumbers are defined by the condition $v_0(r = 1) = 0$ for each mode. The first radial wavenumbers have values $d_1 = 3.83$, $d_2 = 7.016$, $d_3 = 10.1734681350627$ and so on.

4.1.4 PIV measurement of the amplitudes

The experimental setup for the PIV campaign (Figure 4.1) used a double-pulsed YAG laser (150 mJ per pulse, 532 nm) at 0.5 Hz with pulse intervals of $0.1 - 50$ ms. A 1.5 mm thick laser sheet, normal to the cylinder axis, illuminated the flow, while a stationary 4-megapixel camera below the cylinder captured synchronized images. Second-pulse images were rotated to remove solid-body rotation, enabling accurate velocity measurements and detecting vortices down to 1% of the rotation. A cross-correlation algorithm optimized for large velocity gradients processed the data (Meunier & Leweke 2003).

The mode amplitudes are determined by projecting the experimental velocity field onto the theoretical model defined by equations (4.1) and (4.5).

The flow is measured on a horizontal cross section of the cylinder at $z_{\text{laser}} = h/8$ in order to be able to measure all the modes without being at the node of a mode (remember that the modes are $\propto \cos(z\pi/h)$ or $\cos(z2\pi/h)$).

As expected from the theory the main modes observed in the cylinder are $m = 0, 1, 5$ and 6, just above the treshold of the instability. An example of the azimuthal Fourier

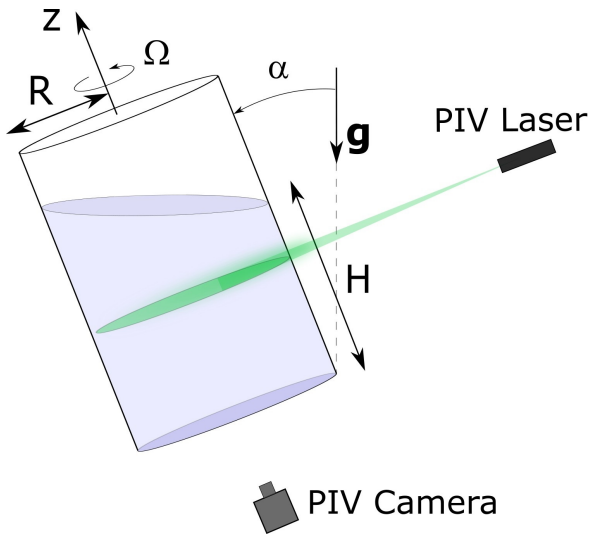


Fig. 4.1 Experimental set-up for the PIV measurements.

decomposition of the experimental flow is shown in Figure 4.2. For this Ekman number, we are able to see three different Kelvin modes.

As shown in Figure 4.3, the amplitudes depend on the Ekman number. In the stable regime at high E (Figure 4.3 (a)) the flow is mainly driven by the forced mode and the geostrophic flow. The amplitude of modes 5 and 6 is smaller than 10^{-3}, and only due to noise in the measurements.

When the E is smaller than the critical value of the triadic instability the forced mode quickly reaches a saturation value. Then the instability is triggered and the amplitudes of mode $m = 5$ and 6 start to grow, in a transient regime. They reach a weakly oscillatory regime with a maximal amplitude around 10^{-3} (Figure 4.3 (b)). When the $E \lesssim 10^{-4}$ the number of unstable modes increases, with most of the modes $m \leq 10$ starting to have an amplitude comparable with the modes $m = 5$ and 6, until it reaches the turbulent regime (Figure 4.3 (c)).

Increasing α we are able to increase the amplitude of the forced mode (see equation (1.63)), changing the critical E for the different regimes we discussed before. However the behavior of the modes follow the same trend for $\alpha \leq 10°$ (see Figure 4.4). For $\alpha = 1°$ and $3°$ the theory predicts correctly the critical E of onset of the triadic instability. For the case $\alpha = 10°$ the experiment is surprisingly more stable than the theory.

Finally, we have measured the azimuthal spectrum of the flow in the experiments to appreciate the behavior of the various modes (Figure 4.5).

The spectrum is defined from the azimuthal transform of the axial vorticity

$$\hat{\zeta}^m(r,t) = \frac{1}{2\pi}\int_0^{2\pi} d\theta \zeta(r,t) e^{im\theta}, \tag{4.6}$$

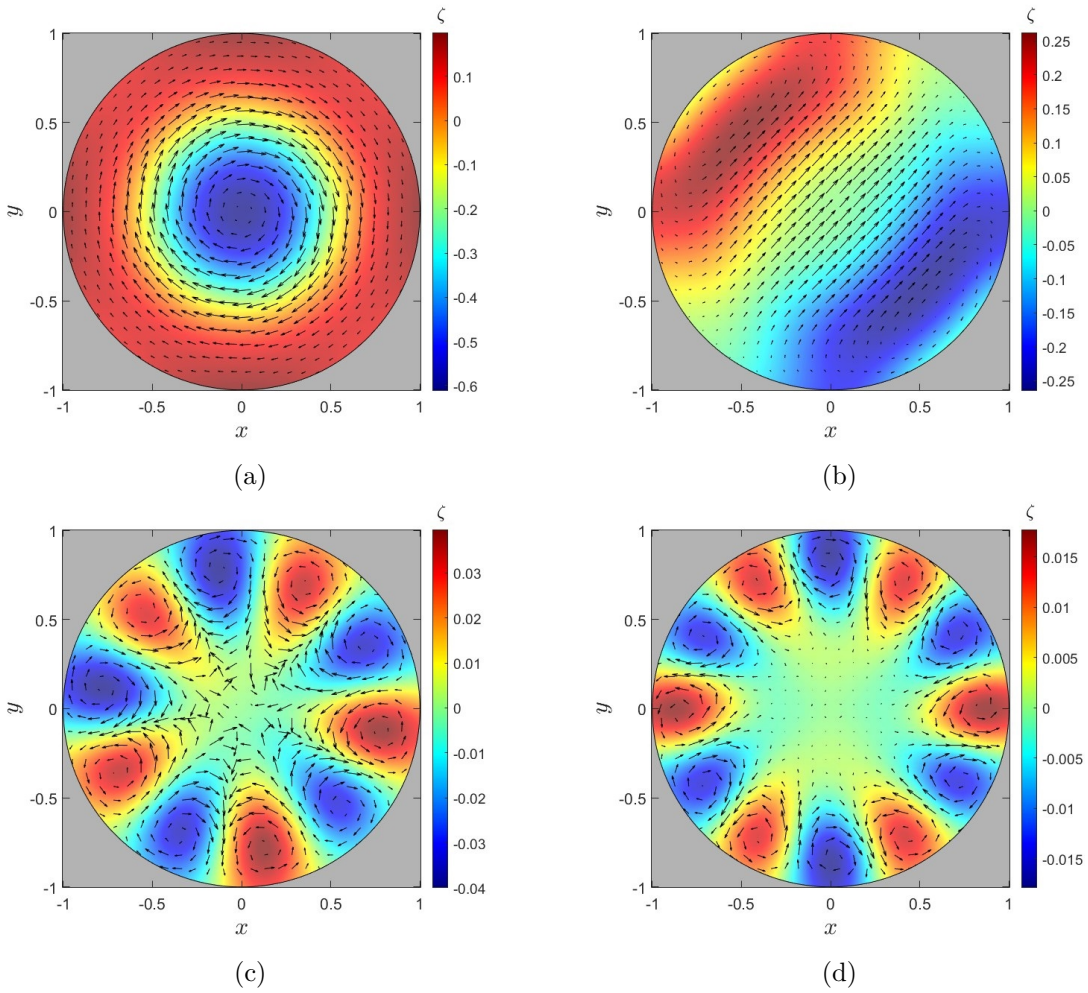


Fig. 4.2 Azimuthal Fourier decomposition of the flow (Vorticity+Velocity) measured at $z_{\text{laser}} = 0.25$ for $\alpha = 3°$ and $E = 2 \times 10^{-4}$ in the same fame. In order we have the component $m = 0, 1, 5$ and 6.

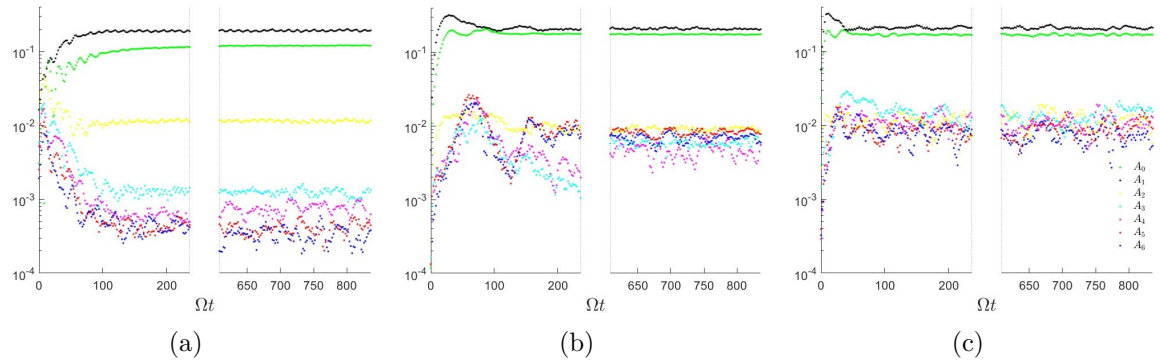
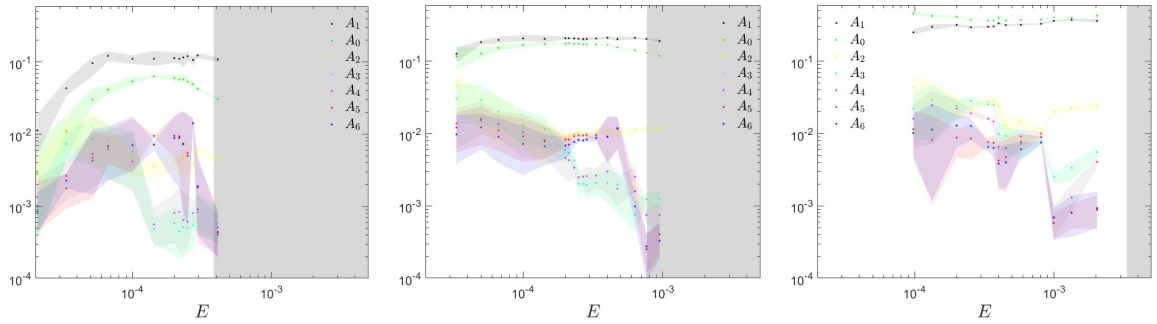
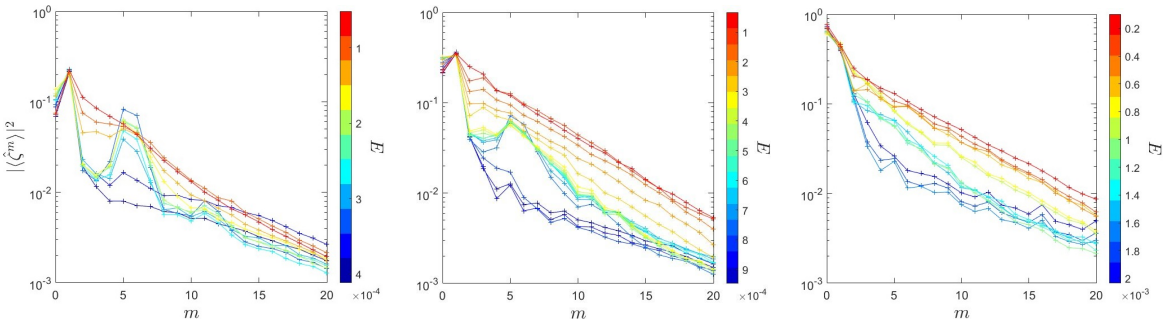


Fig. 4.3 Experimental amplitudes measured at $z_{\text{laser}} = 0.25$ for $\alpha = 3°$ and $E = 10^{-3}, 2 \times 10^{-4}, 10^{-4}$. The measurements are taken at a frequency of 0.5 Hz at the beginning of the experiment and after 10 minutes to measure the transient and the permanent regime of the instability.



(a) (b) (c)

Fig. 4.4 Experimental amplitudes measured at $z_{\text{laser}} = 1.15$ cm for $\alpha = 1°$ (a), $\alpha = 3°$ (b) and $\alpha = 10°$ (c) as E varies. The gray area delineates the region of stability.



(a) (b) (c)

Fig. 4.5 Azimuthal spectrum of the flow $|\langle\hat{\zeta}^m\rangle|^2$ (see equation (4.7)) in the range of E used in the experiments.

of the various experimentally measured frames. Therefore, taking the stationary regime of motion, a time and space average of the transform defined above was taken

$$\langle\hat{\zeta}^m\rangle = \frac{1}{\Delta t}\int_0^{\Delta t}\left(\int_0^1 \hat{\zeta}^m(r,t)dr\right)dt, \tag{4.7}$$

where Δt is the time window of the long time experiment. So the spectrum is defined as the square modulus of the average just defined $|\langle\hat{\zeta}^m\rangle|^2$.

From these plots, we can see that the model of the triadic instability works well in the hypothesis taken of small forcing ($\alpha \lesssim 10°$) with a sudden appearance of modes 5 and 6 at the critical Ekman number. In addition, it can be seen that the increase in forcing changes the stability of the various triads resulting in a continuous spectrum. This is visible, especially for $\alpha = 10°$ where the effect is more pronounced, resulting in a smaller peak of the most unstable triad that is less predominant than the others with a greater equalization of energy.

4.2 The Diffuselet method

The PIV measurements showed that a basis that well approximates the flow in the parameter space considered is given by the superposition of azimuthal wavenumbers $m \leq 8$, for which we took the first five resonances $j \leq 5$.

Being interested in the study of mixing in the stationary regime, the amplitudes are chosen as the mean value of the measurements at late time to avoid influence from the experimental noise. We did a test with different simulations showing that taking stationary amplitudes instead true time dependent amplitudes does not change too much the mixing time and the variance decay behavior but it increases the efficiency of the code.

The first observations of the results generated by this flow concern the trajectories of the particles in the frame rotating with the cylinder. The trajectories generated by Kelvin modes at small forcing have a pattern similar to that of a Stokes drift in which particles have drifted in the azimuthal direction while having an oscillation around shells that fits the cylindrical geometry.

Examples of these trajectories are shown in Figure 4.6. It shows how this pattern evolves as the E decreases, i.e., as the value of the amplitudes increases. We can see that the trajectories lose regularity as the amplitudes increase leading to chaos.

To observe this phenomenon in a clearer way, we chose to define a Poincaré map so as to have a visualization of the dispersive properties of the flow. The map has been defined on a vertical plane $y = 0$ in the laboratory frame. We observe that trajectories develop on concentric shells formed by regular trajectories for large E. As E decreases, the region at the edge of the cylinder changes, showing more irregular behavior that increasingly approaches a chaotic sea.

Regarding the evolution of the variance, we now want to show the sensitivity with respect to the initial positions of the diffuselets. For this study we considered the field with experimental amplitudes measured for $\alpha = 3°$ and $E = 2 \times 10^{-4}$. Considering a set of $N = 5000$ diffuselets homogeneously distributed, on the plane $y = 0$ and $0 \leq x \leq 1$, we calculated the evolution of the variance of each diffuselet, as defined in equation (1.119). The results plotted in Figure 4.7 show a broad distribution of the stretching experienced by the diffuselets demonstrating that there is a strong dependence on the initial positions.

These results allow us to define a distribution of mixing times within this flow. We defined the mixing time as the time at which the variance decays at 9/10 of its initial value. This allows the distribution to be operationally measured from the variance values. Furthermore, since we want this distribution to be as converged as possible, this measurement was made by taking different orientations of the diffuselets. The variance was defined as a function of the orientation angles, $0 \leq \theta \leq \pi/2$ and $0 \leq \phi \leq \pi/2$ respecting the symmetries of the diffuselets, and normalized with respect to the initial value, i.e. it is defined as

$$c_i^2(\theta, \phi)/c_0^2 = \frac{1}{\sqrt{\sin^2(\theta)\left(\eta_i' \cos^2(\phi) + \eta_i'' \sin^2(\phi)\right) + \cos^2(\theta)\eta}}. \tag{4.8}$$

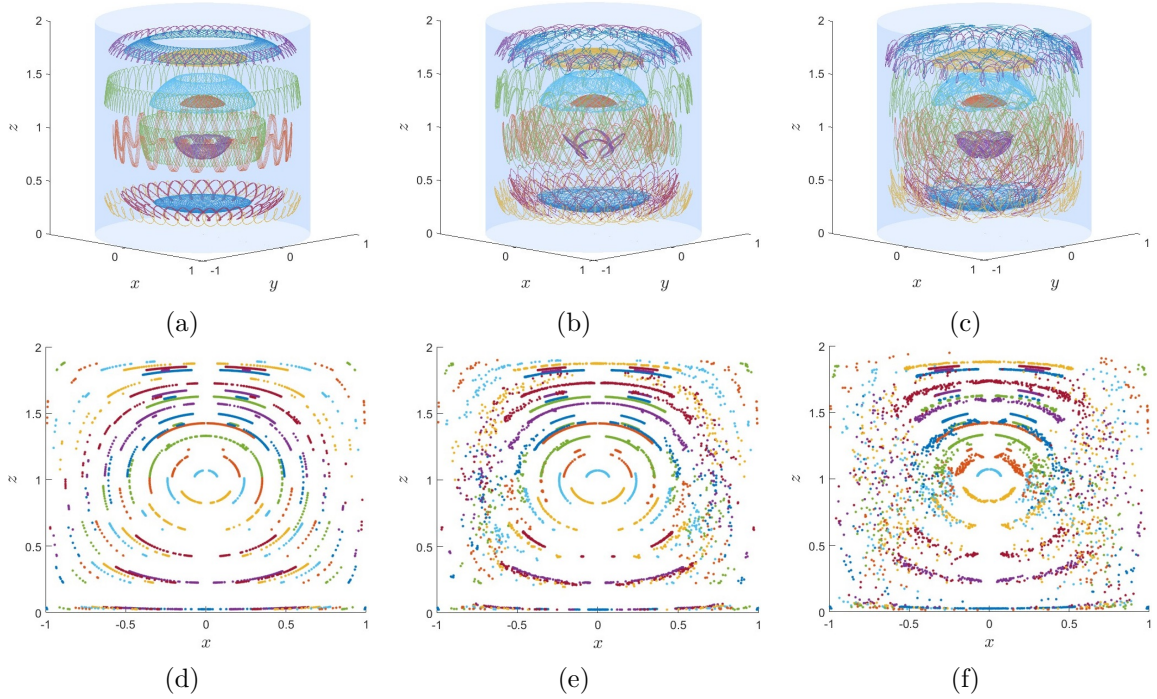


Fig. 4.6 Trajectories and Poincaré maps of 15 particles with the same initial condition in the flow with amplitudes measured for $\alpha = 3°$ and $E = 10^{-3}$ (a-d), 2×10^{-4} (b-e) and 10^{-4} (c-f) in the rotating frame of the cylinder. The Poincaré maps are defined as the crossing points on the plane $y = 0$ in the laboratory frame.

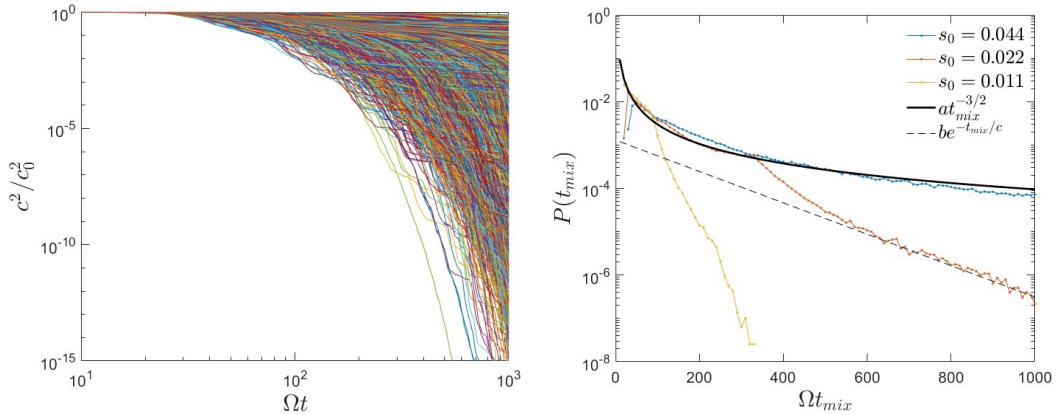


Fig. 4.7 Variance plot for each individual diffuselet in a simulation of $N = 5000$ for $s0 = 0.022$ initially positioned on a plane defined for $y = 0$ and $0 \leq x \leq 1$ advected by the flow with experimental amplitudes given by $\alpha = 3°$ and $E = 2 \times 10^{-4}$ (a). Mixing time distribution extracted from the same ensemble as the parameter $s0$ varies (b).

Indeed, the variance of each diffuselet is proportional to $V_i c_i^2$ where V_i is a diffused volume of the diffuselet and c_i its maximal concentration. However, scalar conservation gives $V_i = V_0 c_0 / c_i \sim c_i^{-1}$. The variance is thus proportional to $c_i \sim \tau_i^{-1/2} = \left((\hat{\mathbf{n}}_0^i)^T \boldsymbol{\mathcal{T}}_i \hat{\mathbf{n}}_0^i\right)$.

From this definition, we extracted the values $t_{\text{mix}}(\theta, \phi)$, and calculated the probability distribution function $P(t_{\text{mix}}, \theta, \phi)$. The distribution obtained were then averaged over the orientation as follow

$$P(t_{\text{mix}}) = \int_0^{\pi/2} d\phi \int_0^{\pi/2} \sin(\theta) d\theta P(t_{\text{mix}}, \theta, \phi), \tag{4.9}$$

an example is shown in Figure 4.7. In this plot, we can observe the dependence of the distribution on the parameter s_0. For $s_0 = 0.022$, we observe a power trend of the type $P(t_{\text{mix}}) \sim t^{-3/2}$, which transitions to an exponential law of the type $P(t_{\text{mix}}) \sim e^{-t}$ at large times. The transition occurs for smaller times when s_0 decreases. This kind of behavior may be explained by a log normal model of stretching rate resulting in a distribution of mixing time as

$$P(t_{\text{mix}}) = \gamma_p \frac{e^{-\gamma_p t_{\text{mix}}/2}}{(\gamma_p t_{\text{mix}})^{3/2}}, \tag{4.10}$$

where γ_p is the most probable stretching rate in the flow.

Let us now look at the evolution of the averaged variance of the field. The first observation focus on the effect of the diffuselet parameters, namely s_0 and δA_0. The initial area δA_0 does not influence the temporal evolution of the variance. It only affects the initial value of the variance. This is why we have normalized the variance with respect to its initial value to drop the dependency on δA_0.

In the same simulation as above, we can calculate the total variance with increased values of the parameter s_0 while keeping the same initial position of the diffuselets, as shown in Figure 4.8. Although the diffuselets have the same stretching history, the value of s_0 modifies the mixing time. That phenomenon has been described in section 1.3.1, where for a mean value of shear rate γ the mixing depends logarithmically on s_0. Here the mixing time depends on s_0, but the decay exponent at late times seems to be independent of s_0, although there are different stretching rates.

We observed that the decay of the variance depends on initial positions in the model. This is why a comparison test with experiments was carried out. The results of this test for $\alpha = 3°$ and $E = 2 \times 10^{-4}$ (see Figure 4.9) show that this dependence is less pronounced in the experiments, probably because the experimental injection introduces some perturbations that break the regular structures of the Poincaré sections and also increases the effective volume injection. In the model the injection at mid height on the axis decays very slowly due to the KAM torus observed in the Poincaré sections.

Based on this test we have then defined the simulation protocol for the initial conditions of the diffuselets by fixing a spherical blob of comparable size with the volume injected in the experiments (the experiments were carried out by injecting 10

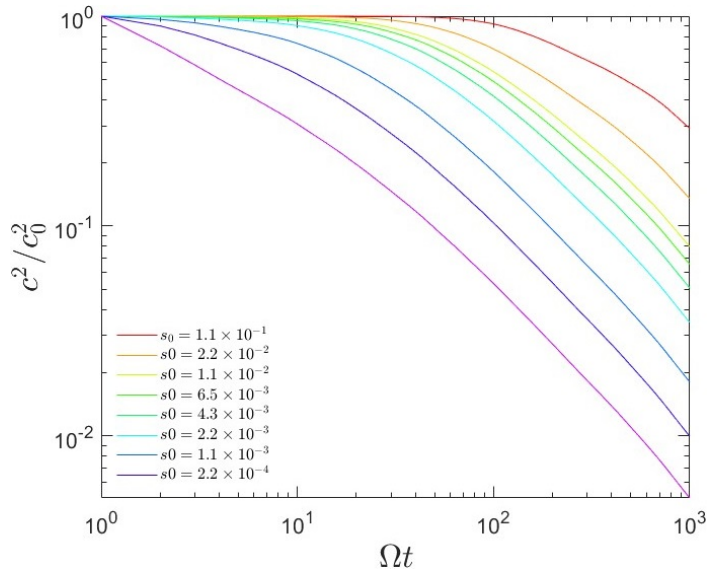


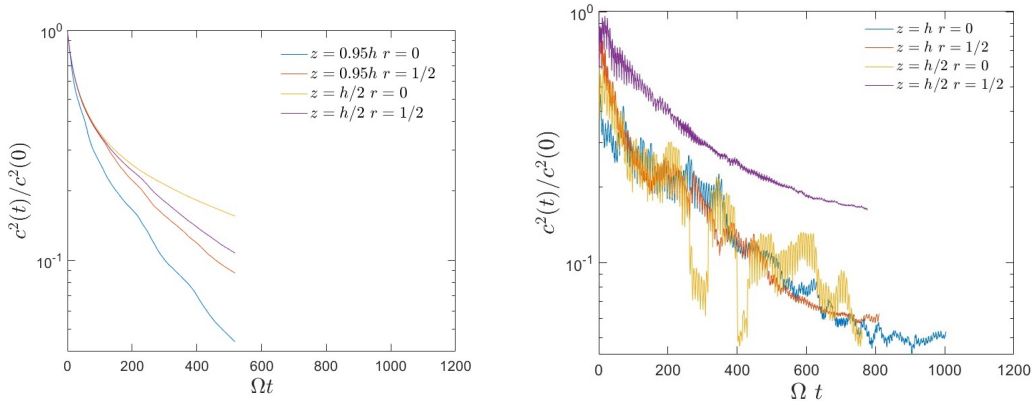
Fig. 4.8 Variance for $N = 5000$ diffuselets initially positioned on a plane defined for $y = 0$ and $0 \leq x \leq 1$ advected by the flow with experimental amplitudes given by $\alpha = 3°$ and $E = 2 \times 10^{-4}$.

ml of dye through a pipette at a fixed controlled position with an error of about half a cm) of radius $R_0 = 0.07$ and fixing $s_0 = 0.022$ compatible with the structures observed in the experiments. After multiple trials, we selected a sphere centered at $z = 0.65h$ and $r = 0$.

4.3 Comparison with experiment

Before moving on to the comparison between the diffuselet method and experiments, let us briefly describe the experimental procedure adopted. The following experimental data were partly taken from the previous work (Meunier 2020) and also from new experimental data used in the PDF study and in the change of position of the injection used in the previous paragraph. The experimental set-up used is equivalent to that of the work cited above and the one described in section 2.2.3. An example of the experiment is shown in Figure 4.10.

To fix the initial position of the diffuselets, we focused on experiments with $\alpha = 3°$ at $E = 10^{-3}, 2 \times 10^{-4}$, and 10^{-4}, aiming to capture a broad range of amplitude variations, by studying the evolution of the variance, with the results presented in Figure 4.11. These plots show good agreement between experimental data and the model for small E. This agreement differs in the case $E = 10^{-3}$ probably because the model used for the flow lacks the effect of Ekman pumping, which is large at large E. It could be due to the forced Kelvin mode itself to the fact that the air in the room above the rotating cylinder is not rotating.



(a) (b)

Fig. 4.9 Comparison of samples with different initial positions for diffuselet (a) and experiment (b) in the case $\alpha = 3°$ and $E = 2 \times 10^{-4}$. In this case $N = 100$ diffuselets are randomly introduced in a small blob centered at the injection point of the experiments, with $s_0 = 2.2 \times 10^{-3}$ to match the mixing time of the experiments.

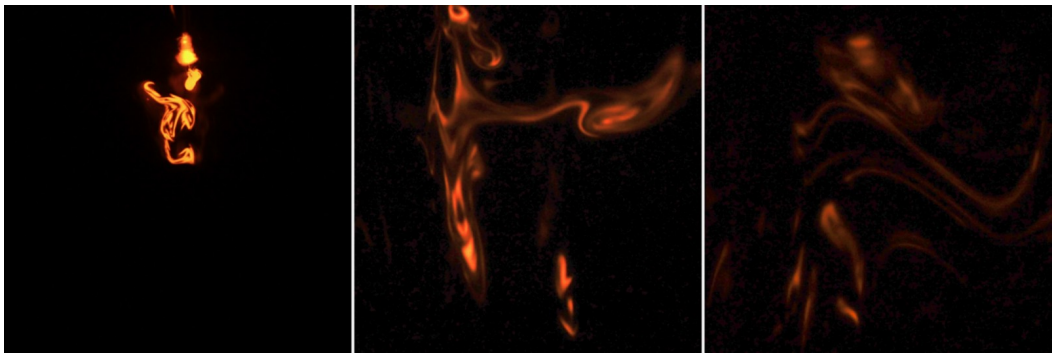
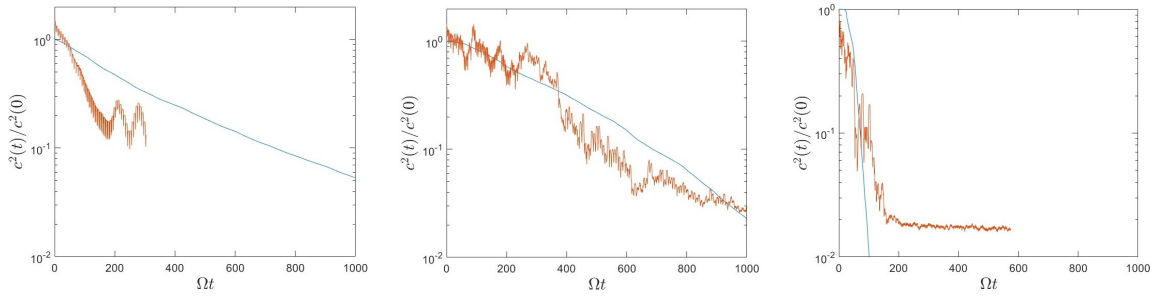


Fig. 4.10 Example of the evolution of the concentration field measured in experiments using the LIF method. This experiment is conducted for the parameters $\alpha = 1°$ and $E = 2.5 \times 10^{-4}$. The picture shows the initial injection, the field after ~ 10 min and after ~ 20 min.



(a) (b) (c)

Fig. 4.11 Comparison of the variance evolution between the Diffuselet (blue line) and experiment (orange line) for $\alpha = 3°$ and (from right to left) $E = 10^{-3}$, $E = 2 \times 10^{-4}$ and $E = 10^{-4}$.

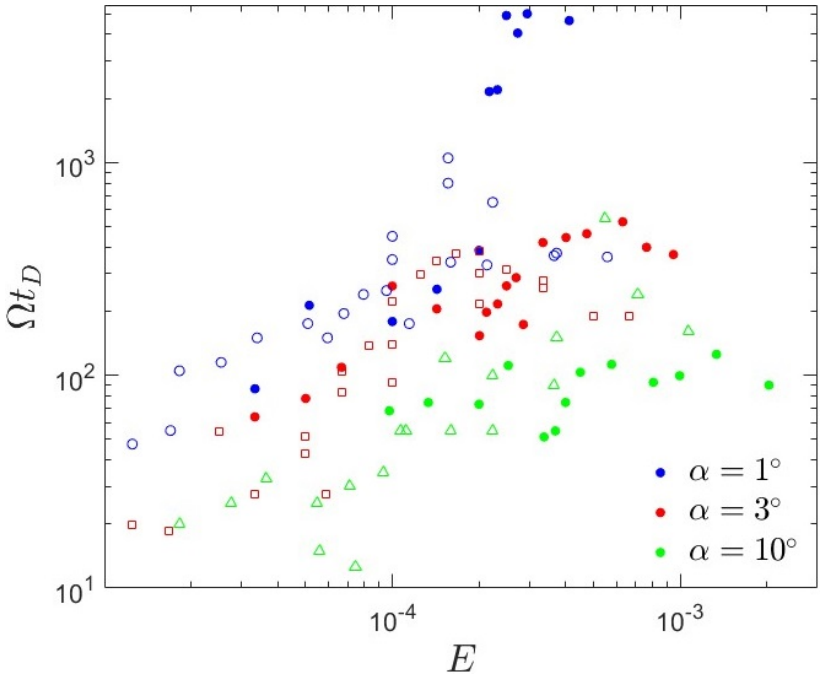


Fig. 4.12 The parameter t_D, representing the exponential decay of the variance, as a function of E. Filled points indicate numerical values, while empty points represent experimental data.

To quantify and compare the behavior of the variance across the range of parameters measured in the experiments, an exponential fit of the variance, $c^2(t) \sim e^{-t/t_D}$, is used. The result is shown in Figure 4.12. Despite the large scatter, the model predicts correctly the experimental results, with a gradual increase by a factor about 10 from small to large E. The increase of t_D with the tilt angle is also recovered in the model. However, the decay of t_D at large E in the experiments is not predicted. As mentioned before, it is probably due to Ekman pumping for these stable experiments.

Finally, the evolution of the PDF was calculated with the same simulations used for the variance and compared with the experimental data. Figure 4.13 shows the results of this comparison for $\alpha = 3°$ at $E = 2 \times 10^{-4}$ (a,b) and $E = 10^{-3}$ (c,d). The PDF calculated with the formula in equation (1.121) are the plots (a) and (c). It is clear from this data that there is no agreement between the results. This disagreement is attributable to the initial conditions considered in the model. Indeed, the formula used for the diffuselets is valid under the assumption that all diffuselets have an initial maximal concentration value $c_0 = 1$, i.e. that the PDF of initial concentration is

$$P_0(c_0) = \delta(c_0 - 1). \tag{4.11}$$

In experiments, injection is disordered and not instantaneous, so that in this process the flow begins to form a collection of structures in which the initial concentration c_0 is distributed around 1. This is clearly visible just after injection where the experiments display a monotonic decay from $c = 0.1$ to 1.3 whereas the model exhibits a peak at

$c = 1$. The previously used formula (1.121) has to be modified to alter the initial conditions of the distribution. This is possible through a convolution of the PDF $P(c/c_0)$ given by (1.121) with the distribution of the initial concentration $P_0(c_0)$ in log scale (Villermaux & Duplat 2003). The new theoretical PDF is thus calculated as

$$\tilde{P}(c) = \int_{c_0^{\min}}^{c_0^{\max}} P_0(c_0) P(c/c_0) dc_0/c_0. \tag{4.12}$$

Here, $P(c/c_0)$ is given by (1.121) and $P_0(c_0)$ is chosen in order to best describe the initial experimental PDF.

The model for the fitting is a power law $P_0'(c_0) = c_0^{-a}$ for $c_0^{\min} \leq c_0 \leq c_0^{\max}$. The results are shown in Figure 4.13 (b,d) where after the fit of the initial condition there is a better agreement with the experiment at moderate times (green). There is still a discrepancy in the large time limit. This discrepancy shows a well-known phenomenon in the diffuselets model which is the lack of overlap of concentrations. Indeed the model used here assumes that there is no aggregation of the diffuselets at late times although this is necessary to have a uniform concentration field. This could be done in the future.

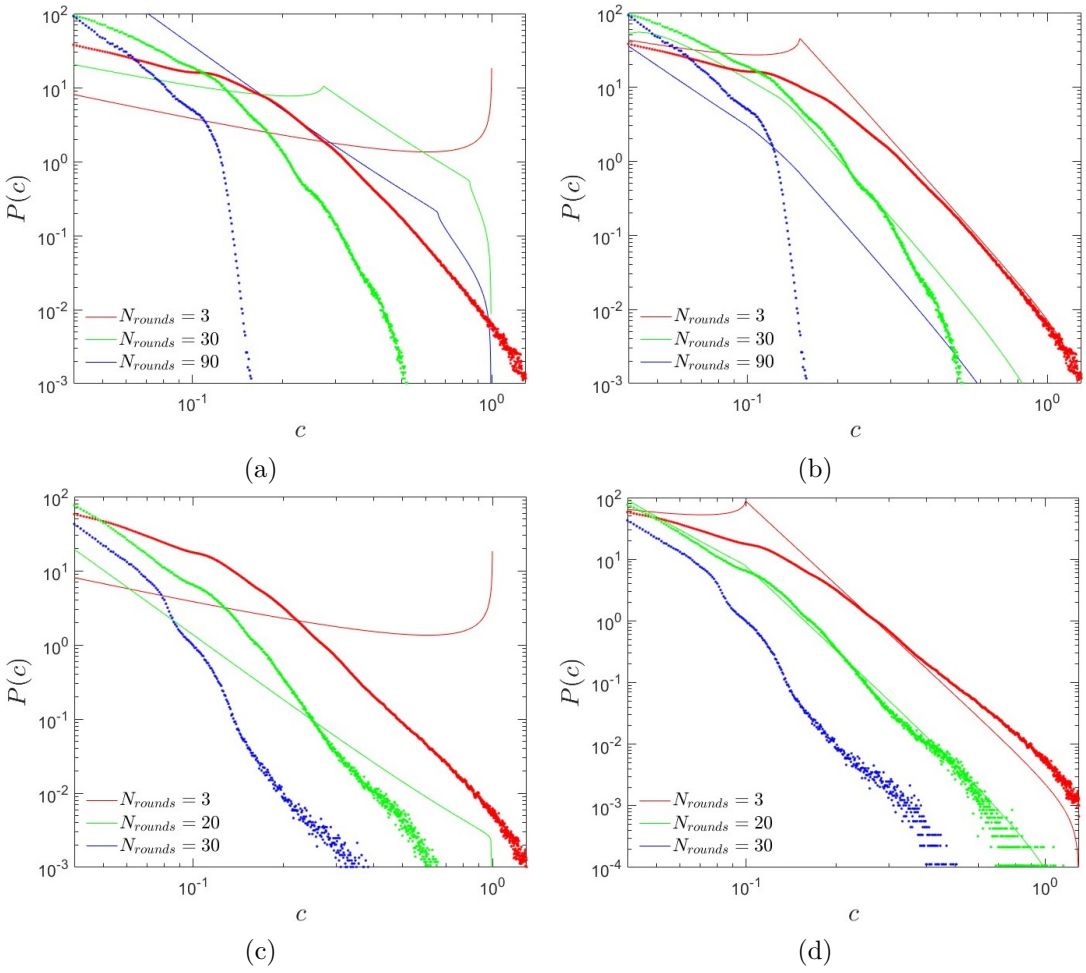


Fig. 4.13 Comparison of the PDF evolution between numerics (solid line) and experiments (points) for $\alpha = 3°$ at $E = 2 \times 10^{-4}$ (a,b) and $E = 10^{-4}$ (c,d). Solid lines are obtained by equation (1.121) in (a,c) and by equation (4.12) in (b,d). In these plots we can appreciate how the initial distribution of experiments differs from the model (a,c). By factoring the initial conditions of the experiments into the model, the evolution of the PDF is well described for short times (b,d).

Chapter 5

Stratified Fluid in Rotating Cylinder

The aim of this chapter is to observe how stratification alters the known motion in the unstratified case of a soft-mixer. This work involves preliminary observations of the flow within this setup, with the goal of conducting a future Particle Image Velocimetry (PIV) campaign to deepen understanding of the flow characteristics and, subsequently, to examine its mixing behavior.

5.1 Method and material

5.1.1 Experimental set-up

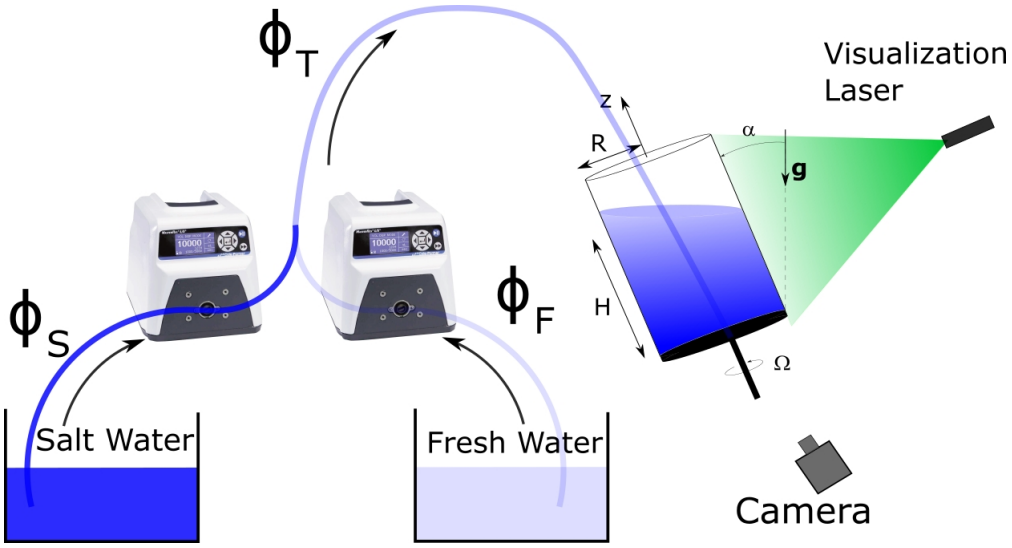


Fig. 5.1 Experimental set-up.

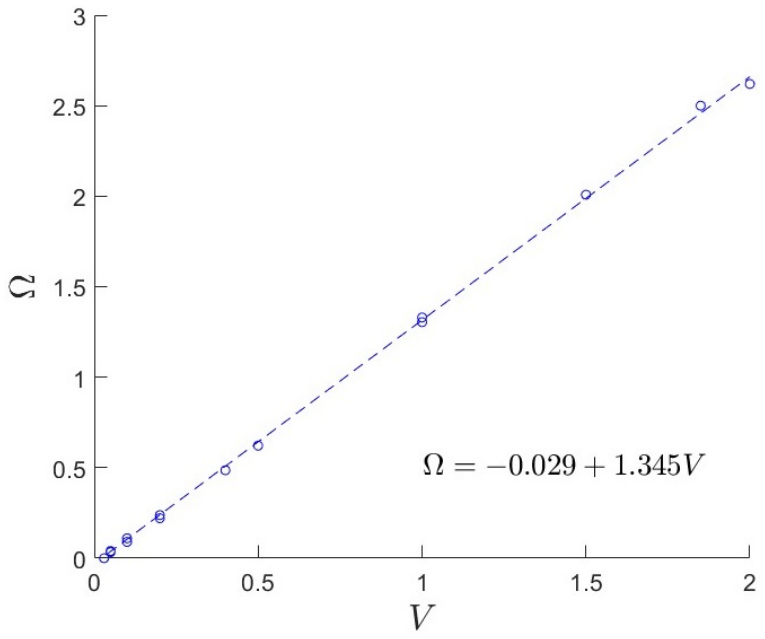


Fig. 5.2 Calibration curve of the motor used in the experiment.

The cylinder used for the experiment is characterized by a radius $R = 14.45$ cm and a height of 24 cm. It is placed on a rotating table driven by a remotely controlled motor, which allows adjustment of the rotation speed from a minimum of $\Omega_{min} \simeq 0.016$ rad/s to a maximum of $\Omega_{max} \simeq 2.6$ rad/s. The motor is controlled by a voltmeter, which has been calibrated (see Figure 5.2) by measuring Ω as a function of V, resulting in the following calibration curve

$$\Omega = -0.029 + 1.345V. \tag{5.1}$$

Two remotely controlled peristaltic pumps (**MasterFlex® L/S®** 07522-20) were used to fill the cylinder whit a linear saltwater stratification. For remote control, we used a computer running DigiFlow© software. The pumps were supplied by two independent reservoirs, one filled with a saturated salt solution ($\rho_s = 1.176$ g/cm^3) and the other with fresh water ($\rho_f = 1$ g/cm^3), each containing identical concentrations of Kalliroscope particles. The outflows from the pumps were combined through a junction connected to a pipe that delivered the mixed fluid to the bottom of the cylinder. A sponge was placed at the end of the pipe to minimize mixing with the fluid already injected. Visualization was achieved with a laser (of power 30 mW and wavelength 520 nm) to create a laser sheet, and a camera to capture data. Finally, an electronic inclinometer with an accuracy of 0.01° was used to measure inclination, and a graduated wedge was prepared for use in the various experiments.

5.1.2 Procedure

The procedure followed is as follows:

- The cylinder was filled with a linearly stratified saltwater solution under static, untilted conditions. All experiments were conducted with a water height of $H = 21.68$ cm giving a dimensionless height of $h = H/R \approx 1.5$. Stratification was achieved using a dual-pump system that created a linear density gradient with a buoyancy frequency of $N = [g(\rho_B - \rho_T)/(\rho_f H)]^{1/2} = 1.2 \pm 5\%$ s^{-1} with ρ_B and ρ_T the density at the bottom and the top. The two peristaltic pumps were connected to a metal tube that injected fluid at the cylinder's base, equipped with a sponge to minimize mixing upon injection. The pumps were computer-controlled to vary the flow rates each second, creating density layers from lightest to heaviest. The control settings ensured a target density at the top ($\rho_T = 1.1$ g/cm^3) and the maximum flow rate $\phi_{max} = \phi_S + \phi_F = 200$ ml/min, where ϕ_S and ϕ_F are respectively saltwater and freshwater flow rates. This prevented turbulent mixing and maintained clear separation between layers.

  Once N, the initial density ρ_T, and the liquid height H are set, we can calculate the required final density as

$$\rho_B = \rho_T \frac{2g/H + N^2}{2g/H - N^2}. \tag{5.2}$$

  Finally, with the maximum flux ϕ_{max}, the required number of time steps n_f can be determined as $n_f = V/(\phi_{max}\Delta t)$, with V in ml, ϕ_{max} in ml/min and Δt of about 1 minute.

  To automate the described process, the following routine was used:

$$\begin{cases} \rho_n = \rho_T + \frac{n}{n_f}(\rho_B - \rho_T) \\ \phi_S^n = \phi_{max}\frac{\rho_n - \rho_F}{\rho_S - \rho_F} \\ \phi_F^n = \phi_{max}\frac{\rho_S - \rho_n}{\rho_S - \rho_F} \end{cases}, \tag{5.3}$$

  where ρ_n is the layer density at each time step n.

- The density profile was measured by sampling the fluid at various heights using a syringe. Each sample was then analyzed with a densimeter, with a sensitivity of $\delta\rho = 10^{-6}$ g/cm^3, to determine its density.

- Following static stratification, the fluid was subjected to a spin-up phase. To minimize mixing, a non-linear spin-up procedure was employed by setting the Rossby number to $Ro = 0.09$[1]. At each increment, the system was allowed to stabilize for the spin-up time $t_s \simeq 362.208\Omega^{-1/2}$ s, starting from the motor's minimum allowable rotational speed $\Omega_{min} \simeq 0.016$ rad/s.

[1]This value was chosen to limit changes in N to less than 10% and to complete the spin-up procedure overnight.

This procedure can be summarized by the following formula:

$$\Omega_n = \begin{cases} (1+Ro)^n \Omega_{min} & \text{for} \quad 0 \leq n \leq n_{max} = \frac{\ln \Omega_f/\Omega_{min}}{\ln(1+Ro)} \\ \Omega_f & \text{for} \quad n = n_{max}+1 \end{cases} . \tag{5.4}$$

At the end of the procedure, we allowed the salt to diffuse ($t_d \simeq 5.8$ h) to ensure that the vertical layers reached a stationary condition. While this method does not provide optimal control over the experimental parameters, it still requires approximately 20 hours to complete the setup. A faster approach, developed by Munro *et al.* (2010), involves a linear spin-up phase with a diffusion time of about 8 hours, focusing solely on salt diffusion. However, the paper does not specify the duration for each increment of angular velocity. For this reason, the spin-up time was used in our experiment, even though, in the stratified case, Ekman pumping is significantly damped. Despite this, the spin-up procedure was the most careful approach to avoid mixing.

- At the end of the preparation, we used a laser sheet and a camera to capture the motion while incrementally changing the inclination of the cylinder.

5.1.3 Measurement of the Stratification

First, the method used to fill the cylinder produces a linear density profile, except in the region where the height is $\lesssim 3$ cm. The uncertainty in the value of N is 5%.

Second, a measurement was made to assess the change in N due to mixing during the spin-up phase. The results show that the initial condition does not decrease by more than 10% (see Figure 5.3).

In the experiments, the stratification was measured before the spin-up procedure. So from the measured values of N, a decrease in the measured value of 5% is taken into account and then the cumulative error of the measurement and confidence due to the spin-up procedure is taken into account.

5.2 Experimental results

The results of the experiments are summarized in the stability diagram in parameter space (α vs. Fr), shown in Figure 5.4. In this context, the Froude number is defined as $Fr = \Omega/N$. The flow remains stable for small tilt angles (black symbols) but destabilizes as the tilt angle increases. The critical tilt angle depends non-monotonically on the Froude number, suggesting the presence of two distinct regimes. In the region where $Fr \gtrsim 1.4$, the flow exhibits a behavior similar to the unstratified case, showing the presence of a triadic instability. An example of the observed pattern is shown in Figure 5.5. It appears that decreasing the Froude number stabilizes the flow in this region.

For $Fr \lesssim 1.4$, a different pattern is observed in the Kalliroscope visualizations. In this region, the fluid exhibits a global oscillation of the vortices.

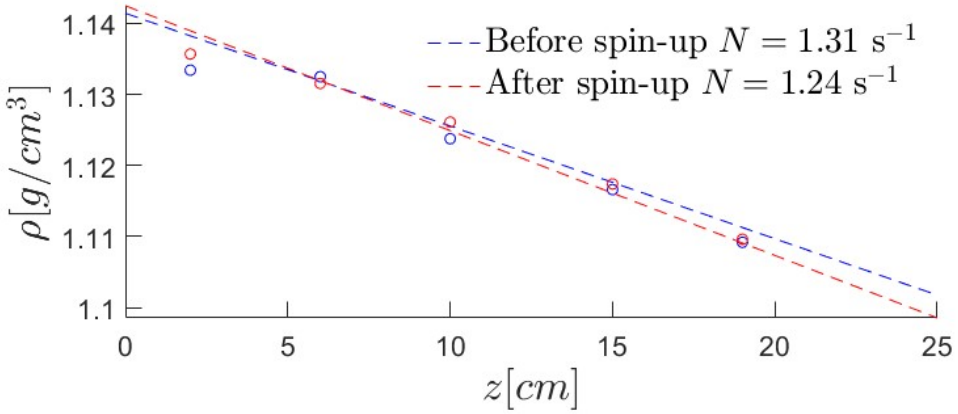


Fig. 5.3 Example of how the spin-up procedure affects the value of N for the maximum obtainable rotation speed $\Omega \simeq 2.6$ rad/s. The symbols are obtained before the spin-up (blue) and after the spin-up during the solid body rotation (red). The dashed lines are the linear fits of the density profile before (blue) and after (red) the spin-up effect.

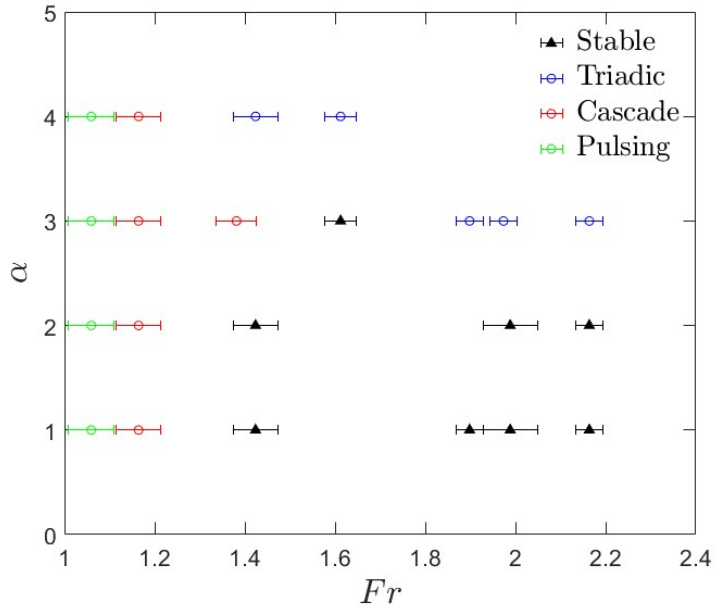
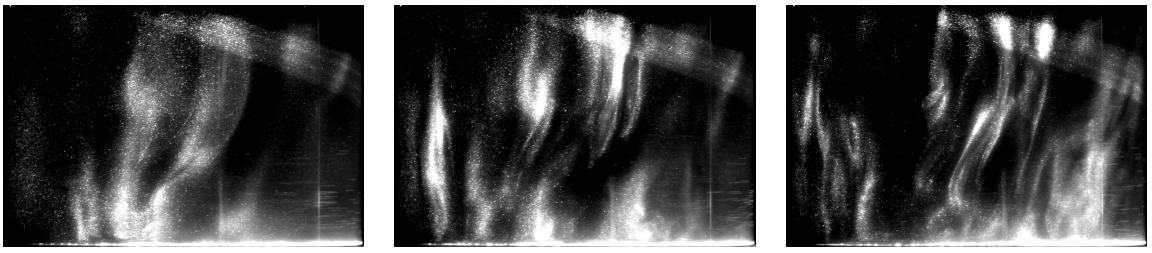
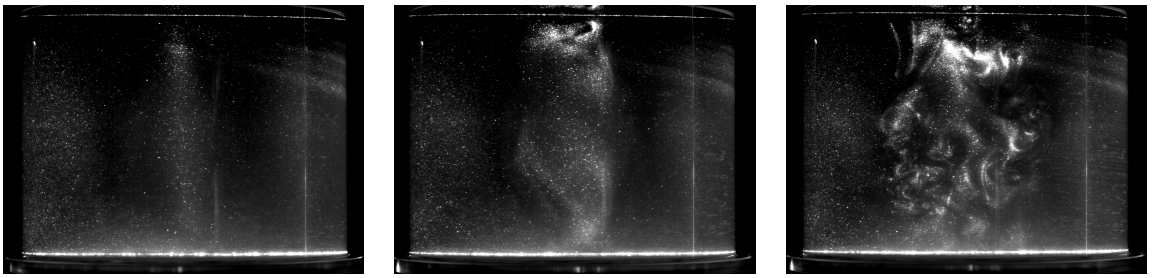


Fig. 5.4 Results of the experiments in the parameter space (α vs. Fr). The results are reported by category of the observed patterns in various colors.



(a) (b) (c)

Fig. 5.5 Pattern of triadic instability for $Fr = 1.88$ and $\alpha = 3°$. From left to right, the temporal evolution of this instability can be observed.



(a) (b) (c)

Fig. 5.6 Pattern cascade like observed for $Fr = 1.14$ and $\alpha = 1°$.

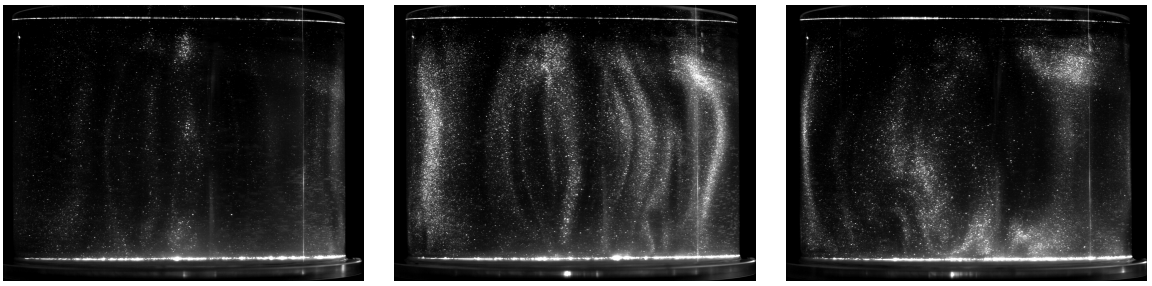
We have referred to the case where the vortices remain stable under this oscillation as pulsing-like. This pattern is characterized by pulsations originating from the edges, with a preliminary observation of elliptic vortices.

As the Froude number decreases further, we observed a breakdown of the vortices, resulting in a cascade effect with the intermittent formation of small structures in the flow. This behavior is referred to as cascade-like. It occurs when the pulsing becomes strong enough to trigger a cascade toward smaller scales, driven by the interaction of two fronts from the edges, as shown in Figure 5.6.

Finally, as the Froude number decreases further, approaching $Fr \to 1$, the number of vortices within the fluid increases. In this case, the formation of small structures is no longer observed (see Figure 5.7). This suggests a weaker instability. However the threshold angle (critical angle for the onset of the instability) could not be identified as no stable flow was observed at 1°.

5.3 Theoretical Background

Following the work of Guimbard *et al.* (2010), the evolution of the base flow is modeled by the linearized Navier-Stokes equations under the Boussinesq approximation, coupled with a buoyancy force $\left(\vec{b} = \frac{z}{\rho_0}\partial_z \rho \vec{g}\right)$, in a reference frame rotating with the cylinder,



(a) (b) (c)

Fig. 5.7 Pattern observed for $Fr = 1.03$ and $\alpha = 1°$.

expressed as:

$$\begin{cases} \partial_t \mathbf{u} + 2(\hat{\mathbf{z}} \wedge \mathbf{u}) = -\nabla p + \mathbf{b} + E\nabla^2 \mathbf{u} \\ \partial_t b = -\frac{1}{Fr^2}\mathbf{u} \cdot \hat{\mathbf{z}} \\ \nabla \cdot \mathbf{u} = 0 \end{cases} . \tag{5.5}$$

This system is nondimensionalized in the same manner as the unstratified case, using the length scale R and time scale Ω^{-1}, where the Froude number becomes $Fr = 1/N$.

Taking the Ansatz

$$\begin{cases} \mathbf{u} = \sum_{j=1}^{\infty} \mathrm{Re}\left[A_j \begin{pmatrix} u_j(r)\cos(k_j z) \\ v_j(r)\cos(k_j z) \\ w_j(r)\sin(k_j z) \end{pmatrix} e^{i(\theta+t)} \right] \\ p = \sum_{j=1}^{\infty} \mathrm{Re}\Big[A_j p_j(r)\cos(k_j z) e^{i(\theta+t)} \Big] \\ b = \sum_{j=1}^{\infty} \mathrm{Re}\Big[A_j b_j(r)\sin(k_j z) e^{i(\theta+t)} \Big] \end{cases} , \tag{5.6}$$

it is possible to find the relation

$$\begin{cases} u_j(r) = \frac{-i}{3}\Big(\partial_r p_j(r) + \frac{2}{r} p_j(r)\Big) \\ v_j(r) = \frac{1}{3}\Big(2\partial_r p_j(r) + \frac{1}{r} p_j(r)\Big) \\ w_j(r) = -\frac{k}{1-Fr^{-2}} p_j(r) \\ b_j(r) = -\frac{ik}{1-Fr^{-2}} p_j(r) \end{cases} . \tag{5.7}$$

The equation for the pressure is found as the unstratified case, adding the buoyancy force, leading to:

$$\begin{cases} \Big[\frac{d^2}{dr^2} + \frac{1}{r}\frac{d}{dr} + \Big(\Lambda_j^2 - \frac{1}{r^2}\Big)\Big] p_j(r) = 0 \\ \Lambda_j^2 = k_j^2 \frac{3}{1-Fr^{-2}} \end{cases} , \tag{5.8}$$

with solution

$$p_j(r) = J_1(\Lambda_j r). \tag{5.9}$$

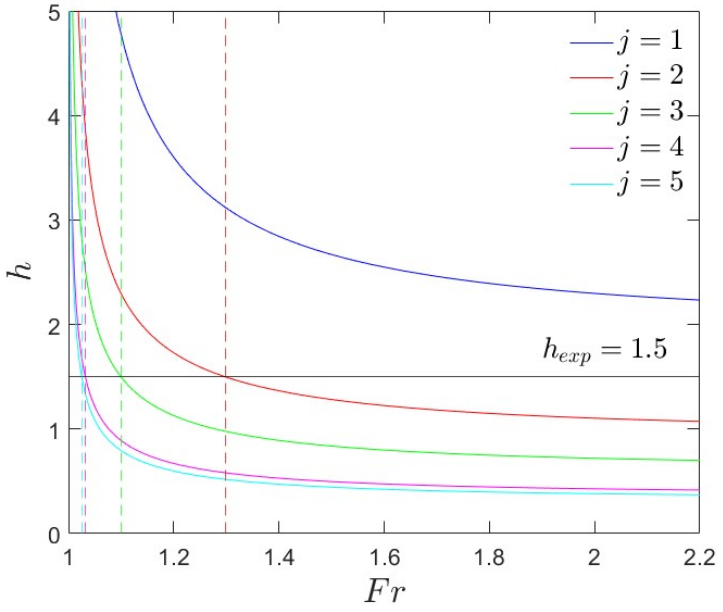


Fig. 5.8 Resonant height given by (5.13) as a function of Froude number for the first modes. The black line at $h_{exp} = 1.5$ is the height of fluid used in the experiment. The dashed lines are the resonances of various modes for $h = h_{exp}$.

The radial wavenumbers Λ_j are determined by assuming that $u = 0$ at $r = 1$, yielding $\Lambda_1 = 2.73$, $\Lambda_2 = 5.69$, $\Lambda_3 = 8.77$, and so on. In this configuration the axial wavenumbers depends on the Froude number trough (5.8).

Then, similar to the unstratified case, we can derive the expression for the amplitude by assuming that $w(z = h)$, as defined in (5.6), is equal to the velocity of the free surface, as given in equation (1.30). Multiplying by $rJ_1(\Lambda_1 r)$ and integrating with respect to r results in

$$A_j = \frac{\alpha \tilde{F}_j}{\tilde{T}_j \sin(k_j h)}, \tag{5.10}$$

where

$$\tilde{F}_j = \int_0^1 r^2 J_1(\Lambda_j r) dr = \frac{3}{\Lambda_j^2} J_1(\Lambda_j), \tag{5.11}$$

and

$$\tilde{T}_j = \frac{-k_j}{1 - Fr^{-2}} \int_0^1 r J_1^2(\Lambda_j r) dr = \frac{-k_j}{2(1 - Fr^{-2})} \left(1 + \frac{3}{\Lambda_j^2}\right) J_1^2(\Lambda_j). \tag{5.12}$$

The amplitude A_j diverges when $k_j h = \pi$. The expression for the resonant height in the stratified case is

$$h_j = \frac{\pi}{\Lambda_j} \sqrt{\frac{3}{1 - Fr^{-2}}}, \tag{5.13}$$

where Λ_j are known numerically.

These resonant heights are plotted in Figure 5.8 as a function of Fr. The key difference from the unstratified case is the dependence on the Froude number, with the heights increasing monotonically as $Fr \to 1$, reaching a limit where they diverge for all modes at $Fr = 1$.

In the experiments, $h = 1.5$ was chosen with Fr spanning from 1 to 2.2, allowing for the selection of different resonances across various modes. To better understand the development of these modes, we rewrite the amplitude as

$$A_j = \frac{-6\sqrt{3}\alpha}{\Lambda_j(\Lambda_j^2+3)J_1(\Lambda_j)} \frac{\sqrt{1-Fr^{-2}}}{\sin(\frac{\Lambda_j}{\sqrt{3}}\sqrt{1-Fr^{-2}}h)}. \tag{5.14}$$

We can assume that the flow will destabilize when the amplitude exceeds a critical value A_j^{C}. This allows us to define the critical tilt angle for the various modes:

$$\alpha_j^{\mathrm{C}} = B_j^{\mathrm{C}} \frac{\sin(\frac{\Lambda_j}{\sqrt{3}}\sqrt{1-Fr^{-2}}h)}{\sqrt{1-Fr^{-2}}}, \tag{5.15}$$

where $B_j^{\mathrm{C}} = A_j^{\mathrm{C}}\Lambda_j(\Lambda_j^2+3)J_1(\Lambda_j)/6\sqrt{3}$ is used as a fitting parameter in Figure 5.4. The bands of instabilities predicted by this simple theory clearly corresponds to the unstable domain found experimentally. This plot also illustrates how the different patterns observed are strongly correlated with the different Kelvin modes.

Subsequent studies are needed to increase the number of experiments in the transition regions and to conduct a PIV campaign to measure the various amplitudes and quantify the instabilities observed in this study.

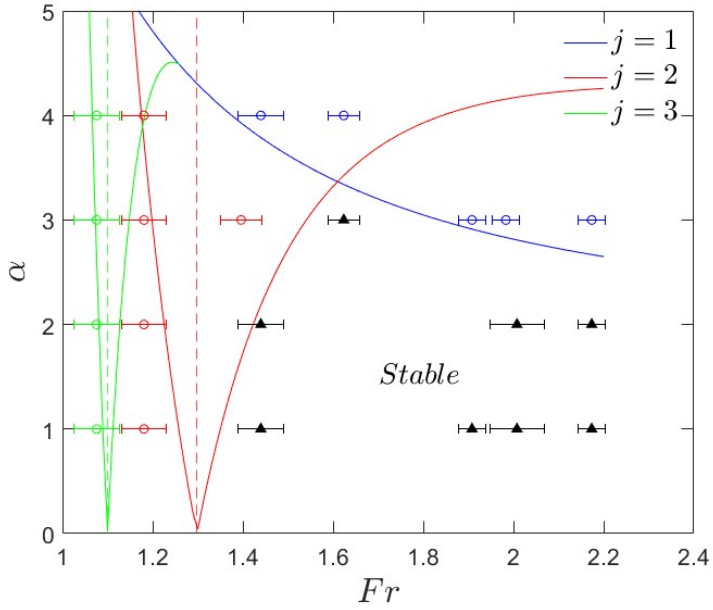


Fig. 5.9 Parametric space of the experimental results compared with the critical tilt angle of the modes defined in Equation (5.15). The experimental symbols are defined in Figure 5.4. This plot shows that the resonances of the various modes can be used to distinguish the flow behavior in the different experiments, with the stable region corresponding to the overlap of the areas below the resonances of the main modes.

Chapter 6

Conclusion

6.1 Summary

The work presented in this manuscript is a compendium of studies carried out to understand the flow and mixing properties of the soft mixer.

In Chapter 2, the study was adapted from cylindrical to annular geometry, revealing that the amplitude of the forced mode follows the same law, changes in geometric ratios alter the coefficients of the dispersion relation and of the viscous corrections. The basic physics remains consistent, but the resonant height decreases as the annulus's inner radius increases. The first forced mode amplitude matches experimental data.

As in the cylindrical case, forced mode resonances trigger instabilities, experimentally quantified by the onset time as a function of fluid height, which shows minima for multiples of the resonant height.

The main instability is a triadic instability with azimuthal wavenumbers increasing as the inner radius increases: $m' = 5$, $m'' = 6$ for $r_i = 0$ (cylinder); $m' = 9$, $m'' = 10$ for $r_i = 0.33$, and $m' = 17$, $m'' = 18$ for $r_i = 0.55$.

The stability theory was extended to this case, showing excellent agreement with experimental results across the measured parameter space concerning the wavenumbers, but also the critical Ekman number.

In addition, a centrifugal instability was observed on the inner edge of the annulus for large tilt angles, with the formation of the axial vortices typical of this instability. We attribute the presence of this instability to geostrophic motion which, as in the case of the cylinder, is retrograde. It decelerates the motion on the edge of the inner cylinder and makes the layer unstable with a negative Rayleigh discriminant.

Mixing experiments confirmed that the resonances and the instabilities enhances the mixing efficiency. Additionally, a systematic study across the parameter space revealed a monotonic increase in efficiency with rising values of α and decreasing values of E.

In Chapter 3, we described how the code written to do simulations with the diffuselet method in 3D is well validated in the simple flows of a shear and a uniform stretching. Furthermore, a description of the application to the case of homogeneous turbulence is

presented showing the predictive capabilities of the code in good agreement with the DNS results for $Sc = 70$. The variance and the evolution of the PDF are well captured at moderate times, even if the aggregation process, not considered within the model, creates discrepancies at late times.

Chapter 4, describes the case of the cylindrical soft mixer, where the flow is modeled by a sum of Kelvin modes measured by PIV and the code is adapted to this empirical flow. It gives the possibility to predict mixing within the soft mixer. The evolution of the experimental and numerical variance was compared. Using a simple exponential fit of the variance decay, it was possible to quantify the mixing efficiencies. The mixing protocol becomes faster as the Ekman number decreases and as the tilt angle increases, since the flow becomes more chaotic. A good quantitative agreement is observed for small Ekman numbers. However, a small discrepancy is present at the largest Ekman numbers, probably due to Ekman pumping in the experiments.

The model showed that the decay of the variance depends on the initial position of the injected scalar, due to the presence of KAM torus in the Poincaré sections. However this effect could not be reproduced in the experiments because the injection was too turbulent.

An example of a comparison between the evolution of the concentration field PDFs is shown in the final part of the chapter. The theoretical PDF must be adapted to the experiments since the turbulent injection creates a broad distribution of concentration instead of an homogeneous concentration at $c_0 = 1$. The temporal evolution of the PDF is well predicted for short periods of time. The trend for long times shows that the aggregation phenomenon not present in the diffuselet method leads to a discrepancy with the experiments.

We have also shown how the diffuselet method allows the mixing time distribution to be calculated. It agrees with the asymptotic limits expected in the normal log model.

Finally, in Chapter 5, observations of the flow stability in the case of a cylindrical soft mixer with a stratified fluid are reported, showing the observed patterns and parameter space. These measurements showed the existence of various instability bands. Using a simple linear theory of inviscid amplitudes, it was possible to predict these bands theoretically.

6.2 Future work

The work done on the cylinder is far from finished; in fact a conclusive formula describing the mixing in the observed parameter space is still needed. Designing new experiments on the flow with a set up that allows it to be measured in 3D would help to improve the predictions of the diffuselet method as well as give the possibility of more knowledge to study its transition to turbulence. In this direction, the use of the wave turbulence formalism could lead to the description of the observed spectrum as well as the axial spectrum.

The same applies to the stratified case where a first step is to increase the points in parameter space and extend the theory to viscous corrections. Furthermore, through PIV experiments, one could quantitatively study the amplitudes to improve the developed theory.

With regard to mixing, the study shown in Chapter 4 is still in progress. The results regarding the distribution of mixing times must be investigated further in order to arrive at an analytical model of the concentration field distribution. Furthermore, the study of the evolution at long times, including the phenomenon of aggregation, is necessary to conclude the study and verify the analytical model.

A further study is at an early stage concerning a mixing experiment in homogeneous turbulence inside a water tunnel for which the instruments developed in the study of this thesis will be applied.

References

[1] Albrecht, T, Blackburn, HM, Lopez, JM, Manasseh, R & Meunier, P 2015 Triadic resonances in precessing rapidly rotating cylinder flows. *Journal of Fluid Mechanics* **778**, R1.

[2] Albrecht, T, Blackburn, HM, Lopez, JM, Manasseh, R & Meunier, P 2016 Components of mean streaming flow in a precessing cylinder at small nutation angles. In *International Congress of Theoretical and Applied Mechanics 2016*, pp. 1616–1617. International Union of Theoretical and Applied Mechanics.

[3] Albrecht, T, Blackburn, HM, Lopez, JM, Manasseh, R & Meunier, P 2018 On triadic resonance as an instability mechanism in precessing cylinder flow. *Journal of Fluid Mechanics* **841**, R3.

[4] Albrecht, Thomas, Blackburn, Hugh M, Lopez, Juan M, Manasseh, Richard & Meunier, Patrice 2021 On the origins of steady streaming in precessing fluids. *Journal of Fluid Mechanics* **910**, A51.

[5] Batchelor, George K 1959 Small-scale variation of convected quantities like temperature in turbulent fluid part 1. general discussion and the case of small conductivity. *Journal of Fluid Mechanics* **5** (1), 113–133.

[6] Bayly, BJ 1986 Three-dimensional instability of elliptical flow. *Physical Review Letters* **57** (17), 2160.

[7] Betchov, R 1956 An inequality concerning the production of vorticity in isotropic turbulence. *Journal of Fluid Mechanics* **1** (5), 497–504.

[8] Bödewadt, Von UT 1940 Die drehströmung über festem grunde. *ZAMM-Journal of Applied Mathematics and Mechanics/Zeitschrift für Angewandte Mathematik und Mechanik* **20** (5), 241–253.

[9] Bordes, Guilhem, Moisy, Frédéric, Dauxois, Thierry & Cortet, Pierre-Philippe 2012 Experimental evidence of a triadic resonance of plane inertial waves in a rotating fluid. *Physics of Fluids* **24** (1).

[10] Buch, Kenneth A & Dahm, Werner JA 1996 Experimental study of the fine-scale structure of conserved scalar mixing in turbulent shear flows. part 1. sc [gt] 1. *Journal of Fluid Mechanics* **317**, 21–71.

[11] Busse, Friedrich H 1970 Thermal instabilities in rapidly rotating systems. *Journal of Fluid Mechanics* **44** (3), 441–460.

[12] Bustamante, Maritza CC, Cerri, Marcel O & Badino, Alberto C 2013 Comparison between average shear rates in conventional bioreactor with rushton and elephant ear impellers. *Chemical Engineering Science* **90**, 92–100.

[13] Camacho, F García, Rodríguez, JJ Gallardo, Mirón, A Sánchez, García, MC Cerón, Belarbi, EH & Grima, E Molina 2007 Determination of shear stress thresholds in toxic dinoflagellates cultured in shaken flasks: implications in bioprocess engineering. *Process Biochemistry* **42** (11), 1506–1515.

[14] Chandrasekhar, S 1961 *Hydrodynamic and Hydromagnetic Stability*. Clarendon Press, Oxford.

[15] Cherry, RS & Papoutsakis, ET 1986 Hydrodynamic effects on cells in agitated tissue culture reactors. *Bioprocess Engineering* **1**, 29–41.

[16] Crow, Steven C 1970 Stability theory for a pair of trailing vortices. *AIAA Journal* **8** (12), 2172–2179.

[17] Davidson, Peter 2015 *Turbulence: an introduction for scientists and engineers*. Oxford University Press.

[18] Davidson, Peter Alan 2024 *The Dynamics of Rotating Fluids*. Oxford University Press.

[19] De Jesus, Sérgio S, Neto, João Moreira & Maciel Filho, Rubens 2017 Hydrodynamics and mass transfer in bubble column, conventional airlift, stirred airlift and stirred tank bioreactors, using viscous fluid: A comparative study. *Biochemical engineering journal* **118**, 70–81.

[20] Detournay, Olivier & Meunier, Patrice 2024 Cell culture system, method and assembly. US Patent App. 18/266,242.

[21] Doran, Pauline M 1999 Design of mixing systems for plant cell suspensions in stirred reactors. *Biotechnology progress* **15** (3), 319–335.

[22] Duplat, Jerôme & Villermaux, Emmanuel 2008 Mixing by random stirring in confined mixtures. *Journal of Fluid Mechanics* **617**, 51–86.

[23] Ekman, Vagn Walfrid 1905 On the influence of the earth's rotation on ocean-currents. *Ark. Mat. Astron. Fys.* .

[24] Eloy, Christophe & Le Dizès, Stéphane 1999 Three-dimensional instability of burgers and lamb–oseen vortices in a strain field. *Journal of Fluid Mechanics* **378**, 145–166.

[25] Ernst-Hullermann, Julia, Harder, Helmut & Hansen, Ulrich 2013 Finite volume simulations of dynamos in ellipsoidal planets. *Geophysical Journal International* **195** (3), 1395–1405.

[26] Fenstermacher, PR, Swinney, Harry L & Gollub, JP 1979 Dynamical instabilities and the transition to chaotic taylor vortex flow. *Journal of Fluid Mechanics* **94** (1), 103–128.

[27] Fountain, GO, Khakhar, DV & Ottino, JM 1998 Visualization of three-dimensional chaos. *Science* **281** (5377), 683–686.

[28] Gans, Roger F 1970 On the precession of a resonant cylinder. *Journal of Fluid Mechanics* **41** (4), 865–872.

[29] Gans, Roger F 1971 On hydromagnetic precession in a cylinder. *Journal of Fluid Mechanics* **45** (1), 111–130.

[30] Gao, Donglai, Meunier, Patrice, Le Dizès, Stéphane & Eloy, Christophe 2021 Zonal flow in a resonant precessing cylinder. *Journal of Fluid Mechanics* **923**, A29.

[31] Garcia-Ochoa, Felix & Gomez, Emilio 2009 Bioreactor scale-up and oxygen transfer rate in microbial processes: an overview. *Biotechnology advances* **27** (2), 153–176.

[32] Gauthier, Georges, Gondret, Philippe & Rabaud, Marc 1998 Motions of anisotropic particles: application to visualization of three-dimensional flows. *Physics of Fluids* **10** (9), 2147–2154.

[33] Giesecke, André, Albrecht, Thomas, Gundrum, Thomas, Herault, Johann & Stefani, Frank 2015 Triadic resonances in nonlinear simulations of a fluid flow in a precessing cylinder. *New Journal of Physics* **17** (11), 113044.

[34] Giesecke, André, Vogt, Tobias, Gundrum, Thomas & Stefani, Frank 2018 Nonlinear large scale flow in a precessing cylinder and its ability to drive dynamo action. *Physical Review Letters* **120** (2), 024502.

[35] Girimaji, SS & Pope, SB 1990 Material-element deformation in isotropic turbulence. *Journal of fluid mechanics* **220**, 427–458.

[36] Glatzmaiers, Gary A & Roberts, Paul H 1995 A three-dimensional self-consistent computer simulation of a geomagnetic field reversal. *Nature* **377** (6546), 203–209.

[37] Gledzer, EB 1975 An experimental and theoretical study of the stability of motion of a liquid in an elliptical cylinder. *Izv. Atoms. Ocean Phys.* **11**, 617–622.

[38] Gledzer, EB, Novikov, Yu V, Obukhov, AM & Chusov, MA 1974 An investigation of the stability of liquid flows in a three-axis ellipsoid. *Isv. Atmos. Ocean. Phys* **10**, 69–71.

[39] Gledzer, EB & Ponomarev, VM 1977 Finite-dimensional approximation of the motions of incompressible fluids within an ellipsoid. *Akademiia Nauk SSSR Fizika Atmosfery i Okeana* **13**, 820–827.

[40] Goto, Susumu, Shimizu, Masaki & Kawahara, Genta 2014 Turbulent mixing in a precessing sphere. *Physics of Fluids* **26** (11).

[41] Greenspan, HP 1969 On the lnviscid theory of rotating fluids. *Studies in Applied Mathematics* **48** (1), 19–28.

[42] Greenspan, Harvey Philip 1968 *The theory of rotating fluids.*. Cambridge University Press.

[43] Guimbard, David, Le Dizès, Stéphane, Le Bars, Michael, Le Gal, Patrice & LEBLANC, Stéphane 2010 Elliptic instability of a stratified fluid in a rotating cylinder. *Journal of Fluid Mechanics* **660**, 240–257.

[44] Halim, Alexander, Ariyanti, Agnes Dwi, Luo, Qing & Song, Guanbin 2020 Recent progress in engineering mesenchymal stem cell differentiation. *Stem cell reviews and reports* **16**, 661–674.

[45] Herault, Johann, Gundrum, Thomas, Giesecke, André & Stefani, Frank 2015 Subcritical transition to turbulence of a precessing flow in a cylindrical vessel. *Physics of Fluids* **27** (12).

[46] Kantarci, Nigar, Borak, Fahir & Ulgen, Kutlu O 2005 Bubble column reactors. *Process biochemistry* **40** (7), 2263–2283.

[47] Kelvin, Lord 1880 Vibrations of a columnar vortex. *Proceedings of the Royal Society of Edinburgh* **10**, 443–456.

[48] Kerswell, RR 1993 The instability of precessing flow. *Geophysical & Astrophysical Fluid Dynamics* **72** (1-4), 107–144.

[49] Kerswell, RR 1996 Upper bounds on the energy dissipation in turbulent precession. *Journal of Fluid Mechanics* **321**, 335–370.

[50] Kerswell, RR 1999 Secondary instabilities in rapidly rotating fluids: inertial wave breakdown. *Journal of Fluid Mechanics* **382**, 283–306.

[51] Kerswell, Richard R 2002 Elliptical instability. *Annual review of fluid mechanics* **34** (1), 83–113.

[52] Kudlick, Michael Douglas 1966 On transient motions in a contained, rotating fluid. PhD thesis, Massachusetts Institute of Technology.

[53] Lagrange, Romain, Eloy, Christophe, Nadal, François & Meunier, Patrice 2008 Instability of a fluid inside a precessing cylinder. *Physics of Fluids* **20** (8).

[54] Lagrange, Romain, Meunier, Patrice, Eloy, Christophe & Nadal, François 2009 Dynamics of a fluid inside a precessing cylinder. *Mechanics & Industry* **10** (3-4), 187–194.

[55] Lagrange, Romain, Meunier, Patrice, Nadal, François & Eloy, Christophe 2011 Precessional instability of a fluid cylinder. *Journal of Fluid Mechanics* **666**, 104–145.

[56] Landeau, Maylis, Fournier, Alexandre, Nataf, Henri-Claude, Cébron, David & Schaeffer, Nathanaël 2022 Sustaining earth's magnetic dynamo. *Nature Reviews Earth & Environment* **3** (4), 255–269.

[57] Landman, MJ & Saffman, PG 1987 The three-dimensional instability of strained vortices in a viscous fluid. *Physics of Fluids* **30** (8), 2339–2342.

[58] Larmor, Joseph 1919 How could a rotating body such as the sun become a magnet? In *A Source Book in Astronomy and Astrophysics, 1900–1975*, pp. 106–107. Harvard University Press.

[59] Le Bars, Michael, Cébron, David & Le Gal, Patrice 2015 Flows driven by libration, precession, and tides. *Annual Review of Fluid Mechanics* **47** (1), 163–193.

[60] Lefranc, Cyril 2023 Optimization of a bioreactor type "soft-mixer" : for the growth of microalgae. PhD thesis, Aix-Marseille.

[61] Lin, Yufeng, Noir, Jerome & Jackson, Andrew 2014 Experimental study of fluid flows in a precessing cylindrical annulus. *Physics of Fluids* **26** (4).

[62] Loper, David E 1975 Torque balance and energy budget for the precessionally driven dynamo. *Physics of the Earth and Planetary Interiors* **11** (1), 43–60.

[63] Lopez, Juan M & Marques, Francisco 2016 Nonlinear and detuning effects of the nutation angle in precessionally forced rotating cylinder flow. *Physical Review Fluids* **1** (2), 023602.

[64] Lopez, Juan M & Marques, Francisco 2018 Rapidly rotating precessing cylinder flows: forced triadic resonances. *Journal of Fluid Mechanics* **839**, 239–270.

[65] Lorenzani, Silvia & Tilgner, Andreas 2001 Fluid instabilities in precessing spheroidal cavities. *Journal of Fluid Mechanics* **447**, 111–128.

[66] Lorenzani, Silvia & Tilgner, Andreas 2003 Inertial instabilities of fluid flow in precessing spheroidal shells. *Journal of Fluid Mechanics* **492**, 363–379.

[67] Malkus, Willem VR 1989 An experimental study of global instabilities due to the tidal (elliptical) distortion of a rotating elastic cylinder. *Geophysical & Astrophysical Fluid Dynamics* **48** (1-3), 123–134.

[68] Manasseh, Richard 1992 Breakdown regimes of inertia waves in a precessing cylinder. *Journal of Fluid Mechanics* **243**, 261–296.

[69] Manasseh, Richard 1994 Distortions of inertia waves in a rotating fluid cylinder forced near its fundamental mode resonance. *Journal of Fluid Mechanics* **265**, 345–370.

[70] Marques, Francisco & Lopez, Juan M 2015 Precession of a rapidly rotating cylinder flow: traverse through resonance. *Journal of Fluid Mechanics* **782**, 63–98.

[71] Martínez-Ruiz, Daniel, Meunier, Patrice, Favier, Benjamin, Duchemin, Laurent & Villermaux, Emmanuel 2018 The diffusive sheet method for scalar mixing. *Journal of Fluid Mechanics* **837**, 230–257.

[72] McEwan, AD 1970 Inertial oscillations in a rotating fluid cylinder. *Journal of Fluid Mechanics* **40** (3), 603–640.

[73] Meironke, Heiko & Klembt, Daniel 2019 Measurement of flow parameters in a taylor-couette configuration using udv measurement technology. *Journal of Mechanical and Energy Engineering* **3** (3), 259–266.

[74] Meriggiola, Rachele 2012 The determination of the rotational state of celestial bodies. PhD thesis, Università degli Studi di Roma" La Sapienza".

[75] Meunier, Patrice 2020 Geoinspired soft mixers. *Journal of Fluid Mechanics* **903**, A15.

[76] Meunier, Patrice 2020b Mélanger en s' inspirant du mouvement de la terre. *Pour la Science. Dossier* .

[77] Meunier, Patrice, Eloy, Christophe, Lagrange, Romain & Nadal, Francois 2008 A rotating fluid cylinder subject to weak precession. *Journal of Fluid Mechanics* **599**, 405–440.

[78] Meunier, Patrice & Leweke, Thomas 2003 Analysis and treatment of errors due to high velocity gradients in particle image velocimetry. *Experiments in fluids* **35** (5), 408–421.

[79] Meunier, Patrice & Villermaux, Emmanuel 2003 How vortices mix. *Journal of Fluid Mechanics* **476**, 213–222.

[80] Meunier, Patrice & Villermaux, Emmanuel 2010 The diffusive strip method for scalar mixing in two dimensions. *Journal of Fluid Mechanics* **662**, 134–172.

[81] Meunier, Patrice & Villermaux, Emmanuel 2022 The diffuselet concept for scalar mixing. *Journal of Fluid Mechanics* **951**, A33.

[82] Moore, Derek William & Saffman, Philip Geoffrey 1975 The instability of a straight vortex filament in a strain field. *Proceedings of the Royal Society of London. A. Mathematical and Physical Sciences* **346** (1646), 413–425.

[83] Munro, Richard J, Foster, MR & Davies, PA 2010 Instabilities in the spin-up of a rotating, stratified fluid. *Physics of Fluids* **22** (5).

[84] Nagata, S. 1975 *Mixing: Principles and Applications*. Kodansha.

[85] Nobili, C, Meunier, Patrice, Favier, Benjamin & Le Bars, Michael 2021 Hysteresis and instabilities in a spheroid in precession near the resonance with the tilt-over mode. *Journal of Fluid Mechanics* **909**, A17.

[86] Noir, Jérôme, Brito, Daniel, Aldridge, Keith & Cardin, Philippe 2001 Experimental evidence of inertial waves in a precessing spheroidal cavity. *Geophysical Research Letters* **28** (19), 3785–3788.

[87] Ottino, Julio M 1989 *The kinematics of mixing: stretching, chaos, and transport*, , vol. 3. Cambridge university press.

[88] Phillips, Norman A 1963 Geostrophic motion. *Reviews of Geophysics* **1** (2), 123–176.

[89] Pierrehumbert, RT 1986 Universal short-wave instability of two-dimensional eddies in an inviscid fluid. *Physical Review Letters* **57** (17), 2157.

[90] Pizzi, Federico, Giesecke, André, Šimkanin, Ján & Stefani, Frank 2021 Prograde and retrograde precession of a fluid-filled cylinder. *New Journal of Physics* **23** (12), 123016.

[91] Poincaré, Henri 1885 Sur l'équilibre d'une masse fluide animée d'un mouvement de rotation. *Bulletin astronomique, Observatoire de Paris* **2** (1), 109–118.

[92] Pozzo, Monica, Davies, Chris, Gubbins, David & Alfe, Dario 2012 Thermal and electrical conductivity of iron at earth's core conditions. *Nature* **485** (7398), 355–358.

[93] Prokop, A. 1981 Bioreactor design fundamentals: Hydrodynamics, mass transfer, heat exchange, control and scaleup. *Acta Biotechnologica* **1(3)**, 269–278.

[94] Proudman, Joseph 1916 On the motion of solids in a liquid possessing vorticity. *Proceedings of the Royal Society of London. Series A, Containing Papers of a Mathematical and Physical Character* **92** (642), 408–424.

[95] Ranz, William E 1979 Applications of a stretch model to mixing, diffusion, and reaction in laminar and turbulent flows. *AIChE Journal* **25** (1), 41–47.

[96] Rayleigh, Lord 1917 On the dynamics of revolving fluids. *Proceedings of the Royal Society of London. Series A, Containing Papers of a Mathematical and Physical Character* **93** (648), 148–154.

[97] Roberts, Paul Harry 1968 On the thermal instability of a rotating-fluid sphere containing heat sources. *Philosophical Transactions of the Royal Society of London. Series A, Mathematical and Physical Sciences* **263** (1136), 93–117.

[98] Robinson, AC & Saffman, PG 1984 Three-dimensional stability of an elliptical vortex in a straining field. *Journal of Fluid Mechanics* **142**, 451–466.

[99] Rochester, MG, Jacobs, JA, Smylie, DE & Chong, KF 1975 Can precession power the geomagnetic dynamo? *Geophysical Journal International* **43** (3), 661–678.

[100] Schlichting, Hermann & Gersten, Klaus 2017 *Boundary-layer theory*. springer.

[101] Scollo, Simone, Nobili, Clément, Villermaux, Emmanuel & Meunier, Patrice 2023 Resonances and instabilities in a tilted rotating annulus. *Journal of Fluid Mechanics* **973**, A34.

[102] Shore, R. M. 2013 Improved description of earth's external magnetic fields and their source regions using satellite data. PhD thesis, University of Edinburgh.

[103] Stephenson, Makeda & Grayson, Warren 2018 Recent advances in bioreactors for cell-based therapies. *F1000Research* **7**.

[104] Taylor, Geoffrey Ingram 1917 Motion of solids in fluids when the flow is not irrotational. *Proceedings of the Royal Society of London. Series A, Containing Papers of a Mathematical and Physical Character* **93** (648), 99–113.

[105] Taylor, Geoffrey Ingram 1923 Viii. stability of a viscous liquid contained between two rotating cylinders. *Philosophical Transactions of the Royal Society of London. Series A, Containing Papers of a Mathematical or Physical Character* **223** (605-615), 289–343.

[106] Thompson, RORY 1970 Diurnal tides and shear instabilities in a rotating cylinder. *Journal of Fluid Mechanics* **40** (4), 737–751.

[107] Tilgner, Andreas 2005 Precession driven dynamos. *Physics of Fluids* **17** (3).

[108] Tsai, Chon-Yin & Widnall, Sheila E 1976 The stability of short waves on a straight vortex filament in a weak externally imposed strain field. *Journal of Fluid Mechanics* **73** (4), 721–733.

[109] Valdés, Rodolfo, Aragón, Hasel, González, Marcos, Hernández, Daily, Geada, Déborah, Goitizolo, David, Ferro, Williams, Pérez, Adelma, Garcia, Jose, Masforrol, Yordanka, Aguilar, Pedro, Márquez, Gabriel, Lao, Maylín, Gonzalez, Tatiana, Calvo, Yodelis, Hernández, Alexander, Menéndez, Grechen & Tamayo, Andrés 2017 Mouse hybridoma cell culture in a protein-free medium using a bio-mimicking fish-tail disc stirred bioreactor. *Bioprocess J* **16**, 51–64.

[110] Villermaux, Emmanuel 2012 Mixing by porous media. *Comptes rendus. Mécanique* **340** (11-12), 933–943.

[111] Villermaux, Emmanuel 2019 Mixing versus stirring. *Annual Review of Fluid Mechanics* **51** (1), 245–273.

[112] Villermaux, E. & Duplat, J. 2003 Mixing as an aggregation process. *Phys. Rev. Lett.* **91**, 184501.

[113] Von Kármán, Th 1921 Uber laminare und turbulente reibung. *Z. Angew. Math. Mech.* **1**, 233–252.

[114] Waleffe, Fabian 1989 The 3d instability of a strained vortex and its relation to turbulence. PhD thesis, Massachusetts Institute of Technology.

[115] Waleffe, Fabian 1990 On the three-dimensional instability of strained vortices. *Physics of Fluids A: Fluid Dynamics* **2** (1), 76–80.

[116] Watanabe, Daiki & Goto, Susumu 2022 Simple bladeless mixer with liquid–gas interface. *Flow* **2**, E28.

[117] Wedemeyer, EH 1966 Viscous corrections to stewartson's stability criterion(viscous corrections to stewartson theory on stability of spinning top containing liquid). *1966.* pp. 99–116.

[118] Weidman, Patrick D 1976 On the spin-up and spin-down of a rotating fluid. part 1. extending the wedemeyer model. *Journal of Fluid Mechanics* **77** (4), 685–708.

[119] Weidman, Patrick D 1976 On the spin-up and spin-down of a rotating fluid. part 2. measurements and stability. *Journal of Fluid Mechanics* **77** (4), 709–735.

[120] Widnall, Sheila E, Bliss, Donald B & Tsai, Chon-Yin 1974 The instability of short waves on a vortex ring. *Journal of Fluid Mechanics* **66** (1), 35–47.

[121] Xu, Wenchao & Harlander, Uwe 2020 Inertial mode interactions in a rotating tilted cylindrical annulus with free surface. *Physical Review Fluids* **5** (9), 094801.

[122] Zeldovich, YaB 1937 The asymptotic law of heat transfer at small velocities in the finite domain problem. *Zh. Eksp. Teoret. Fiz* **7** (12), 1466–1468.